Study of 1D Photonic crystals incorporated with thermochromic materials for energy efficient smart window applications

A thesis

Submitted in partial fulfillment of the requirements

Of the degree of

Doctor of Philosophy

By

Dipti

(ID: 20142021)

INDIAN INSTITUSTE OF SCIENCE EDUCATION AND RESEARCH

PUNE

AUGUST, 2022

Dedicated to,

My Mother

Acknowledgement

I am grateful to IISER Pune, a lovely campus. This PhD journey including one year of COVID pandemic was full of many surprises and challenges. This journey along with many scientific discussions, exciting science, the laughter and the friendship without their support, I wouldn't be writing this today!

Foremost, I would like to show my sincere gratitude towards Dr. Shouvik data for his guidance and giving me the opportunity to work in his lab at IISER Pune. I specially thank him for giving me full freedom to explore new research ideas.

I want to thank Dr. Remya Narayanan for guiding me in synthesis protocols and having enthusiastic scientific discussions and more over supporting me and always showing interest in my ideas.

I would like to thank my Research Advisory committee members Prof. G.V Pavan Kumar and Dr. Nirmallya Ballav for taking out their time and guiding my research throughout these years and providing us their valuable suggestions. I would also like to thank Dr. Aparna Deshpande with whom I have completed one-year master project. She was extremely supportive and also tried to enlighten me with her research experience. I am grateful to all the people from the Physics Department and IISER Pune for helping me in academic activities.

I would like to thank my lab mates, Mohit Kumar Singh and Anweshi dewan for their support and valuable scientific discussions.

I also thank, Technical officer nilesh dumber, Prashant kale, sudhir lone and Karthikeyan for their help during the starting of my PhD. I want to thank them for training me in magnetron sputtering, Scanning electron microscopy and Nanolithography.

I would like to thank IISER Pune for providing the most comfortable hostel accommodation. I want to mention my friends that have made during this long journey at IISER Pune. I want to thank

my friends from my batch, my senior batch and from junior batch. I want to thank Mayur, Mohit, Tejal, Sayali, Shikha, Nilam, Puneeta, Kriti, Chetan, Imran, Sandra, Abhishek, Manisha and Vikhyaat. I want to give special mention of IISER Pune badminton court. I must mention the refreshment I got after playing badminton an hour during my PhD stay at IISER. Not just playing I made very good friends with Namratha and Vishak in that court with whom I enjoyed Kerala cuisines. It's my great fortune that I met so many amazing colleagues at IISER Pune.

Dipti.

IISER PUNE

भारतीय विज्ञान विक्षा एिं अनुसंधान संस्थान, पुणे

INDIAN INSTITUTE OF SCIENCE EDUCATION AND RESEARCH (IISER), PUNE

(An Autonomous Institution, Ministry of Human Resource Development, Govt. of India)

Dr. Homi Bhabha Road, Pune – 411 008

DECLARATION

I declare that, this written submission represents my ideas in my own words and where other's ideas and works have been included, I have adequately cited and referenced the original sources. I also declare that I have adhered to all principles of academic honesty and integrity and have not misrepresented or fabricated or falsified any idea/data/fact/source in my submission. I understand that violation of the above will be cause for disciplinary action by the Institute and can also evoke penal action from the sources which have thus not been properly cited or from whom proper permission has not been taken when needed.

03/01/2023

Date

Dipti

(ID: 20142021)

IISER PUNE

भारतीय विज्ञान विक्षा एिं अनुसंधान संस्थान, पुणे

INDIAN INSTITUTE OF SCIENCE EDUCATION AND RESEARCH (IISER), PUNE

(An Autonomous Institution, Ministry of Human Resource Development, Govt. of India)

Dr. Homi Bhabha Road, Pune – 411 008

CERTIFICATE

Certified that the work incorporated in the thesis entitled "Study of 1D Photonic crystals incorporated with thermochromic materials for energy efficient smart window applications'' submitted by Dipti was carried out by the candidate, under my supervision. The work presented here or any part of it has not been included in any other thesis submitted previously for the award of any degree or diploma from any other University or Institution.

Date: 05/01/2023

Dr. Shouvik Datta

Supervisor

Table of Contents

List of Figures

Abstract

Abstract of the thesis entitle "Study of 1D Photonic crystals with thermochromic materials for energy efficient smart window applications''

Advent of artificially designed periodic structures also known as 'photonic crystals' opened up new avenues for smart window to reduce the energy consumptions in commercial buildings. An efficient smart window can regulate solar flux by adjusting the transmission of light. Photonic crystal structures due to their periodicity generates photonic band gaps (PBGs). PBGs regulates the photons of specific wavelength. Realization of photonic crystal with thermochromic material can accomplish ideal control over light transmission and reflection along heat regulation.

The main work of this thesis is focused on the fabrication and study of photonic crystals hybridized with thermochromic material for energy saving smart windows.

Here we present 1-D photonic crystals tuned in infra-red wavelength region incorporated with Vanadium Dioxide (VO_2) nanostructures. Vanadium dioxide is a phase changing thermochromic material. It is in infra - red transparent state below the phase transition temperature and in infra-red reflective state above the transition temperature. The solar modulation is an important parameter to evaluate the smart window thermochromic performance. VO_2 (M) nanostructures with tuned crystallinities are obtained. Both moderately crystalline (MC) and highly crystalline (HC) VO_2 (M) nanostructures are characterized and phase transition temperature is confirmed near to 68 ^oC. Thin films of MC and HC VO_2 nanostructures shows similar solar transmission modulation. For ease of synthesis MC – VO_2 is employed with 1-D Photonic crystals. By varying the periodic number of stacks, 1D photonic crystal (PC) can regulate the transmission and reflection in controlled manner. By combining VO_2 with ~ 100 % reflecting 1-D PC, we have achieved near to perfect absorption in near IR region above the VO_2 transition temperature. We have then tailored the transition temperature of the VO_2 (M) near to room temperature by suitably doping with tungsten atoms. One step modified hydrothermal method is used to synthesized tungsten (W) doped VO_2 (M) nanostructures. Thin films of W - VO_2 (M) incorporated on flexible 1D photonic crystals fabricated on PET substrate. Flexible 1D Photonic crystal provides the

retrofitting of exiting windows and glass. This design can regulate solar heat flux near to room temperature and incorporating W-VO_2 over high quality 1D photonic crystal, the transmission vanishes with subsequent decrease in reflection. These hybrid structures proved a potential candidate for perfect absorber in smart windows.

Finally, in chapter 3 we have studied the effect of dielectric Bragg reflector and metallic cavity on carbon dots as well. carbon dots with different emission are obtained by solvo - thermal method. The origin of light emissions is briefly described from various characterizations. Significant enhancement in photoluminescence along with reduction in FWHM (full width half maxima) is observed. This design can pave a new path for high quality color rendering devices.

Chapter 1
Introduction

1.1 Introduction and Background

The Primary goal of any contemporary energy schemes are sustainability and energy efficient operations. With the advent of technology, energy consumption is substantially increasing [1,2] all over the world. Combustion of fossil fuels produce vast amount of energy which is leading to emission of 98% of the CO_2 footprints alone [3]. Climate crises is directly related with the huge energy consumptions and these are both immediate and inevitable threat for the whole world [4]. Although governments have implemented several policies to limit the emission of CO_2 by taking measures in several sectors. One of the major sector is environment sensitive building constructions [5]. Recently, such building integrated energy saving schemes have attracted considerable attentions [6, 7]. According to the 2018's survey of energy consumptions, commercial buildings [8] are the major consumers of the overall energy consumption as shown in Figure 1.1, The significant portion of this energy consumptions comes from the air conditioners as a lot of constant energy supplies are required for heating and cooling buildings interiors as well as for artificial lightings. Moreover, significant energy loss happens through glass doors and windows [9]. According to a survey, the estimated energy required for the ventilation of these commercial buildings are approximately 30 to 40 % of the total energy consumptions [10]. This is because glass windows and glass doors are ineffective to the ingress and egress of the excesses solar light and heat.

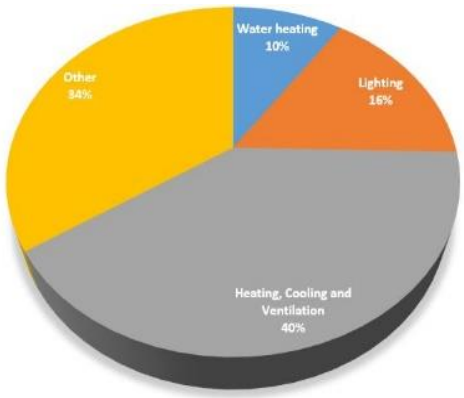

Figure 1.1 Schematic showing the percentage of energy consumers in a building [11].

Therefore, these losses of energy due to heating up through glass windows amounts to approximately 50 % of the entire energy consumed in the buildings [11]. In addition, the passage of infra-red light through glass windows are accountable for overheating the glass covered offices with greenhouse like interiors, as well as automobiles. To maintain the interior temperatures, artificial cooling and heating system with constant energy supplies are required. This increases the emission of CO_2 and contributes towards the global warming. According to the report [12], the energy requirement for artificial cooling of the interiors will be 40 times more by the year of 2100. Therefore, by controlling the optical reflection and transmission of infra-red light from solar light spectrum through windows and doors can lead to notable reduction in such energy losses. Theoretical calculations [13] shows that by controlling the in-flux of infra-red heat transfer, energy used for artificial lighting and ventilation can be reduced nearly to 50 % upon implementing improved window designs. There are various well known techniques [14] and designs that has been implemented for energy saving windows such as reflective glazing, tinted glazing and low emissive glazing etc. Manipulating the spectral response of light and controlling the infra-red heat flux according to human's need and will are being extensively explored for energy efficient windows [15]. A practical design for employing an energy efficient window for human needs has to consider various other aspects than just to reduce the usage of energy consumption. In case of office room, windows have to be fairly translucent with good optical visibility. Windows should also have fast response time to switch optical states. Moreover, it should be durable for the range of external temperatures. The robustness towards the retrofitting is also very crucial factor for any energy efficient window, fulfilling all these criteria in a design ultimately called a smart window or smart glass. Therefore, smart window can be defined as a glazed unit of glass with a material

coating over it which can dynamically changes the optical transmission and solar heat in-flux going in and going out under the influence of some external stimuli [16]. There are many technologies which are being utilized to design smart windows consisting chromic material technology [17], liquid crystal technology [18] and devices based on suspended particles [19] etc. Windows based on chromic material can be categorized as - dynamic and passive smart windows. Both have different operating mechanisms and different glazing characteristics. In general, windows based on active dynamical systems alter the optical transmissions and reflections under the influence of external stimuli such as electrical biasing, mechanical strain and even by chemical changes [20]. Whereas, passively dynamic window system, change their optical properties in the response of naturally occurring external stimuli, these windows do not require any external source of power to operate. Windows based on passive smart glazing technology can be further categorized depending on their response to external environments which include light, humidity and heat. These can be categorized as photochromic [21], humidity - chromic and thermochromics [22]. Whereas there are electrochromic [23] and gas chromic technologies [24] as well, but these are classified as actively responsive window systems. All these technologies for smart glass installation for windows and doors has its own pros and cons. Windows based on thermochromics technology respond automatically to the external heat upon tinting the glass with material responsive to heat. In this thesis, we will mainly focus on the importance of thermochromics based advanced design for smart windows hybridized with photonic crystal structure. Windows based on electrochromic technology has drawback of its high maintenance and requirement of usage of electricity which is necessary [25] for its operations. Therefore, the usage of electrochromic type smart glass is still not best choice. Windows tinted with thermochromics material surpasses many of these limitations over the time. However, thermochromics material based smart windows has its own operational constraints such as low visible light transmission and limited solar modulation [26]. Active research is going in this area to overcome these limitations. This thesis not only emphasizes on modifying the smart windows using a photonic crystal based structures but also paved a path to modify thermochromics properties of tinted materials. Tinting the glass with a coatings of thermochromics functional material can be one of the most efficient way to reduce the energy consumption in buildings. Vanadium Dioxide is a typical thermochromics material used for smart window applications as it undergoes infra-red transmitting insulating state to infra-red reflecting metallic state around its phase transition temperature. This interesting property attains exclusive

attention of researcher in past few years [27, 28]. This thesis also discusses the challenges in the synthesis and fabrication of thin films of Vanadium Dioxide and Tungsten Doped Vanadium Dioxide nanoparticles as well as the fabrication of Photonic crystal structures over flexible PET substrates. Apart from these, challenges in employing VO_2 thin films on top of a photonic crystal structures to fabricate scalable and flexible robust devices for applications in smart windows is also discussed.

1.2 Vanadium Dioxide as a Phase Changing Material

Vanadium Dioxide is a potential candidate in smart glass technology as it undergoes Metal to insulator phase change under the influence of external heat [29]. There is a wide range of materials which also respond to external heat and shows good response to transmission in visible region with change in temperatures [30-33]. However, most of these materials undergo irreversible switching action near infra-red region. On the other hand, Vanadium Dioxide (VO_2) is one of the material which respond reversibly to the applied heat, hence it exhibits a change in optical state i.e., it undergoes from semiconducting state which is transparent to infra-red light to a metallic state which is infra-red reflective around the temperature of 68°C and above [34-36]. Typical physical methods used to synthesize VO_2 are pulsed laser deposition [37], magnetron sputtering [38], electron beam deposition [39] and atomic layer deposition [40]. There are various chemicals routes to synthesize high quality VO_2 nanoparticles, such as hydrothermal method [41], electrochemical deposition [42], sol-gel method [43] and polymer assisted method [44]. As vanadium oxides occurs in many oxidation states such as +5, +4, +3 and +2 [45,46] therefore, it is quite challenging to obtain a single stable vanadium dioxide state. From Vanadium oxide phase diagram [47] it is quite evident that even at least 20 stable phases such as VO_2, V_2O_5, V_3O_7, V_4O_9 etc. can occur within a very small change in the composition. Among all these oxide phases, pristine VO_2 possess very unique optical and electrical switching properties. This makes it a very promising candidate for thermochromics based electrical switch applications [48]. The electrical conductivity of the VO_2 can change up to five orders of magnitude when the transition from semiconductor to metal phase occurs [49].

1.3 Lattice and electronic structure of Vanadium Dioxide

The Metal to Insulator transition of VO_2 was first reported by Morin in 1959 [50]. This transitional behavior leads to drastic change in its optical and electrical properties. The Pure VO_2 exhibits two phases around the temperature of 340 K. Below the temperature of 340 K it remains in monoclinic phase also known as M_1 phase with semiconducting band gap, and above 340 K it undergoes the metallic phase with lattice structure changes to rutile, also known as R phase [51 – 53]. As VO_2 comes under the class of strongly correlated system, understanding the physics of band structure of VO_2 is still an open question among researchers. With the advent of new technologies [54 – 56] and advanced computational approaches [57], researchers have putted many efforts to understand the phase transition mechanism and tried to design new VO_2 based devices with improved performances [58]. There are many theories to explain this MIT (Metal to Insulator) transition behavior. The classical band theory fails to explain the abnormal insulting behavior of VO_2 at room temperature. Thereafter, based on observations, two different mechanisms have been proposed. Peierls transition mechanism or electron correlation mechanism is the most common explanations of VO_2 transitional behavior. There are various experimental and theoretical studies for a suitable description [59] for this phase transition. It was found that electron interactions are connected with orbital occupancy and lattice structure which are the reasons for this peculiar behavior of transition in VO_2. Figure 1.2 demonstrating the lattice diagram explaining the possible explanations to understand the MIT transition. Rutile being the most stable state of VO_2 exhibits metal like characteristics with tetragonal like lattice under space group of $P4_2/mnm$ as shown in figure1.2 (a).

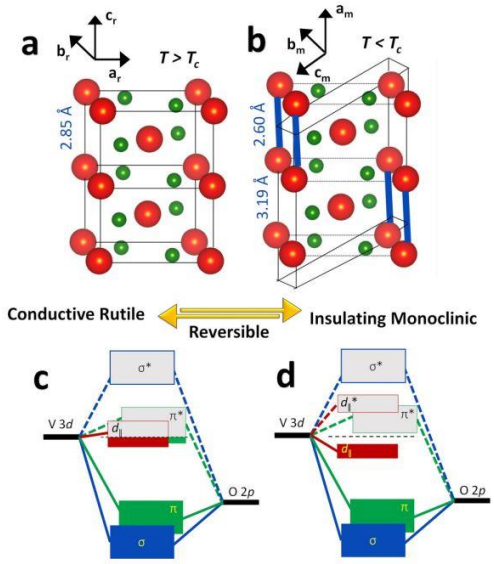

Figure 1.2 (a) and (b) Showing the lattice structure of VO_2 in rutile (conductive) and monoclinic (semiconducting) phase along with their lattice parameter, (c) and (d) showing their respective band diagram (above figure is adapted from ref [60])

This is a very symmetric structure which forms an octahedron unit where V^{4+} ions sits in corner and body center positions and each vanadium atom neighbored by O^{2-} atoms. In rutile structure all vanadium ions are chained up linearly, with adjacent V-V bond has spacing of ~ 2.85 A° along the c-axis. All the vanadium atoms in the linear chain formed by V-V bond has equal share of d-orbital electrons. Subsequently, it leads to the metallic phase which results in higher conductivity of electron with resistivity as low of the order of 10^{-6} Ωm [61]. Figure 1.2 (b) showing the semiconducting phase reaches with temperature less than 340 K. The lattice structure belongs to the space group of $P2_1/c$, here two vanadium atoms undergoes the dimerization along the monoclinic a-axis. This creates a chain of zigzag vanadium atoms with two alternate different distance i.e. shorter and longer length of V-V bonds with spacing of 3.19 A° and 2.60 A° respectively. Two different distances of vanadium atoms or dimerization that doubles up the unit cell along the axis and this leads to the distortion which lowered the structural symmetry and hence electrons present in d-orbitals localize. This gives the monoclinic VO_2 structure its insulting state having the resistance near to the order of 0.1Ωm [62]. Goodenough [63] had also proposed band and molecular structure of VO_2. As the electronic structure of V and O atom goes as $[Ar]4s^2 3d^5$ and $1s^2 2s^2 2p^4$ respectively. Vanadium occupy V^{4+} state and fill the 2p Oxygen shells and others

electrons go into the 3d lower shells. According to crystal field theory 3d shell go into octahedral splitting of e_g which is twofold high energy level and t_{2g} which a threefold low energy level. Due to strong crystal field e_g form d_σ and t_{2g} further splits into $3d_\pi$ and $3d_{//}$. With increase in temperature, rutile phase hybridized with vanadium $3d_\pi$ and oxygen $2p_\pi$ strongly than nonbonding orbital of Vanadium $3d_{//}$ and oxygen $2p_\pi$. In rutile phase, the band energy is around 2.5 eV and there is overlap between $3d_\pi$ and $3d_{//}$ with the fermi level near to this overlap therefore makes the phase conductive in nature as clearly shown in Figure 1.2 (c). With temperature below 340 K when the lattice is in monoclinic phase (M_1). This is shown in Figure 1.2 (d) due to the dimerization along the rutile c-axis leads to distortion which causes the 3d// band to split into additional bonding and antibonding states. The overlapping between $3d_\pi$ and $2p_\pi$ increases which causes antibonding $3d_\pi$ to lift upward above the fermi level. The splitting of $3d_{//}$ band into $d_{//}$ bonding and $d_{//}$ antibonding reduces the $3d_\pi$ antibonding and $3d_{//}$ bonding band gap to 0.7eV, which finally gives monoclinic it's insulting character. VO_2 Metal to Insulator (MIT) transition band energy mechanism can be explained with many experimental results and theoretical calculations which many other factor can contradict the above explanation [64]. This MIT transition in general depends on many factors which makes understanding this mechanism in general more complex. Overall the correlation between electrons in VO_2, distortion in lattice and Peierls instability are the factors which makes this mechanism more complex. These arguments give interpretation of MIT transition of VO_2 which is a decade long debate such as splitting of $3d_{//}$ band is influenced by dimerization of V-V bond which double the unit cell which leads to lattice deformation similar to Perierl mechanism [65] to explain this MIT transition which explain the correlation between electron-lattice with electron of $3d_{//}$ band [66] or upon combining both theories [67]. Therefore, the phase transition of VO_2 and its mechanism depends upon various external factors as well such as VO_2 morphology and stoichiometry etc. which makes the actual transition quite complex to articulate within a simple situation.

This MIT Phase and temperature can be perturbed by external doping. We can increase and decrease this transition temperature with the substitution of suitable dopant. On substituting dopant with the valance state higher than +4 the transition temperature of VO_2 will decrease [68] substantially. Tungsten being most suitable dopant to substitute for Vanadium atom in VO_2 to lower the transition temperature near to room temperature. The best reported value of transition temperature reduction is up to 27K/at. % of doping [69]. This potential of modulation of desired

temperature which leads to the considerable change in optical and electrical properties in IR region makes VO_2 a promising candidate for smart window applications. In chapter 4 we will discuss the effect of Tungsten doping on Vanadium Dioxide which incorporated with flexible 1D Photonic crystal which proved to be an efficient method for energy saving smart windows.

1.4 Tungsten Doped Vanadium Dioxide

Doping tungsten into vanadium dioxide intentionally can alter its electrical and optical properties by modifying the metal - Insulator transition temperature. So far at least 60 elements either experimentally or theoretically have been explored as intentional dopants for vanadium dioxide. Doping element is chosen based on following criteria. Firstly, that dopant is chosen which can increase the concentration of carriers and can also alter the electrical phase transition. Secondly, that dopant should induce distortions in atomic lattice structure of VO_2, which can lead to the change in structural phase itself. When a doping element is introduced into VO_2, it acts either as a donor or as an acceptor. Accordingly, it drives either electron or holes into the VO_2 lattice [70]. There are various experimental techniques which were utilized to study the phase diagram of tungsten doped vanadium Dioxide such as Tang *et.al* [71] based on X-ray scattering and absorption method elaborates on reduction of transition temperature. This is because injected tungsten atoms in vanadium dioxide leaves their electrons in vanadium valance band 3*d*, which breaks the V^{4+} - V^{4+} bonds in monoclinic M_1 phase. This leads to distortion of Monoclinic phase M_1 and hence reduced the MIT transition temperature. There are various spectroscopy results such femtosecond spectroscopy [72], ultraviolet-infrared spectroscopy [73] and theoretical calculations has been done to explain the effect of tungsten doping on this metal to insulator transition. Booth *et al*. observed that tungsten atoms breaks the Peierls V-V bond due to enlargement of crystal axes which leads to reduction in transition temperature of VO_2 [74]. To have a clearer picture, we need to understand the MIT transition for a large range of dopants concentrations. Therefore, there are two main aspects on which we should focus on while using tungsten as a dopant in vanadium dioxide. Firstly, why introducing a very small amount of tungsten atoms in vanadium dioxide would lead to such drastic change in VO_2 lattice structure and secondly, what is the physical mechanism involved while MIT transition once tungsten is introduced. To understand role of tungsten in the

local structure around VO_2 lattice, X-ray absorption fine structure spectroscopy is studied [75]. This shows that with the dilute concentrations of tungsten, there is some enhancement in symmetry in lattice structure in the Rutile phase. It also leads to expansion of lattice volume. Density functional theory calculations reveals that even at low concentrations, tungsten dopant can drive a large change in VO_2 lattice and subsequently to its atomic and electronic structures. Insertion of tungsten atoms within large volume in VO_2 lattice, however, leads to the local lattice distortion. Higher valance state tungsten ions aggregate the electrons on the vanadium sites which suppress the doubling lattice and distort the insulting VO_2 monoclinic Phase. Which is the main reason of temperature reduction of MIT transition even with a dilute concentration of tungsten atoms.

1.5 Photonic crystal based smart windows

As already discussed in the above section, there are concerns regarding the effect of energy consumption where a substantial usage of energy goes towards maintaining the building environment. Therefore, energy consumed in heating and cooling of buildings from the infrared heating, which is 50% from the overall sun energy, causes significantly towards global warming [76]. For a comfortable room environment, controlling heat as well adjusting room brightness is equally important [77]. For energy saving consumptions in buildings, heat shielding from the infra-red light and attaining good transparency are few of the challenges. There are various approaches to reduce the heat, one of the approach is to use a metal layers over the glass windows or doors, infra-red absorption is significant with metal based material layer coating. due to metallic coating over glass, it loses its visibility which makes these design less suitable for practical purpose. [78]. Therefore, blocking infra-red radiation and controlling the transmission or reflection wavelength would be promising approach for smart windows applications for energy consumption reduction. To serve the above purpose, we use photonic crystals as a new class of material substrate which can be utilized to control the optical spectra of solar energy being allowed to transmit and reflect. This has opened new directions for smart glasses. Photonic crystal materials are found in nature and can also be artificially fabricated in labs. Therefore, it is an active topic of extensive research be it for fundamental studies or for applied applications.

1. 6 Introduction to Photonic crystals

Photonic crystal was first analyzed in 1976 by Amnon Yariv, Pochi Yeh and C.S. Hong [79-80]. These are also known as photonic band gap crystals formed by periodicity in dielectric material which can manipulate the light by creating a photonic band structure similar to electronic band structure in crystalline solids. In semiconductors, due to the periodic arrangement of atoms in lattice results in formation of periodic potential which creates an electronic band gap, the region where motion of electrons is prohibited. In a similar way, in photonic crystal a photonic band gap is created which block the light of certain wavelength inside the photonic crystal i.e. photons having certain energies are forbidden within these structures. In other words, if a light of certain polarization has the similar frequency as that of the photonic crystal, it will reflect it with 100% efficiency. Similar to the electronic system, the periodicity of the photonic crystal can be broken by introducing a defect. Introduction of defect results in formation of new eigen states with eigen energy corresponds to the band gap of the defect. Photon with wavelength similar to defect frequency were allowed to propagate inside the structure. This sort of structures was beneficial to study fundamental physics of optical micro-cavites. Based on the fabrication and geometry of Photonic crystals (PCs), they are classified into one- dimensional (1D), two- dimensional (2D) and three-dimensional (3D) with periodic modulation of refractive index in 1, 2 or 3 dimension as shown in Figure 1.3.

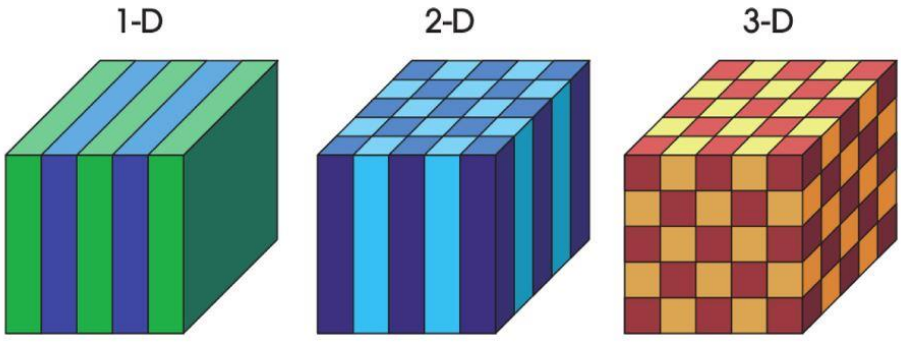

Figure 1.3 Schematic of Photonic crystals in one, two and three dimensions (Figure is adapted from ref [82])

In this thesis we have mainly worked with 1D Photonic crystals. However, 2D Photonic crystals were usually fabricated using optical and/or e-beam lithography.

1.6.1 One Dimensional Photonic crystal (1D –PhC)

1-D Photonic crystal are the structures with periodic modulation in one direction [79]. Artificial periodicity of 1D PC can be fabricated by creating the periodic modulation of refractive indices in one direction. In general, one chooses the direction along the light propagation. The other two directions remain homogenous for light propagation [81]. In nature, there are several examples of naturally occurring 1-D photonic crystal for e.g. Neon tetra a tropical fish, the scales of fish consist of many periodic 1-D reflecting platelets which changes the color of fish from blue to deep violet. Optical properties of 1D Photonic crystal structures can be simulated using transfer matrix method. To fabricate the 1D Photonic crystal, researchers have employed various techniques such as Bottom-up approach and top-bottom approach. The bottom-up techniques generally compromise the self-assemblies of structures in a periodic way. Copolymer based photonic crystal is an example of 1D Photonic type crystal where system reaches the ordered structure on its own when it attains lowest energy state. 3-D synthetic opal system is also an example of self-assembled 1D Photonic crystal system. Fabrication of multilayer structures periodically by alternate deposition of thin films are also included in bottom-up approach. This sort of fabrication includes the alternate spin coating of polymers, dip-coating etc. But in case of polymer based photonic crystal, contrast between refractive indices are small therefore, a large no of alternate periodic layers having different refractive indices are required. Top-down technique is also used to fabricate Photonic crystals. This is mainly used in optical components and display applications. Top-down approaches includes holographic photo-polymerization [82] which is a soft lithography based technique used to fabricate polymer based 1-D photonic nanostructures. This approach offers a quick and simple route to fabricate photonic crystal structures. Another top-down technique used to fabricate photonic crystal structure is layer-multiplying coextrusion [83]. This method is used to fabricate 1-D photonic crystal by depositing hundreds of layers of two polymers alternately. For commercial purposes, mostly vacuum based physical vapor systems are used. Sputtering is also another common fabrication technique to fabricate large area uniform 1D Photonic crystals [84]. In Figure 1.4 (a), 1D photonic crystal slab formed by depositing high and

low refractive index layers alternatively in ordered manner. The characteristics of the dielectric slab are depending on the contrast of refractive indices, thickness of layers and number of layers to fabricate the whole dielectric structure. As shown in Figure 1.4 (b), light incident normally on the surface and get reflected and the amount of light reflected from the two interfaces of the dielectric is measured by the Fresnel formula, which is given as,

$$R = \left(\frac{n_2 - n_1}{n_2 + n_1}\right)^2$$

where n_1 and n_2 are the high and low refractive indicies of the alternate layers. It is quite evident from the above equation higher refractive index leads to high value of reflectivity from the interfaces and a few number of layers are required to achieve higher reflectivity. In genral, the optical thickness of each layer is set to be ($\lambda/4n$) which is quarter of reflecting wavelength, this way we can achieve the maximum reflectivity by nomrally incidenting the light on the multilayer stack. This type of 1D Photonic crystal known as quarter wave stack. In this thesis, all these 1D Photonic crystal fabrictaed are quarter wave stacks with thichkenss of each layer to be one fouth the reflecting wavelength. This is a well known constrctution method and is used in many devices including Fabry-Perot filters and distributed feedback laser. From figure 1.4 (b) explain physical picture of the working of highly reflective dielectric stack. To form a photonic band, the light which is reflected from each dielectric surface is the multiple of 2π to interfere constructively and the light which reflected while going from low to high refractive index interface experince the phase shift of π. Light experience no phase shift while going from high to low refractive index interface. From the skecth it is clear that light experince phase shift of π while going from air to interface n_2.

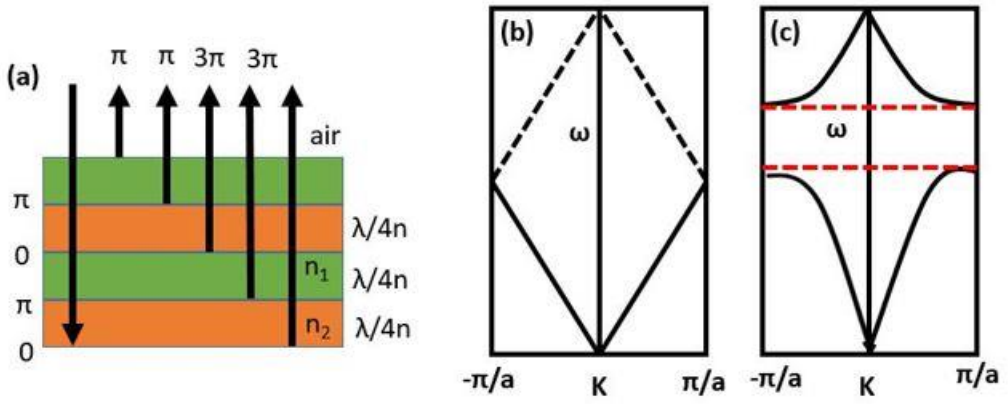

Figure 1.4 (a) Showing the schematic of working mechanism of 1D Photonic crystal, (b) showing the band diagram in 1D uniform media and (c) showing the band diagram in media with alternate periodicity [85].

Second reflection also go through phase shift of π due to the round trip of light from the first interface, the other subsequent reflection from the dielectric stack are also 2π out of phase to interfere constructively, therefore it makes the quarter wave stacks highly reflecting in nature. Figure 1.4 (b) and (c) are illustrating the physical origin of Photonic band gap. As explained already photonic crystal are the optical analogy of the electronic band gaps in solid structures. Depending on the lattice periodicity, the photonic band gap can be formed in all direction, this can result in 3D Photonic crystals. Photonic crystal research field is like marriage between electromagnetism and solid state physics, to understand the concepts of photonic band gap one should have a good grasp in fundamentals of both fields, Photonic band gaps in 1D Photonic crystal can be formed by solving the Maxwell equation. This formulation can be found in reference [85] which assumes the periodicity in dielectric constant. Based on Bloch theorem, the solution of the Maxwell equation gives the Eigen values in terms of ω and k. This also gives the photonic band gaps for complex values of k where there are no propagating solutions. Figure 1.4 (b) is showing the solution of 1D system with constant dielectric constant ε, on perturbing ε with some periodicity the solution of Maxwell equation is given as Figure 1.4 (c). This leads to the formation of the optical band gap. larger is the dielectric contrast of alternating layer, boarder is the stop band of the photonic crystal. 1D photonic crystal also exhibit important properties such as surface states which induce localized modes. These form the basis of photonic crystal based waveguides and photonic crystal based cavities as well.

1.6.2 Two Dimensional Photonic crystal (2D-PhC)

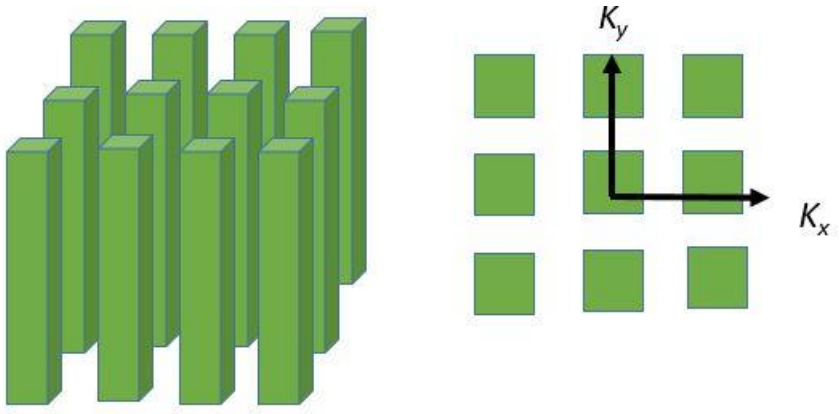

Figure 1.5 Schematic diagram of 2D Photonic crystal with periodic symmetry along x and y axis.

2D PhC are formed when periodic modulation of refractive indices is along two spatial directions and leaving the third direction homogenous. Therefore, periodic modulation in 2D PhC occur in a plane. Typical examples of 2D photonic crystals are holes drilled periodically in a slab. Periodically etched rods in square lattice are shown in Figure 1.5. This type of photonic crystal creates photonic band in a plane, inside the band gap frequency no other energy state with those frequency is allowed. The major difference from the multilayer stack is that it prohibits or reflect the light which incident normally to the surface, whereas two-dimensional photonic crystal can block or reflect the incident light from any direction of the periodic plane. 2D photonic crystal creates band in a plane. The band structure is calculated for modes into two polarization say TE and TM mode. To form the photonic bands, symmetry in crystal lattice is required. As the system is homogenous in say z direction, the restriction on k, the wave vector will be lifted. The system will possess periodicity in x-y plane the permittivity ε will have translation symmetry with component in both x and y direction. Upon applying the Bloch theorem, the allowed values of k for both TE and TM modes for 2D Photonic crystal can be calculated. Finite Difference Time Domain (FDTD) is frequently used method to calculate the dispersion relation for TE and TM polarized light. 2D photonic crystal based cavities can also formed by inducing some defect in the periodicity. 2D Photonic crystal cavity due to high quality factor have various application in photonic crystal based laser and in waveguides

1.6.3 Three Dimensional Photonic crystal (3D PhC)

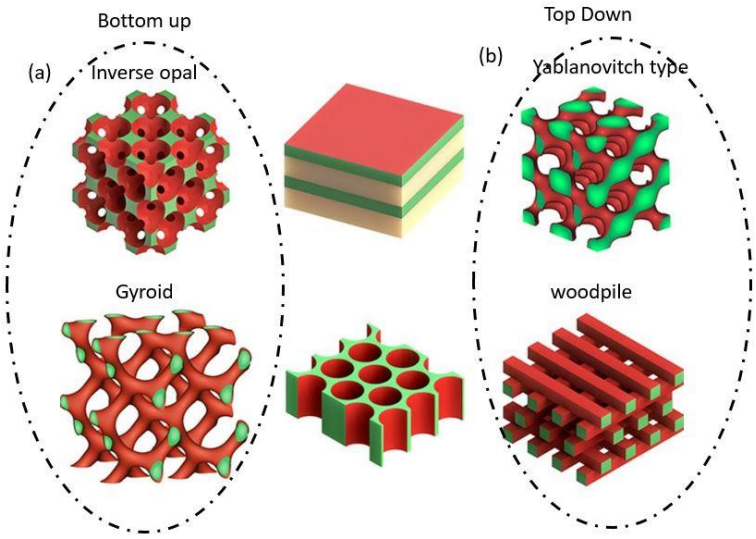

Figure 1.6 (a) showing the inverse opal 3D Photonic crystal Fabricated with bottom up approach and (b) Showing the 3D woodpile Photonic crystal structure fabricated with top down approach (Figure is adapted from Ref [85])

3D photonic crystal is also known as ultimate photonic crystal. They have periodicity of refractive indices in all three x, y and z directions. Various examples of 3D Photonic crystal occurring in nature are opal and inverted opal structures. To form a 3D Photonic crystal self-assembly of mono dispersed particles leads to the formation of opal and inverted opal structure. Opal structures can be fabricated by forming spheres over the substrates. Inverted opal structure can be fabricated from the opal structures. If the void between the sphere is filled with another material and if the spheres are removed later, then the remaining structure will form the inverted opal structure with symmetrical periodicity in all three directions. This structure is similar to honey comb like structure as shown in figure 1.6(a), photonic crystal has photonic band gap in all three directions i.e. this structure has complete band gap. Although as compared to 1D and 2D photonic crystal, achieving periodicity of refractive index in all three directions is a really challenging task [86]. Techniques such as photo lithography, e-beam lithography and ion etching are utilized to fabricate 3D Photonic crystals. Woodpile structure is a famous example of 3D Photonic crystal.

Photonic crystal structure fabricated as 1-D ,2-D or 3-D can regulate the photons in desired manner by creating photonic bands and localized surface states by arranging spatial configuration of refractive indices in a periodic manner. As Photons can be manipulated as heat carriers. therefore, there are many reports in which Photonic crystals are used a main component to manipulate the heat radiation . It is observed photonic bands effect the thermal photons and its transport properties [87]. There are theoretical calculations which shows that multilayer structures can decrease the thermal conductance by using photonic bands, this property makes photonic crystals a key component coating for thermal barrier applications [88]. Combining Photonic crystal with thermochromic materials provides the advantage of operational tunability. Incorporating thermochromic material with photonic crystal can gives the static control of light by optimizing the stop band of the photonic crystal and due to thermochromics material further provide the dynamic control in near infra-red region as it changes state automatically in response to external heat. All these properties make Photonic crystals a good candidate for smart windows or smart glass designs. Research in the field of smart windows mainly comprises the idea based on materials which exhibits certain properties such as organic materials or thermochromics material. There are very few reports about the role of Photonic crystal in smart glasses or smart windows where photonic crystal being the crucial aspect. In this thesis we have clubbed the idea of thermochromics material with Photonic crystals which make this a very efficient and novel design for smart glass. Although Photonic crystal of different structures can be employed with materials, be it thermochromics or electrochromic to utilize them for smart glass purpose. In the subsequent sections we will briefly describe the Photonic crystal based smart windows.

1.7 Photonic crystal with electrochromicity

Electrochromic materials are well known for their utility in smart windows. Electrochromic materials work on applying the electric current or voltages and show significant change in their optical properties. The main characteristics of an electrochromic based devices is change in optical transmission which mainly occur due to change in state of valance ions. Electrochromic based devices and smart windows has four main contributing factors such as, change in optical transmission state before and after applying the electric current and voltage. The state before applying the electrical input is generally known as colored state. After the application of electric

current or voltage, the state is usually known as bleached state. Other main contributing factor is response time; this time refers to the duration in which electrochromic material goes from one state (colored state) to other state (bleached state). A general rule of thumb to define the response time is the duration in which the transmission of material upon application of electric current or voltage reaches to 90%. Coloring efficiency and coloring cycle stability are the other main characteristics of an electrochromic material. To implement these electrochromic devices as smart glass applications for commercial purposes, the change in optical transmission should be constant on application of voltage for a regular number of cycles and duration of time. Although there are materials which shows all the above characteristic to a good extent, but still electrochromic materials are not good enough for commercial applications. This is because, optimization of all four characteristic mentioned above in a single material is still a challenging task. Electrochromic materials are further divided into organic and inorganic electrochromic materials. Tungsten Trioxide is one the most common inorganic electrochromic material which has reported enhanced color efficiency when embed within inverse opal type 3D Photonic crystal [89].

1.8 Photonic crystal with thermochromicity

Thermochromism is the phenomenon in which a material can undergo a phase transition which leads to reversible change in its optical coloration under the influence of applied heat [90]. One of the main advantage of thermochromics material over electrochromic material is that they are self-regulatory, and doesn't require external electrical stimulus or some extra source of energy. Thermochromics material like Vanadium Dioxide is one of the smartest material which can regulate the infra-red light from the solar spectrum according to the change in its surrounding temperature. This unique property makes vanadium dioxide an ideal candidate as functional smart material for smart glass technology.

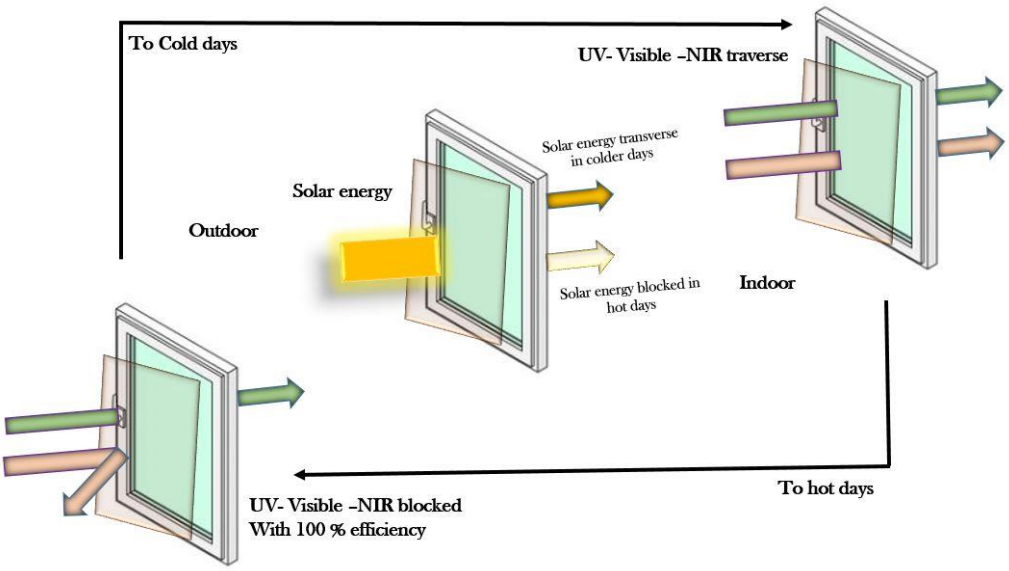

Figure 1.7 Showing the working of smart window incorporated with Photonic crystal layers in hot and cold days.

The main parameters governing the smart window performances are regulation of luminous transmission and ability to modulate the solar radiation. For smart windows applications, the requirement of luminous transmission should be more than 60 %. Although in past, there are several design factors to control the building heat via convection and conduction technologies. Usage of layered glasses with inert gas filled in-between the glass plates were also tried, which deceases the impact of heat inside of building. But all these innovations cannot regulate the luminous transmission and the solar radiation automatically. With change in external heat or other stimulus, it also decreases the luminous transmission substantially. Therefore, this opens opportunities for new inventions in the field of energy saving coatings for smart window glasses. While using vanadium dioxide as thermochromic smart material for the above purpose, solar modulation throughout the day will be another important parameter of concern. To serve the purpose of solar modulation to control the heat efficiently should be more than 10% to be considered as effective for energy efficient windows. Therefore, having good luminous transmission and dynamic regulation of solar light to perfection is still a challenge for smart window research. Reports suggested that luminous transmission enhancement with anti-reflecting coating leads to reduction of solar modulation with deposition of antireflective coatings [91]. Solar modulation can be enhanced with increased thickness of vanadium dioxide but it can cause

absorption in visible region as well as leads to the reduction of luminous transmission. Now combining thermochromic with photonic crystals can fulfill both of the above stated criteria and can give a very feasible and large scale, reproducible designs for smart glasses for the application in smart windows, doors etc. The above sections have already discussed about the photonic crystal. These are artificially made periodic structures. A photonic crystal would reflect a color when it's band gap lie in visible region by following the simple Bragg law. There are various reports of Vanadium Dioxide over Photonic crystals for implementation in smart window glass like applications. For example, inverse opal photonic crystal which can tune its photonic band gap by just changing the size of these colloidal opals. They can be easily synthesized by sol-gel method. This can easily enhance the solar modulation in regular manner but due to intrinsically high refractive index of VO_2 transmission luminescence enhancement would be a challenge. But inverse opals made out of the SiO_2 composite with vanadium dioxide [92] has reported increased luminous transmission with improved solar modulation. Even homogenous periodicity of inverse opal VO_2 system not only increased the thermochromic performance, but also it reduced the phase transition temperature [93]. Therefore, these interesting designs of photonic crystals incorporated with thermochromics materials for new application of smart glass technology for energy saving applications.

1.9 Aim and Scope of the thesis

Therefore, the primary goal of this thesis is to implement Photonic crystal structures with thermochromic materials for improving the designs for energy efficient smart windows in building fenestrations. We have addressed the issues of robustness and durability for smart glass designs with improved transmission and reflection efficiency. With this aim, we have divided the thesis into two studies. In the first part [chapter 3] we have incorporated vanadium dioxide a 'thermochromics material' with 1-D photonic crystal fabricated with alternate deposition of SiO_2/TiO_2 over glass with tunability in near Inra-red wavelength region. In the other Part [chapter 4] we have tuned the transition temperature of Vanadium Dioxide with suitable doping near to room temperature and incorporated it over flexible 1-D Photonic crystals structures, as a consequence, the transmission and reflection via these structures regulates with nearly 100 % efficiency with retrofitting applications.

The next Chapter 2, briefly discusses the fabrication and characterization of 1D Crystals and thermochromic materials in details. We have briefly explained the various instruments, working principle and techniques such as UV- Visible absorption spectroscopy, X-ray diffraction spectroscopy, scanning tunneling microscopy and transmission electron microscopy. Apart from these we have described the homemade set up for high temperature reflection spectroscopy and micro-photoluminescence spectroscopy which are assembled to characterize VO_2/1-D Photonic crystal structure, W - doped VO_2/1D-Photonic crystal structures.

In chapter 3, we have synthesized VO_2 nanostructures by thermolysis method. VO_2 nanostructures of tuned crystallinities are synthesized. FESEM imaging, TEM imaging and high temperature XRD measurements, are performed on VO_2 nanostructures of different crystallinities and confirming the phase transition from monoclinic to rutile phase at and above 68 ºC. Thin films of VO_2 nanostructures with PVP are fabricated and employed over 1D photonic crystals also known as Bragg reflector of varying stacks. The effect of number of stacks of Bragg reflectors over transmission and reflection of VO_2/1-D Photonic crystal structure is studied. Bragg reflector of ~ 100 % reflectivity are fabricated and employed with phase changing VO_2 materials and near to perfect absorption enhancement in VO_2/1-D Photonic crystal structures are studied.

In chapter 4, We have further tailored the transition temperature of VO_2 nanostructures by doping with tungsten atoms which reduces the transition temperature near to room temperature. Tungsten doped VO_2 nanostructure are employed on flexible 1D photonic crystals fabricated over PET substrate. DBR's are fabricated over PET substrate as it offers flexibility. Good crystallinity W - VO_2 (M) nanostructures are obtained with one – step hydrothermal method. we have reported the least time reaction to obtain the W - VO_2 (M) nanostructure for the first time. Various characterizations have confirmed the phase transition of W-doped VO_2 nanostructures thin films. Thin films of W- doped VO_2 nanostructures shows good optical modulation. Incorporating with flexible 1D Photonic crystal not only shows the good optical transmission and reflection control but also shows good performance under compressive bending, which make this design quite robust and economical for smart glass applications as an optical absorber.

In chapter 5, we will report the synthesis of environmental friendly with good optical tunablity, blue, green and red emission carbon dots. The optimized mixture of carbon dots can achieve white light emission. Incorporation of these dots which can be excited with single excitation source with

dielectric Bragg reflectors and broad band reflective metal cavity structures gives significant enhancements in Fluorescence. Studying these structures will have great potential in color rendering devices and highly efficient carbon dot based LEDs.

Finally, with Chapter 6, we will end this thesis work with brief discussion on future outlook.

1.10 Reference

[1] Gorgolis G, Karamanis D, Solar energy materials for glazing technologies. *Sol Energy Mater Sol C*, **2016,** 144, 559–578.

[2] Hee W J, Alghoul M A , Bakhtyar B , Elayeb O, Shameri M A, Alrubaih M S, Sopian K, The role of window glazing on daylighting and energy saving in buildings. *Renewable Sustainable Energy Rev*, **2015**, 42, 323–343.

[3]https://www.biologicaldiversity.org/programs/climate_law_institute/energy_and_global_warming/index.html

[4] https://www.eea.europa.eu/signals/signals-2017/articles/energy-and-climate-change

[5] https://www.government.nl/topics/climate-change/national-measures

[6] Khandelwal H , Loonen R C, Hensen J L , Debije M G, Schenning A , Electrically switchable polymer stabilised broadband infrared reflectors and their potential as smart windows for energy saving in buildings, **2015**, *Sci Rep*, 5, 11773.

[7] Kamalisarvestani M, Saidur R , Mekhilef S, Javadi F S, Performance, materials and coating technologies of thermochromic thin films on smart windows. *Renewable Sustainable Energy Rev* **2013**, 26, 353–364.

[8] Hong Y, Xianchun M, Bin X, Theoretical discussions of perfect window, ideal near infrared solar spectrum regulating window and current thermochromic window, *Energy and Buildings*, **2013**, 49 164–172.

[9] file:///D:/Thesis%20Chapters/Chapter%201/qtr-2015-chapter5.pdf

[10] Feng M, Bu X, Yang J, Li D, Zhang Z, Dai Y and Zhang X, Review: smart windows based on photonic crystals, *J Mater Sci*, **2020**, 55, 8444–8463.

[11] Khandelwal H , Schenning A.P. H. J., and Debije M.G. , Infrared Regulating Smart Window Based on Organic Materials, *Adv. Energy Mater*, ***2007***, 7, 1602209.

[12] Isaac M, Vuuren D. P. V , Modeling global residential sector energy demand for heating and air conditioning in the context of climate change, *Energy Policy*, **2009**, 37, 507.

[13] DeForest N, Shehabi A, O'Donnell J, Garcia G, Greenblatt J, Lee E. S, Selkowitz S, Milliron D. J , *Build. Environ*, **2015**, 89, 107

[14] Chow T.T., Li C.Y., Lin Z., Innovative solar windows for cooling-demand climate, *Solar Energy Materials and Solar Cells* , **2010**, 94, 212–220.

[15] Granqvist C.G., Transparent conductors as solar energy materials: A panoramic review, *Solar Energy Materials and Solar Cells,* **2007,** 91, 1529–1598.

[16] Wang X and Narayan S, Thermochromic Materials for Smart Windows: A State-of-Art Review. *Front. Energy Res*., **2021**, 9, 800382.

[17] Granqvist C G, Green S, Niklasson G A , Mlyuka N R , von Kraemer S , Georen P , Advances in chromogenic materials and devices, *Thin Solid Films,* **2010**, 518, 3046–3053.

[18] Cupelli D, Nicoletta F P, Manfredi S, Vivacqua M, Formoso P, De Filpo G, Chidichimo G, Self-adjusting smart windows based on polymer-dispersed liquid crystals, *Solar Energy Materials and Solar Cells* **2009**, 93, 2008–2012.

[19] Vergaz R, Sanchez-Pena J M, Barrios D, Vazquez C, Contreras-Lallana P, Modelling and electro-optical testing of suspended particle devices, *Solar Energy Materials and Solar Cells* , **2008**, 92, 1483–1487.

[20] Baetens R, Jelle B P, and Gustavsen A, Properties, Requirements and Possibilities of Smart Windows for Dynamic Daylight and Solar Energy Control in Buildings: A State-Of-The-Art Review. *Solar Energ. Mater. Solar Cells* **2010**, 94, 87–105.

[21] Pardo R, Zayat M, Levy D, Photochromic organic–inorganic hybrid materials, *Chemical Society Reviews* , **2011**, 40, 672–687

[22] Saeli M , Piccirillo C, Parkin I P , Binions R , Ridley I, Energy modelling studies of thermochromic glazing, *Energy and Buildings,* **2010** , 42, 1666–1673.

[23] Piccolo A, Thermal performance of an electrochromic smart window tested in an environmental test cell, *Energy and Building* **2010**, 42, 1409–1417.

[24] Wittwer V, Datz M, Ell I, Georg A, Graf W, Walze G, Gasochromic windows, *Solar Energy Materials and Solar Cells* **2004**, 84, 305–314.

[25] https://www.thehomehacksdiy.com/the-pros-and-cons-of-smart-glass/

[26] Granqvist C G, Ji Y X, Montero J and Niklasson G A, Thermochromic vanadium-dioxide-based thin films and nanoparticles: survey of some buildings-related advances, *J. Phys.: Conf. Ser.* **2016**, 764, 012002.

[27] Li S, VO2-based thermochromic and nanothermochromic materials for energy-efficient windows: computational and experimental studies. *Acta Universitatis Upsaliensis***; 2013**.

[28] Gonçalves A., Resende J. , Marques A.C. , Pinto J.V., Nunes D., Marie A., Goncalves R., Pereira L., Martins R. , Fortunato E., Smart optically active VO2 nanostructured layers applied in roof-type ceramic tiles for energy efficiency, *Sol Energy Mater Sol Cells*, **2016**, 150, 1-9.

[29]https://ceramics.org/ceramic-tech-today/basic-science/researchers-improve-understanding-of-insulator-metal-transition-in-vanadium-dioxide-films

[30] Sane K and Fukuda Y, Inorganic thermochromism, *Berlin: Springer-Verlag*, **1987.**

[31] Day J H, Thermochromism of inorganic compounds. *Chemical Reviews*, **1968**, 68 p. 649-657.

[32] Tsuyumoto I and Uchikawa H, Nonstoichiometric orthorhombic titanium oxide, TiO2-δ and its thermochromic properties. *Materials Research Bulletin*, **2004,** 39,1737-1744.

[33] Bloomquist D and Willett R, Thermochromic phase transitions in transition metal salts. *Coordination Chemistry Reviews*, **1982,** 47, 125-164.

[34] Morin F, Oxides which show a metal-to-insulator transition at the Neel temperature. *Physical Review Letters*, **1959**, 3. 34

[35] Eyert V, The metal-insulator transitions of VO2: A band theoretical approach. *Annalen der Physik,* **2002,**11, 650-704

[36] Narayan J and Bhosle V, Phase transition and critical issues in structure property correlations of vanadium oxide. *Journal of Applied Physics*, **2006,** 100, 103524-103524-6.

[37] Borek M, Qian F, Nagabushnam V and Singh R, Pulsed laser deposition of oriented VO2 thin films on R-cut sapphire substrates. *Applied Physics Letters*, **1993**, 63, 3288-3290.

[38] Mlyuka N, Niklasson G and Granqvist C G, Mg doping of thermochromic VO2 films enhances the optical transmittance and decreases the metal-insulator transition temperature. *Applied Physics Letters*, **2009,** 95, 171909-171909-3.

[39] Babulanam S, Eriksson T, Niklasson G and Granqvist C, Thermochromic VO2 films for energy-efficient windows. *Solar Energy Materials*, **1987**, 16, 347-363.

[40] Rampelberg G, Schaekers M, Martens K, Xie Q, Deduytsche D, Schutter D De , Blasco N , Kittl V and Detavernier C, Semiconductor-metal transition in thin VO2 films grown by ozone based atomic layer deposition. *Applied Physics Letters*, **2011**, 98, 162902-162902-3.

[41] Li M, Magdassi S, Gao Y and Long Y, Hydrothermal synthesis of VO2 polymorphs: advantages, challenges and prospects for the application of energy efficient smart windows. *Small*, **2017**, 13, 1701147

[42] Koza J A, He Z, Miller A S and Switzer J A, Resistance switching in electrodeposited VO2 thin films. *Chemistry of Materials*, **2011**, 23, 4105-41

[43] Seyfouri M M, and Binions, Sol-gel approaches to thermochromic vanadium dioxide coating for smart glazing application. R., *Solar Energy Materials and Solar Cells*, **2017,** 159, 52-65

[44] Louloudakis D, Vernardou D, Spanakis E, Dokianakis S, Panagopoulou M, Raptis G, Aperathitis E, Kiriakidis G, Katsarakis N and Koudoumas E, Effect of O2 flow rate on the thermochromic performance of VO2 coatings grown by atmospheric pressure CVD. *Physica Status Solidi (c)*, **2015,** 12, 856-860

[45] Andersson G, Studies on vanadium oxides .1. phase analysis. *Acta Chemica Scandinavica*, **1954,** 8, 1599-1606

[46] Chirayil T, Zavalij P Y and Whittingham M S, Hydrothermal synthesis of vanadium oxides. *Chemistry of Materials*, **1998,** 10, 2629-2640.

[47] Wriedt H, The OV (oxygen-vanadium) system. *Bulletin of Alloy Phase Diagrams*, **1989,** 10, 271-27

[48] Nakano M., Shibuya K., Okuyama D, Hatano T , Ono. S., Kawasaki M, Iwasa Y and Tokura Y, Collective bulk carrier delocalization driven by electrostatic surface charge accumulation. *Nature*, **2012,** 487, 459-462.

[49] Rozgonyi G A and Hensler D H, Structural and Electrical Properties of Vanadium Dioxide Thin Films, *Journal of Vacuum Science and Technology* , **1968,** 5, 194.

[50] Morin F, Oxides which show a metal-to-insulator transition at the Neel temperature. *Phys. Rev. Lett.* **1959,** 3, 34.

[51] Eyert V , The metal-insulator transitions of VO2: A band theoretical approach, *Ann. Phys. (Leipzig)* , **2002**,11, 9.

[52] Goodenough J B, The two components of the crystallographic transition in VO2, *J. Solid State Chem.* **1971**, 3, 490.

[53] Liu K, Lee S, Yang S, Delaire O, and Wu J, Recent progresses on physics and applications of vanadium dioxide, *Mater. Today* **2018**, 21, 875.

[54] Yang Z, Ko C & Ramanathan S, Oxide electronics utilizing ultrafast metal insulator transitions. *Annu. Rev. Mater. Res.* **2011**, 41, 337–367

[55] Qazilbash M M et al. Mott transition in VO2 revealed by infrared spectroscopy and nano-imaging. *Science* **2007,** 318, 1750–1753.

[56] Jeong J et al. Suppression of metal-insulator transition in VO2 by electric field–induced oxygen vacancy formation. *Science* **2013**, 339, 1402–1405.

[57] Biermann S, Poteryaev A, Lichtenstein A, & Georges A. Dynamical singlets and correlation-assisted peierls transition in VO2. *Phys. Rev. Lett.* **2005**, 94, 026404 .

[58] Sunet Y. al. New aspects of size-dependent metal-insulator transition in synthetic single-domain monoclinic vanadium dioxide nanocrystals. *Nanoscale* **2011**, 3, 4394–4401

[59] Li X. et al. Direct evidence of tungsten clustering in W0.02V0.98O2 thin films and its effect on the metal-to-insulator transition. *Acta Mater*. , **2014**, 80, 16–24

[60] Devthadeand V and Lee S, Synthesis of vanadium dioxide thin films and nanostructures *J. Appl. Phys.* **2020**, 128, 231101

[61] Strelcov E, Lilach Y, and Kolmakov A, Gas Sensor Based on Metal-Insulator Transition in VO2 Nanowire Thermistor, Nano Lett. **2009**, 9, 2322–2326.

[62] Everhart C R and MacChesney J B, Residual Resistivity and Kohler's Rule in Nickel, *J. Appl. Phys.*, **1968** 39, 2872–2874.

[63] Goodenough J B, The two components of the crystallographic transition in VO2, *J. Solid State Chem*., **1971**, 3, 490–500

[64] Wentzcovitch R M, Schulz W W and Allen P B, *Phys. Rev. Lett*. **1994**, 72, 3389.

[65] Cavalleri A, Dekorsy T, Chong H H, Kieffer J C and. Schoenlein R W, Evidence for a structurally-driven insulator-to-metal transition in VO2: A view from the ultrafast timescale. *Physical Review B*, **2004**,70 p. 161102

[66] Stefanovich G,Pergament A and Stefanovich D, Electrical switching and Mott transition in VO2. *Journal of Physics: Condensed Matter*, **2000**, 12 , 8837

[67] Haverkort M W, Hu Z, Tanaka A, Reichelt W, Streltsov S V, Korotin M A, Anisimov V I , Hsieh H H, Lin H J, Chen C T, Khomskii D I and Tjeng L H, Orbital-Assisted Metal-Insulator Transition in VO2. *Physical Review Letters*, **2005**, 95, 196404:1-196404:5.

[68] Nishikawa M, Nakajima T, Kumagai T, Okutani T, and Tsuchiya T, Ti-Doped VO2 Films Grown on Glass Substrates by Excimer-Laser-Assisted Metal Organic Deposition Process *J. Appl. Phys*. **2011,** 50, 01BE04

[69] Gu Q, Falk A, Wu J, Ouyang L, and Park H, Current-Driven Phase Oscillation and

Domain-Wall Propagation in WxV1-xO2 Nanobeams, *Nano Lett.* **2007**, 7, 363–366.

[70] Cyrot M, Theory of Mott transition: Applications to transition metal oxides. J. Phys. (France) **1972**, 33, 125–134.

[71] Tang C, Georgopoulos P, Fine M E, Cohen JB, Nygren M, Knapp GS, and Aldred A, *Phys. Rev. B* **1985,** 31, 1000 .

[72] Zhang J, He H, Xie Y and Pan B, Theoretical study on the tungsten-induced reduction of transition temperature and the degradation of optical properties for VO_2, *J. Chem. Phys*. **2013**, 138, 114705 .

[73] He X, Zeng Y, Xu X, Gu C, Chen F, Wu B, Wang C, Xing H, Chen X and Chub J, Orbital change manipulation metal–insulator transition temperature in W-doped VO2, *Phys. Chem. Chem. Phys.*, **2015**,17, 11638.

[74] Booth JM & Casey P, Anisotropic Structure Deformation in the VO2 Metal Insulator Transition. *Phys. Rev. Lett*. **2009**,103, 086402.

[75] Tan X, Yao T, Long R , Sun Z, Feng Y , Cheng H, Yuan X , Zhang W, Liu Q , Wu C , Xie Y & Wei S , Unraveling Metal-insulator Transition Mechanism of VO2 Triggered by Tungsten Doping *Sci. Report.* **2012** 2 : 466

[76] Li G, Guo C, Yan M, Liu S, CsxWO3 Nanorods: Realization of Full-Spectrum-Responsive Photocatalytic Activities from UV, Visible to near-Infrared Region. *Appl. Catal., B* **2016**, 183, 142−148

[77] Futrell B J, Ozelkan E C, Brentrup D, Bi-Objective Optimization of Building Enclosure Design for Thermal and Lighting Performance. *Build. Environ*. **2015**, 92, 591−602

[78] Kodaira, T.; Suzuki, Y. H.; Nagai, N.; Matsuda, G.; Mizukami, F. A Highly Photoreflective and Heat-Insulating Alumina Film Composedof Stacked Mesoporous Layers in Hierarchical Structure. *Adv. Mater*. **2015**, 27, 5901−5905

[79] Yeh P, Yariv A, and Hong C S, Electromagnetic propagation in periodic stratified media. I. General theory, J. Opt. Soc. Am., **1976**, 67, 423-438 .

[80] John S, Strong localization of photons in certain disordered dielectric super lattices, *Phys. Rev. Lett.* **1987,** 58, 2486

[81] Wang Z, Liu D, Special kind of photonic crystals with omnidirectional bandgaps, Journal of the *Optical Society of America B* **2006**, 23, 12, 2601–2604

[82] Jakubiak R, Bunning T.J, Vaia R A, Natarajan L V, Tondiglia V P, Electrically switchable, one-dimensional polymeric resonators from holographic photo polymerization: a new approach for active photonic bandgap materials, *Adv. Mater*. **2003**, 15, 241 – 244.

[83] Kazmierczak T, Song H, Hiltner A, Baer E, Polymeric one-dimensional photonic crystals by continuous coextrusion, *Macromol. Rapid Commun*. **2007**, 28, 2210 – 2216.

[84] Joannopoulos J D, Johnson S.G, Winn J.N, Meade R.D., Photonic Crystals: Molding the Flow of Light, *Princeton University Press*, **2011**.

[85] Friz M and Waibel F ,*Optical Interference Coatings, Springer*, **2003**, pp. 105-130

[86] Lin S Y, Fleming J G, Hetherington D L, Smith B K, Biswas R, Ho K M, Sigalas M M, Zubrzycki W, Kurtz S R, Bur J, A three dimensional photonic crystal operating at infrared wavelengths, *Nature*, **1998**, 394, 25

[87] Lee J H, Thomas E L, "Photonic crystal" Encyclopedia of Polymeric Nanomaterials, Springer, **2014**

[88] Florescu M, Busch K and Dowling J P, *Phys. Rev. B,* **2007,** 75, 201101

[89] Shklover V, Braginsky L, Witz G, Mishrikey M, and Hafner J C, *Comput. Theor. Nanosci*. **2008**, 5, 862

[90] Lau W T, Shen J T and Fen S, Universal features of coherent photonic thermal conductance in multilayer photonic band gap structures *Phys. Rev. B*, **2009**, 80,155135

[91] Yang H, Yu JH, Jeong RH, Boo JH, , Enhanced electrochromic properties of nanorod based WO3 thin films with inverse opal structure. *Thin Solid Films* **2018,** 660,596–600

[92] Zhu M, Qi H, Wang B, Wang H, Zhang D, Lv W, , Enhanced visible transmittance and reduced transition temperature for VO2 thin films modulated by index-tunable SiO2 anti-reflection coatings. *RSC Adv*, **2018**, 8, 28953–28959

[93] Cao Z, Lu Y, Xiao X, Zhan Y, Cheng H, Xu G () Tunable simultaneously visible-light and near-infrared transmittance for VO2/SiO2 composite films to enhance thermochromic properties. Mater Lett, **2017**, 209,609–612

[94] Zhang J, Wang J, Yang C, Jia H, Cui X, Zhao S, Xu Y () Mesoporous SiO2/VO2 double-layer thermochromic coating with improved visible transmittance for smart window. *Sol Energy Mater Sol C*, **2017**, 162, 134–141

Chapter 2
Experimental, Fabrication and Characterization Techniques

2.1 Introduction

This Chapter gives the brief description of the technical aspect of fabrication process of photonic crystals tuned for visible to near infra-red region of the optical wavelengths. We will discuss the synthesis and characterization methods used for making the nanostructure of Vanadium Dioxide along with its polymorphs and carbon dot. we will be discussing the operating mechanisms of characterizing tools in brief. We will also discuss the transfer matrix method in brief which is used to simulate photonic structures with MATLAB code. This thesis will deal with optical performance of hybrid structures of VO_2 and W-doped VO_2 with 1-D Photonic crystal structures. We will specifically discuss optical experiments such as temperature dependent optical transmissions and specular reflection spectroscopy to characterize VO_2/Photonic crystal hybrid structure. We have also performed photoluminescence experiments to study the performance of carbon dot with Photonic crystal based devices. This chapter gives the brief description of that as well.

2.2 Design and fabrication of 1-D Photonic crystals

In this section we will discuss the design and fabrication of 1D photonic crystal in entire wavelength region. Photonic crystals are mainly described as the study of stationary states of optical electromagnetic waves [1]. With the knowledge of solid state physics and Maxwell's equations, one can anticipate the behavior of light in terms of band theory [2]. There are various methods to calculate the band structure of photonic crystal such as plane wave method (PWM) [3], Finite difference time domain method (FDTD) [4] and transfer matrix method (TMM) [5]. All

these methods give results which are in good match with experimental data. The first method i.e., PWM considers the solution of Maxwell's equations to be the linear combination of plane waves, this method gives the Eigen values of infinite photonic crystal with a defect [6 -7], this technique incorporates both simplicity and viability in a complex problem. It can map the detailed energy diagram for any periodic dielectric arrangement, however, this method has inability to efficiently study the crystals having frequency dependent dielectric functions such as metals. This method is best suited for perfectly periodic structures, when a defect is introduced in the structures, the energy diagram calculation become time consuming and hectic. TMM typically used to calculate the optical absorption parameters in a multilayer structure by applying the electromagnetic boundary conditions through a transfer matrix at each layer [8]. This approach has several advantages over the plane wave method, the main advantage is that while plane wave method fixes k value and search for all value of possible ω, in TMM calculations for a particular ω, it calculates all possible values of k. This makes this method to work even for dielectric functions is some complex function of frequency, i.e., metal. But TMM calculation gives no information about temporal fields inside the crystal structures which is a vital information while designing splitter. couplers etc. whereas, the FDTD method is direct method which uses integration over Maxwell's equation to solve the photonic bands for much complex structures [9] and this method is mainly used for simulating nonlinear materials. The time stepping method used here is fully explicit, hence it completely avoids the problems associated with matrices and simultaneous equations as in both methods state above. However, to calculate transmission and reflection coefficients, this method is more tedious and sensitive to errors than the TMM method. In this thesis, we have used the TMM, which is implemented using MATLAB for structures having many layers. We can easily calculate the reflection and transmission coefficients with this method for any multilayer structure. The code is added into the appendix of this chapter. We have used radio frequency (RF) magnetron sputtering to fabricate the 1D Photonic crystal. This is a well-known and very efficient tool that we have used to fabricate 1D Photonic crystals which are also known as distributed Bragg reflectors (DBRs). Now we discuss the working principle of magnetron sputtering in Brief in the next section.

2.3. Magnetron sputtering

Magnetron sputtering is the one of well-known technique used for physical vapor deposition to make thin films on various kind of substrates [10 - 11]. Magnetron sputtering is also used heavily as an important technique for industrial applications in the areas of wear – resistant coatings etc. [12]. With this technique one can deposit films with varying thickness from few nm to several μm. One of the major advantage of sputtering is that it is high vacuum based deposition system due to which chances of unintentional oxidation of samples are low. This makes this technique a highly desirable coating technique for microelectronic fabrication. Generally, the vacuum chamber is pumped to a gas pressure of 10^{-6} to 10^{-7} mbar [13]. Sputtering is one of the most convenient technique for the fabrication of photonic micro cavities, because of the ease of depositing layers of multiple materials within a single vacuum chamber. Moreover, it also provides good control of refractive index and thickness of each layer [14]. Sputtering system employ magnetrons which uses electric and magnetic fields which confine the charged plasma near the target surface. The target material is hit by the highly energetic plasma of the sputtered gas which is generally an inert gas, usually argon is used for this purpose. Upon hitting the target with energy greater than binding energy of the atoms in material, the target atoms come off the and undergo transition into the gaseous phase. Now the electrons which follow the helical path under the influence of magnetic field, undergo collision with gaseous atoms and formed the gas discharge known as plasma near the surface of target. Sputtering can be of various types depending upon the utility. Mainly there is DC sputtering, which uses the DC (Direct Current) source. DC sputtering generally employed on conductive materials [15]. It involves the DC gas discharge formed after ions hit the target which is kept at cathode. This positive charged discharge is accelerated towards the substrate which is kept at the anode. DC sputtering involves high power DC power source [16]. DC sputtering is beneficial in processing many large substrates. But to deposit thin films of dielectric insulting materials such as oxide DC sputtering cannot be used. To deal with this problem, radio frequency (RF) sputtering is used. In RF sputtering it consist cathode which is the target and anode, which is kept at series with blocking capacitor. The main function of capacitor is to behave as impedance matching network which controls the RF power to form plasma discharge [16]. RF sputtering is found to be useful for depositing insulting materials as it can avoid the charge build up over the target by alternating changing the anode – cathode sign with the frequency of 13.56 MHz Figure 2.1 (a) and (b) showing the Moorefield sputtering system ST80A

used to fabricate 1D Photonic crystals. This system is equipped with both DC and RF magnetron sputtering facility. Figure 2.1 (a) showing the schematic of both DC and RF sputtering.

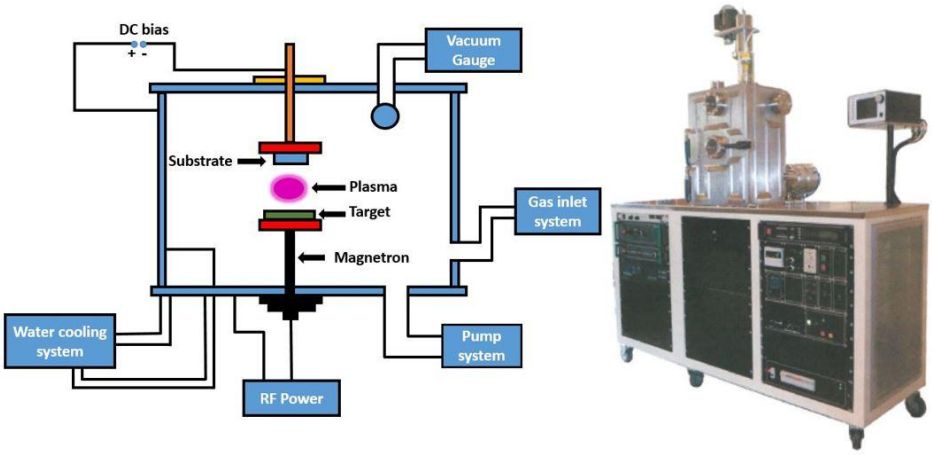

Figure 2.1. (a) Demonstrating the magnetron sputtering schematic diagram and **(b)** showing the actual RF and DC system used to fabricate photonic crystals for this thesis (Moorefield ST80A).

This magnetron sputtering system is installed with three magnetrons with sputter sources and it consists of variable height and variable head angle magnetrons. The system can reach to vacuum of 10^{-7} mbar as it is equipped with turbo molecular stage pump followed with backing pump. Along with it a variable height sample stage is attached to the system. In this system to control the deposition rate a thin film crystal monitor is attached. Although all the optimization to fabricate the 1D photonic crystals in tuned wavelength is done manually by fixing the RF power and distance between the magnetron and sample stage respectively and plasma time exposure. In this thesis, we use SiO_2, TiO_2 and Ta_2O_5 as target materials to fabricate 1D Photonic crystals. Very high quality thin films of these oxides with surface roughness in the range of ± 2 nm were fabricated. This surface roughness is measured with AFM. We have fabricated 1D photonic crystals tuned to optical wavelength varying from visible to infra-red by alternatingly depositing SiO_2/TiO_2 and SiO_2/Ta_2O_5 respectively. Figure 2.2 (a) showing the 1D Photonic crystals fabricated in the visible region as evident from their reflecting color in optical images with 2.2 (b) showing their reflectivity curve which reaches near to 100 %. 2.2 (c) showing the cross sectional view of these multilayer structures.

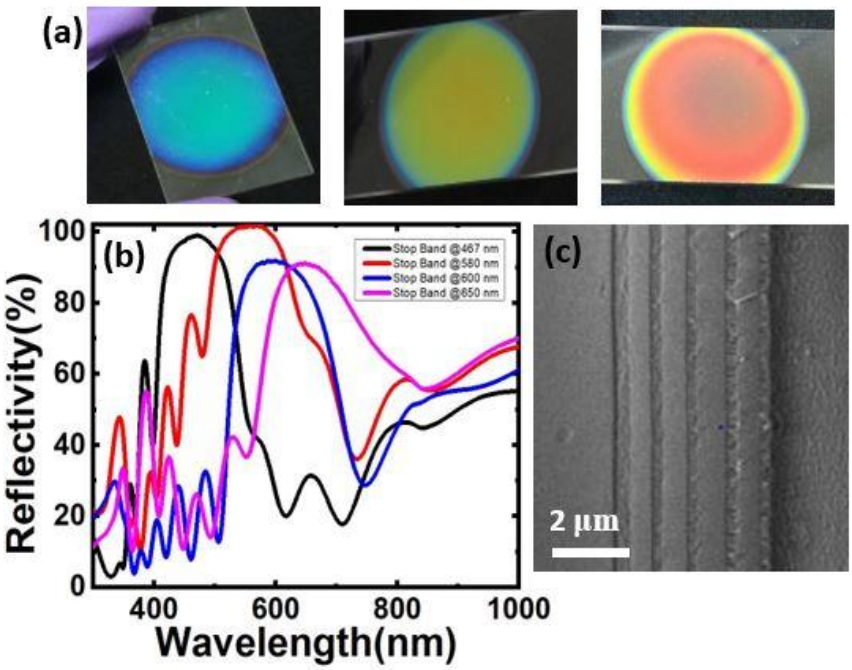

Figure 2.2 (a) Showing the optical images of 1D Photonic crystal in visible region **(b)** showing the respective reflectivity of a photonic crystals and **(c)** showing the cross sectional image of these multilayer photonic crystal fabricated with alternative layers of SiO_2 and TiO_2 respectively.

To fabricate smooth thin films with good reflective interface, we used an appropriate RF power at moderately low deposition rate. To fabricate metallic thin films of Ag and Au to form metallic cavities DC sputtering in the same system with different control unit is employed. Compared to the DC magnetron sputtering RF sputtering is quite complex and it equipped with more expensive instrumentation with many control parameters to take care. However, RF magnetron sputtering is found to be very convenient and suitable tool to fabricated high quality photonic crystals with wavelength varying from visible to Near infra-red [17]. This technique has an advantage of high deposition rates and forming high purity films with good adhesion with uniform large area deposition therefore, it is one of the most important tool for smart glass industry. Also it is widely used in fabrication of thermochromics materials for smart window applications [18]. Now to characterize these photonic crystal we took specular reflection and transmission curves which we mainly collected using Perkin Elmer's Model-950 UV-VIS absorption spectrometer.

2.4. UV - VIS Optical Absorption Spectroscopy

UV - VIS spectroscopy also known in context of absorption spectroscopy and reflectance spectroscopy generally in region from ultraviolet to visible wavelength. It is a simplest and quite inexpensive analytical technique extensively used in various areas of science from fundamental to broad applications. The working principle of UV - VIS spectroscopy is based on light matter interaction, when light is absorbed by the material under study it undergoes excitation and de-excitation which leads to the formation of distinct electronic spectra [19]. Usually the electrons present inside the compound absorbs the Ultraviolet radiation undergoes the electronic transitions from relativity lower ground state to a relativity high energy excited state which gives the idea about the electronic structure of the compound. UV – VIS spectroscopy is usually carried out in solution. To study carbon dot and vanadium dioxide nanoparticle, we have used optical absorption technique which is based on Beer-Lambert law [20]. This states that the optical absorbance is directly depends on concentration of absorbing compound. It gives the mathematical and physical picture of light matter integration for gases and liquid phase in the entire electromagnetic spectrum [21] Figure 2.3 showing a schematic diagram of UV-VIS Spectrometer for liquid and translucent samples.

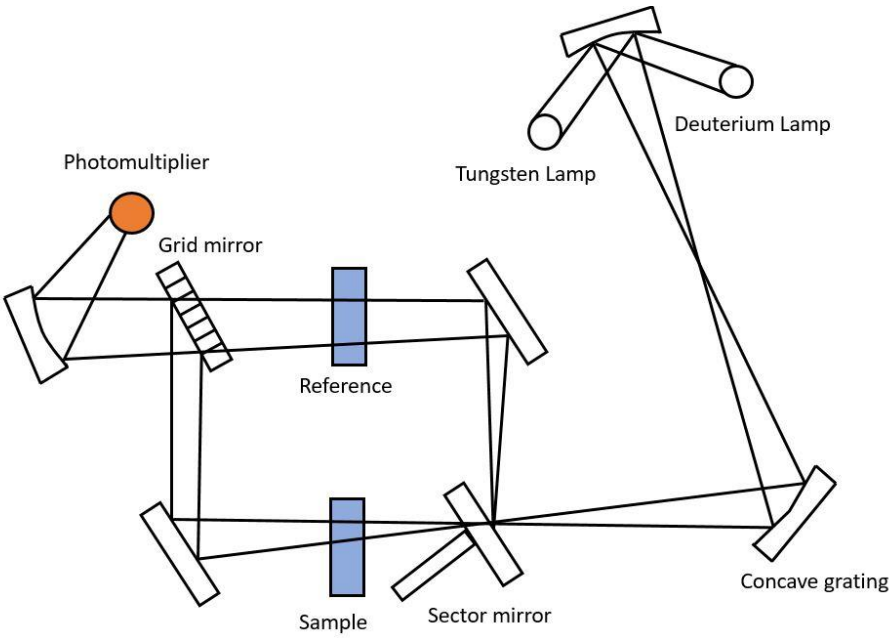

Figure 2.3. Showing the typical UV-VIS Spectroscopy diagram for solution samples.

It depends on path length which is the width of cuvette. The absorption coefficient given as ɑ (λ) gives the idea that how far an electromagnetic wave can penetrate before it get absorbed. For the case of vanadium dioxide, similar to semiconductors have a narrow edge for absorption coefficient across the MIT (Metal to Insulator) i.e., photons with energy less than band gap cannot excite electrons from valance band to conduction band and as a result it results in no light absorption. Therefore, absorption coefficient ɑ(λ) determines the intensity attenuation of the light passing through a compound [22] and can be expressed as,

$$\alpha(\lambda) = \frac{-\,d\,[I_0]}{I_0\,dx}$$

The absorption coefficient is related to extinction coefficient by the formula,

$$\alpha(\lambda) = \frac{4\pi\kappa}{\lambda}$$

Where κ is the extinction coefficient and λ is the wavelength of light define I_0. Knowing the following parameters one can calculate the absorbance of the solutions. But above method is applicable only to dilute solutions. We have calculated the absorption spectrum of Vanadium dioxide nanoparticles across the MIT transition with ethanol as solvent keeping the account of

concentration factor. To characterize the dielectric multilayer samples also known as Bragg mirrors, as these are very high reflectivity at stop band wavelength due to subsequent coherent interference from the layers. To characterize these, absolute reflection measurement using integrating Sphere is done with a high accuracy. For these measurements Shimadzu UV –VIS spectrometer 3600i Plus is used. A typical schematic diagram of an integrating sphere is shown in figure 2.4 (a)

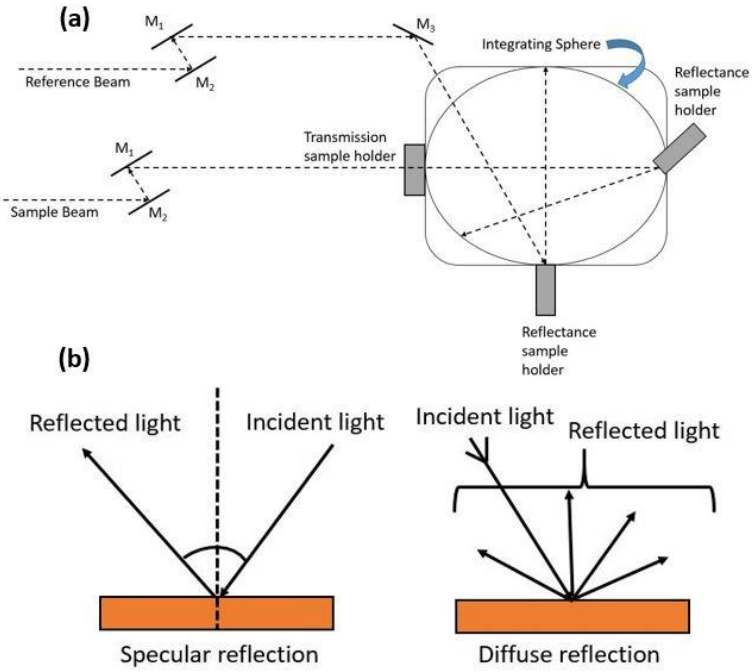

Figure 2.4. (a) Showing the schematic of integrating sphere measurement of solid thin films and (b) showing the specular and diffuse reflection from the surfaces [23].

An integrating sphere compromise of spherical cavity coated with highly reflective materials known as barium sulfate. Light undergoes multiple reflections until the detector collects the reflected light [23]. Reflection measurement is also characterized as diffuse and specular reflection, depending on how the light fall on the sample and reflected through its surface. Generally Specular reflection defined when reflected light is symmetrical to incident light w.r.t the normal line whereas in case of diffuse reflection, incident light scattered in all directions upon reflection through the surface as shown in the figure 2.4 (b). Reflectance and transmittance spectra for Bragg mirrors are obtained through specular mode of reflection. As specular reflection is

usually done on samples having smooth and polished surface. Samples which have rough surfaces usually measured by diffuse reflectance mode as samples undergoes diffuse reflectance are simultaneous scatters and absorb the electromagnetic wave. To study the VO_2/DBR hybrid structure high temperature reflection measurement is done. As of our knowledge there is no commercial spectrometer which can measure specular reflection with increasing temperature of substrate, therefore we have done these measurements on our home build setup consisting of manual optical assembly which will explain further.

2.5. High temperature Reflection Spectroscopy

Vanadium Dioxide (VO_2) and it's polymorphs undergoes the reversible metal to insulator (MIT) transition around critical temperature of 68°C [24]. Such MIT transition leads to abrubt change from the infrared (IR) transparent semiconduting M state to the IR blocking metallic R state. Therefore with change in temperature around the critical temperature there is decrease in transmission in VO_2 nanoparticles thin films. To measure the change in reflection and transmission with tempearture in VO_2 thin films when incorporated with Bragg reflectors, we have employed a home made experimental setup as shown scematic diagram in figure 2.5.

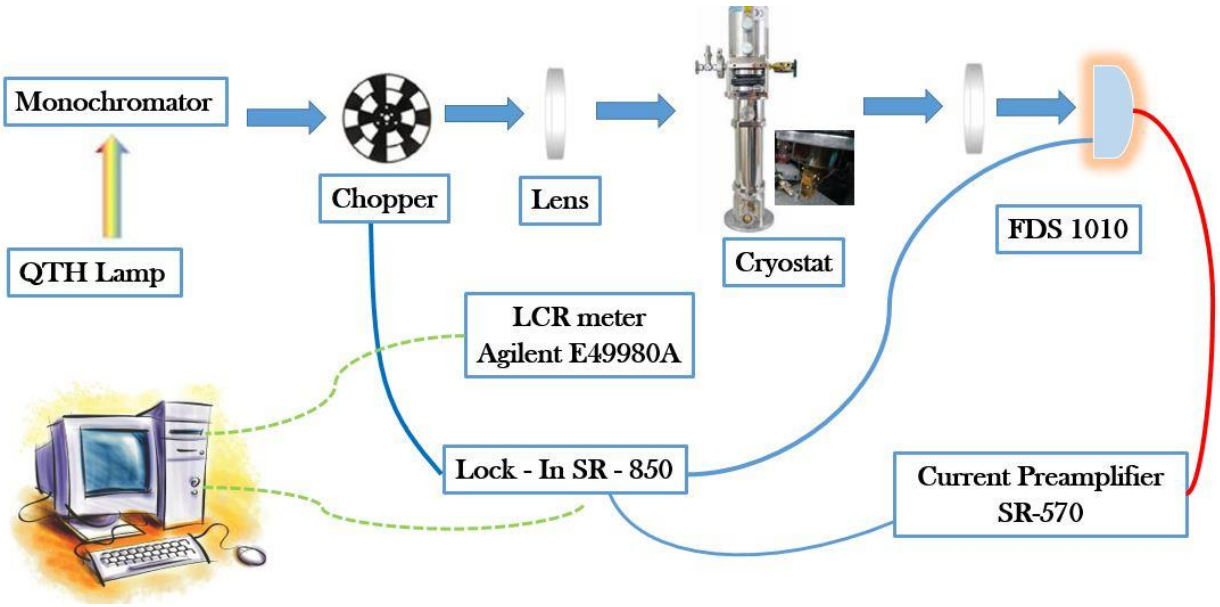

Figure 2.5 Schematic diagram of High temperature Specular reflection and transmission at high temperature.

Bragg reflectors are sensitive to the angle of incidence therefore it is important to do the measurement specuarly with incident light falling normally on the sample. And As of our knowedge there is no spectrometer in and around the world which can measure the specular reflection with increase in temperature of thin films mode inside the integrating sphere. Therefore, we have measured our samples on our home build setup which consist of Acton Research's SP2555i monochromator which can scan a wavelength ranges from 900 – 2500 nm. Light then passes through the chopper which inturn passes through the lens assembly which focues the light into the sample which is kept inside the customised copper sample holder in a ARS CS204-DMX-20 closed cycle cryostat from advanced research systems. The temperature of the cryostat in which the sample is placed is controlled with Lakeshore (Model – 340) temperatre controllers. Finally the specularly reflected and transmitted light is detected through the detector FDS 1010. preamplifier and LCR meter are connected in series for the signal detection. We have also performed these experiment on VO_2/DBR samples fabricated over PET substrate subjected to compressive bending, while structure is compressed it is difficult to measure reflection and transmission though the structure in any spectrometer but our home build set up provides the ease of measurement even when structure is subjected to compressed bending. Therefore, in these experiments we have observed the significant decrease in transmission with increase in temperature with 1-D photonic crystal incorporated with VO_2. While doing the measurement the spot size of light is kept to be of few millimeters so that spectral shape will be retained as the accumulating effect of VO_2 nanoparticles will be considered as the reflectivity decreases with increase in temperature (relevant data is shown in chapter 3).

2.6. Scanning Electron Microscopy

SEM is classified as a family of electron microscope which scan the surface of the specimen with highly energetic beam of electrons and creates an image of the object [25]. It's a most important technique to study materials in a nondestructive way. Scanning electron microscope utilizes high energy electron beam to generate signal by the interaction of electrons beam with the atoms of specimen under study. Figure 2.6 Illustrating the different signals produced upon interaction of electron beam with specimen sample. This interaction contains the information about the morphology, crystalline structure and chemical compositions [27].

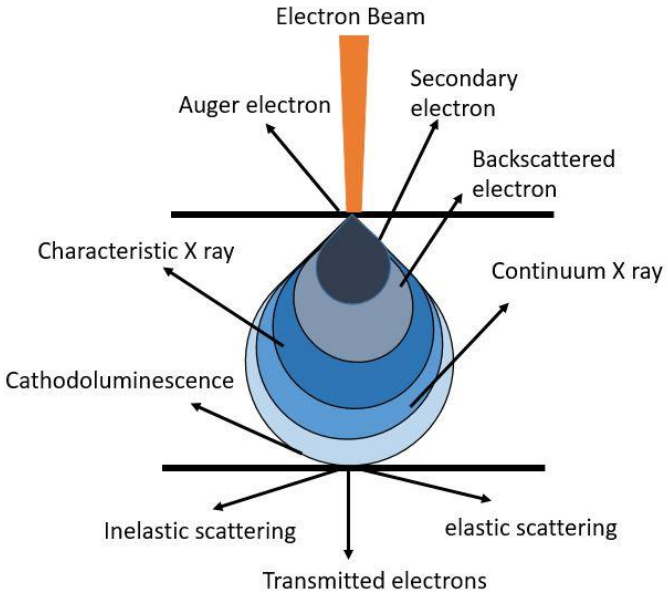

Figure 2.6. Illustrating the interactions of electron beam with specimen sample with various signals generated

Depending on applied accelerating voltage to electron beam and density of the specimen under study many interactions produced such as, secondary electrons (SE), backscattered electrons (BSE) and characteristic X-rays are produced. The penetration of electron beam can occur up to the depth of few microns [27]. Signals due to Secondary electrons and characteristic x-ray are the result of elastic collision between electron beam and atoms of specimen. Apart from that auger electrons, characteristic X-rays and bremsstrahlung radiation are also produced in this interaction. Now characteristic X-rays provides the information about elemental details. BSE have higher energy than secondary electrons (SE) therefore it penetrates deeper region of the specimen hence gives the analytical idea about the element distribution. Whereas, secondary electrons are generated from the atoms of specimen itself after the electron beam and sample specimen undergoes the inelastic collision. Secondary electrons are less energetic as of the order of 50 eV. hence it has limited mean free path therefore it can penetrate up to the depth of few nanometers in the specimen sample. Hence secondary electrons mainly contribute in topography with resolution near or below 1 nm respectively. therefore, secondary electron provides the most important signal for the studies in this thesis. Secondary electrons (SE) can be further classified as SEI, SEII, SEIII and SEIV. This classification is based on the generation procedure of these secondary electrons. SEI carries maximum information, as it is produced with primary impact of electron beam with

specimen. With the progress in technology, to achieve high resolution images Filed emission SEM came into picture. The main difference between a conventional SEM and FESEM is in process of generation of electron beams using field effect guns [28]. The schematic diagram of FESEM is shown in figure 2.7 illustrating the main components.

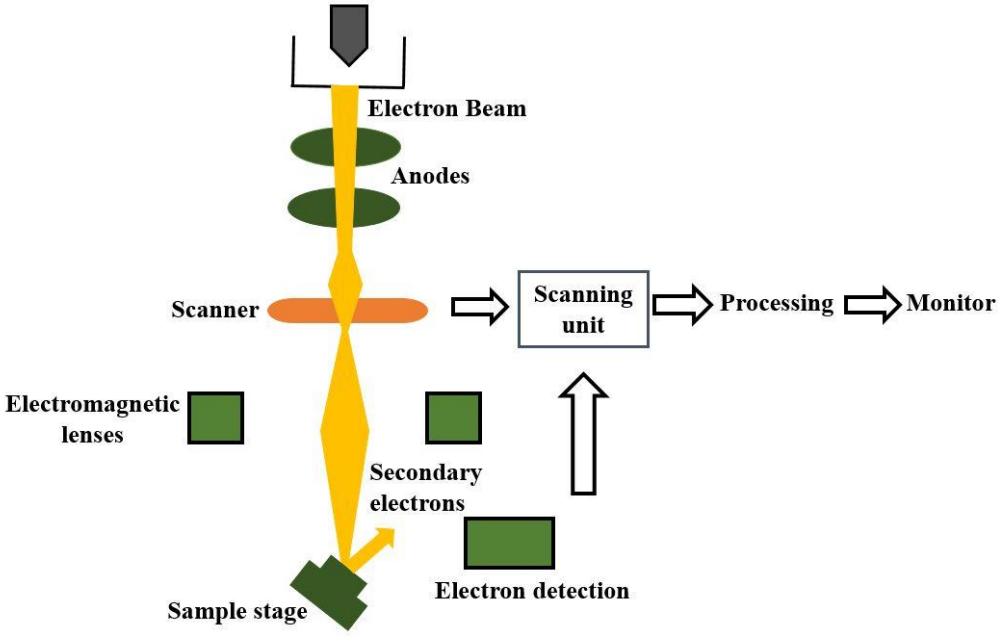

Figure 2.7 Showing the basic construction of FESEM

FESEM consist of the electron gun source between two anode plates. The one anode plate is used to extract voltage, usually this extracted voltage rages from 3 - 5 kilovolts, second anode plate is used for accelerating voltage with electrons accelerated between 1 keV to 30 keV energy, this second anode plate controls the velocity of electrons to travel though the column. These anode plates played the role of electrostatic lens which ultimately focus the beam into the small area. Resolution is an important aspect in FESEM, which is defined as the capability of separating two closely spaced entities. Hence, accelerating voltage and crossover area of electron beam are most crucial factor which determines the resolution of FESEM. Higher is the accelerating voltage better is the point to point resolution of the FESEM. Generally, 30 kV accelerating voltage is used for point to point resolution. The second crucial parameter for resolution is beam crossover i.e. the diameter of the beam. To resolve the features of the specimen the diameter of the beam should be smaller than that of the feature. In field emission systems, electromagnetic lensing system is

employed to magnify the electron beams further. There is a circular magnetic field created by these electromagnetic lenses which condense the passing electron beam. By applying the current to the lensing system, the focal length of the lens can be changed. Therefore, field emission microscopes are one of highest resolution instrument. In this thesis all the characterization of Vanadium Dioxide and other material as well as cross section of DBR is determined using Carl Zeiss ULTRA PLUS FESEM which has the resolution of less than 1 nm. FESEM is installed with various metal aperture strips with different pinhole size. Generally small aperture is used for good resolution of image with good depth of field and less charging. Depth of field of FESEM is another important parameter which is defined as maximum change in topography of specimen while remain focused. The translation stage of the FESEM allow the stage to move in x, y and z direction. Z axis gives the working distance, i.e. the distance between the final lens and surface of specimen. To have an image over large change in z, the working distance should be large, with small aperture. After passing the electrons from the objective aperture, the electron beam goes to the final lens. Now final lens consists of raster coils through which the electron beam is scanned through the surface of specimen. Raster scan is synchronized with viewing screen scan; raster coils control the magnification. Magnification can be changed by scanning the shorter line on the specimen. Since size of CRT is fixed, information by the shorter scan is enhanced to fill the CRT viewing. In this thesis, high resolution images of Vanadium dioxide and carbon dots as well multilayer cross sectional view of Bragg Reflector are taken with high resolution SE detectors. In our case multilayer coated Silicon wafer was cleaved by pressing with diamond cutter at cleavage point. The figure in inset showing the cleaved silicon wafer. Figure 2.2 (c) shows the layers of SiO_2 and TiO_2 formed alternatively along with their thicknesses. Since SiO_2 and TiO_2 are oxides in nature which make it prone to accumulation of electrons on the surface of sample. To avoid this working voltage throughout the cross sectional measurement is kept in the range of 3kV which is quite low.

2.7. Transmission Electron Spectroscopy

Transmission electron microscope is a versatile and a powerful tool in the area of nanotechnology and material research [29]. Unlike SEM, the transmission electron microscope uses very highly energetic electrons which passes through very thin specimen, the interaction between electron and specimen gives the idea about the crystallographic structure. Figure 2.8

showing the schematic diagram of TEM consisting of an electron gun consisting of heated tungsten filament which focuses the electrons to the sample via condenser lenses. Magnetic lenses were used to focus the electron beam to the specimen sample. Vacuum of the system plays crucial role in forming clear image as molecules in the air can deflect the electrons passing through the column tube. Upon interaction of electrons with the specimen, the electrons were focused by magnetic lenses onto a fluorescent screen forming a large clear polychromatic image. Sample preparation is also important while performing TEM measurements. Denser the specimen, there are more chances that electrons will be scattered and only very few electrons hit the fluorescent screen and therefore results into darker image. On a contrast thinner sample will produce brighter image. In this thesis VO_2 and W - doped VO_2 nanoparticles were studied using JEOL JEM 1200 EX HRTEM instrument operated at the accelerating voltage of 200 kV. Sample for TEM and HR - TEM prepared by drop casting the diluted solution of VO_2 nanoparticles with ethanol drop casted on the TEM Copper grids (CF400-Cu, purchased from electron Microscopy Science) which were placed over a filter paper for at least 60 second and afterwards it is preserved in the vacuum desiccator. In this thesis Selected area diffraction (SAED) patterns are also studied using HRTEM, SAED is a technique which help to identify the crystal orientation, structure and symmetry of the nanostructures [30].

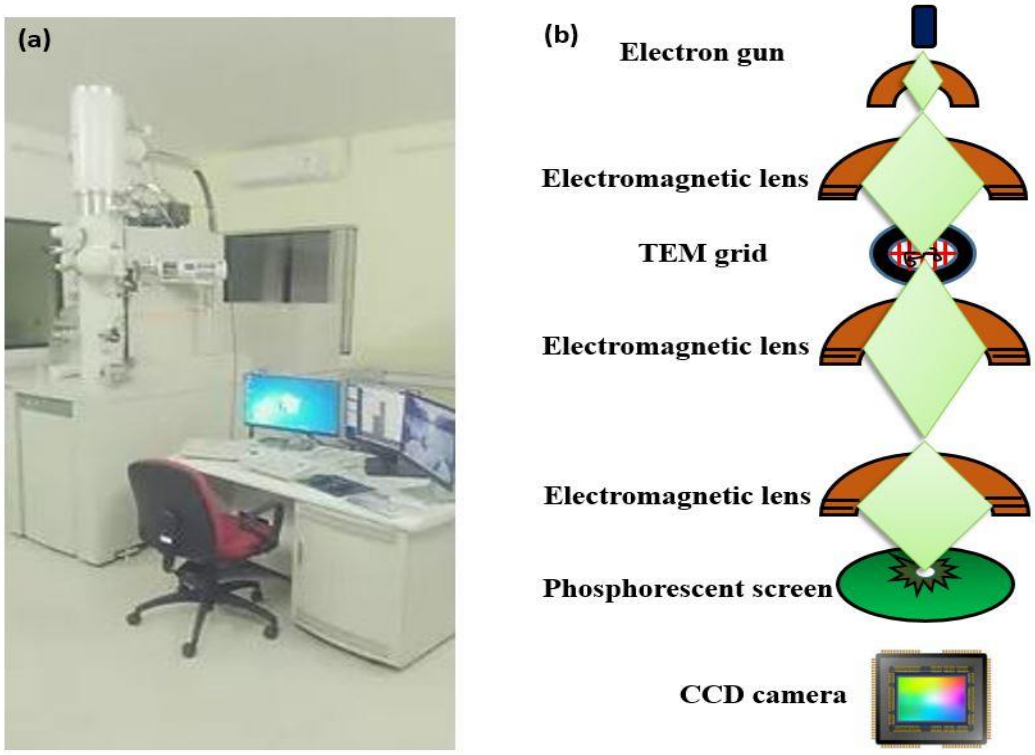

Figure 2.8 (a) Showing the actual TEM used to take images in this thesis with model no. **(b)** showing the schematic diagram of Basic instrumentation of Transmission electron microscope.

diffraction pattern area is typically of the size of few hundreds of nanometers where SAED pattern is observed. Spot pattern is formed upon the interaction of electrons single crystal sample and ringed shaped pattern is formed when interaction of electrons with powder samples takes place [31]. In this thesis high resolution transmission electron spectroscopy is done on VO_2 and W-VO_2 nanoparticles. high resolution imaging mode is a method of imaging the sample crystallographic structure at atomic level [32], it provides the image of atomic structure directly, which provides the resolution to lattice spacing. We have taken HRTEM image of VO_2 and W-VO_2 nanoparticles. Lattice fringes in the range of 3.2 A^o is observed. Diameter of nanoparticles is measured with 'ImageJ' software. This diameter is measured repeatedly on many VO_2 nanostructures and an average value of diameter is given to minimize the error. Figure 2.9 showing the TEM and HRTEM image of VO_2 nanostructures synthesized in our lab.

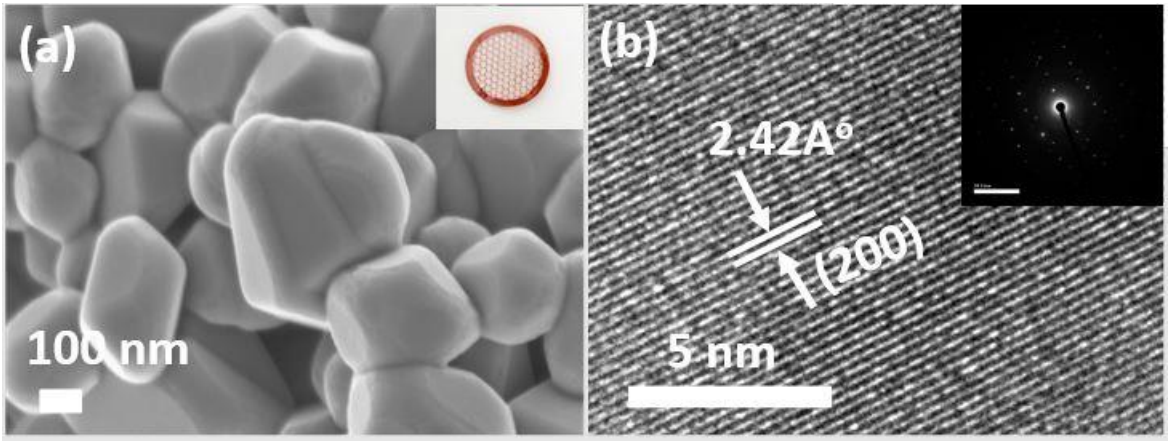

Figure 2.9 (a) Showing the Size of VO_2 nanoparticles which varies from 100 -150 nm with inset showing the Cu TEM grid used and **(b)** showing the HR TEM image with lattice spacing of 2.42 A^o with respective plane

2.8. X – Ray Diffraction

2.8.1 The principle of X-Ray Diffraction

X- Ray diffraction is a well-known technique to study the atomic and molecular structure of a crystal [33] and it is also an important technique to determine sample composition and phase purity [34]. The basic principle of X-Ray diffraction can be understood with Bragg's Law. In

general X-rays produced by cathode tube, generates monochromatic radiation and collimated towards the sample. After X-Ray's passes through the sample, it bounces back from the atoms at some angle theta also known as diffraction angle as shown in figure 2.10. These beams will undergo constructive interference, although few beams also undergo destructive interference but when the all reflected waves arrive with the same phase it forms a large amplitude constructive reflected wave with following the Bragg condition given as,

$$2dSin\Theta = n\lambda$$

Where $2dSin\Theta$ is the path difference upon reflection. Where 'n' is an integer and λ is the X – Ray incident wavelength. XRD instrument consists of X-Ray diffractometer. This instrument also works on the principle of Bragg law, where monochromatic light is produced and impinged on the sample scanned in the range of 2Θ, then reflected X-ray intensity is detected. The X-rays are produced in a Cathode ray tube. A tungsten filament is heated which creates the electrons that are accelerated towards the anode material. Usually Anode material are Cu, Co, Mo etc.

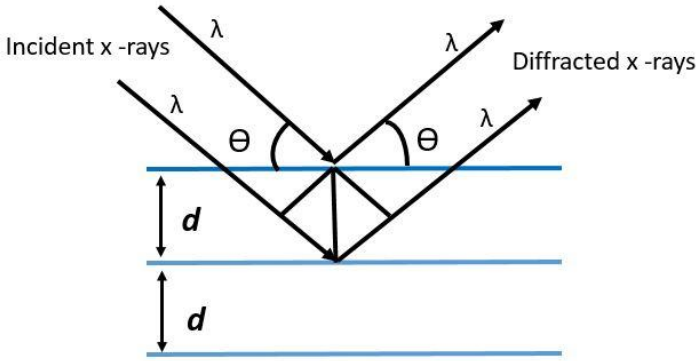

Figure 2.10 Showing the schematic of X-rays following Bragg Law

Upon heating the electrons from the inner shell removed and electrons from the higher shell come down to hold their vacant place which result in the emission of X – Ray characteristic from the anode material, K_{α} being the most common characteristic X-ray. A Schematic diagram of typical diffractometer is shown in figure 2.11

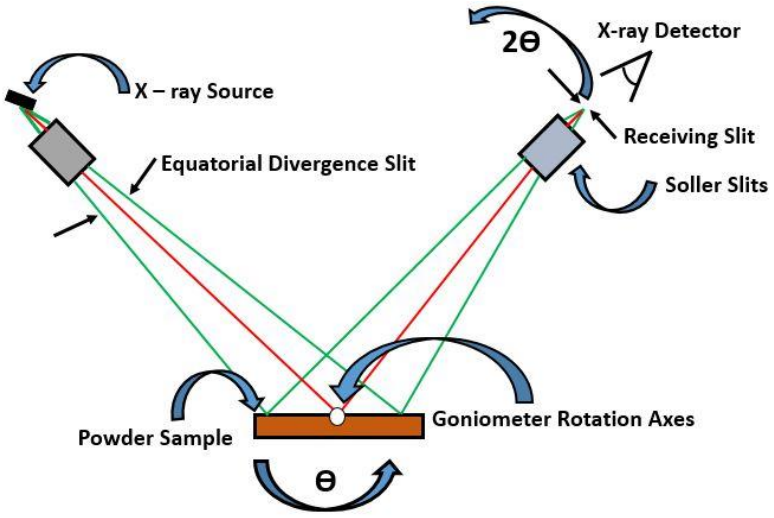

Figure 2.11 Showing the typical schematic diagram of X- Ray Diffractometer

Here Detector and the X-ray tube are connected to goniometer rotation stage which rotates the arms through the scan of 2Θ synchronously [35]. The X-ray source produce the x-rays which falls on the sample and get reflected towards the detector which is placed at the same angle as that of the tube but in the opposite side (see the figure 2.11). When incident X-ray reflected from the sample following the Bragg condition, constructive interference takes place and the peak position and intensity is measured at the detector. Generally, for typical powder x-ray diffraction the scan angle, 2Θ is varied from 5^o to 70^o. In this thesis all the structural analysis for VO_2 and W-VO_2 are done using Bruker D8 advanced X-ray diffractometer with Cu - K_α with $\lambda = 0.154$ nm as the source. Now to analyze the size of crystallites, broadening in peaks due to instrument [36 - 37] and specimen needs to be deconvoluted. Broadening related to the X ray instrument usually associated with finite size of the X-ray source, radiation from the source not fully monochromatic rather have some width to the wavelength, sample surface and divergence in axis of incident X-ray beam [38] are the main contributor to X-ray peak broadening associated with instrument. But with the advancement in technology the broadening due to instrument are negligible compared to Broadening contributed by the sample itself which is mainly due to uneven size of crystallites, distortion in crystal lattice usually known as micro strain or may be due to gradient in concentrations of non- stoichiometric compounds. The peak broadening in the XRD curves gives the estimation of the size of crystal grains using Scherrer equation [39]. Scherrer equation quantitatively describes the relation between diffraction peak Full width half maximum (FWHM)

and size of crystal grain. Scherrer equation is applicable to crystallite size < 200 nm due to diffractometer resolution limit [40].

2.8.2 Determination of Crystallites size

As the broadening of the peak increases with increase in size of crystal grains. The Scherrer equation gives the relation between crystal size and the broadening of diffraction peak as,

$$D = \frac{K\lambda}{\beta Cos\Theta} \quad (1)$$

Where 'D' is the size of Nano crystals, K is the dimensionless shape factor with typical value of 0.9 which is close to unity, λ is the wavelength of X-ray, β is the full width half maxima (FWHM) of the broadened peak and Θ is the diffracted angle. In chapter 3, VO_2 nanoparticles with different crystallinity are characterized by XRD measurements. Nanostructures Peak broadening depends upon crystallites morphology and size. In chapter 3 we have reported that, moderately crystalline VO_2 nanoparticles peaks are broader than the highly crystalline VO_2 nanostructure. And as observed from FESEM images moderately crystalline VO_2 nanostructures are larger in size as compared to highly crystalline nanostructure.

2.8.3 Strain effect on broadening

The second major reason of X-ray peak broadening due to sample are inhomogeneous strains [41]. figure 2.12 (a) depicting the single crystallite undergoing the Bragg diffraction. If this single crystallite undergoing the homogenous strain as shown in figure 2.12 (b), this will reduce the lattice spacing 'd' by 'δd 'and increase the Bragg peak from angle Θ to δΘ which means there is shifting in Bragg peaks but there will no broadening. Therefore, this strain known as homogenous as all crystallites are strained by same amount. When the all crystallites were presented to different amount of strain, this shift in the Θ would be a variable shift as shown in figure 2.12 (c) and the single shift in spot occur as shown in figure 2.12 (b) would be a series of continuous spots as shown in figure 2.12 (c) which leads to broadening in X ray peak due to single crystallite under inhomogeneous strain. This is possibly because of the presence of defect in crystallite or the defect can be interstitial, dislocation etc. which created inhomogeneous strain in

crystallite and causes broadening in X-ray peaks. Now the Bragg law and inhomogeneous strain can be correlated with formula,

$$D = C\,\varepsilon \tan\theta \qquad (2)$$

C is a constant has value between ~ 4 or 5. By combing the equation (1) and (2) and convoluting according to Williamson – Hall equation [42] we can calculate the size of strained crystallites. Warren- Averbach method [43] is another method which can be used to calculate the size of the crystallites knowing the peaks intensities in terms of Fourier transform.

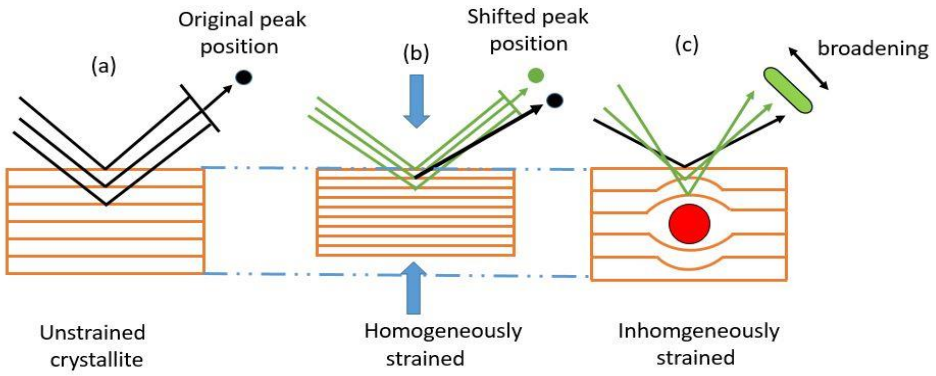

Figure 2.12 (a) showing the crystallite under no strain (b) showing the crystallite undergoes the homogenous strain and (c) showing the crystallite undergoes the inhomogeneous strain

2.9. Micro - Photoluminescence spectroscopy

Photoluminescence spectroscopy is a widely used spectroscopy to study the optoelectronic properties of semiconductors [44 - 47]. In general Photoluminescence categorized as fluorescence and phosphorescence [48] which is a contactless method to study the samples in a nondestructive way. In this thesis we mainly discuss the fluorescence. Photoluminescence spectroscopy uses the photons which were absorbed by the material and absorbed energy excites the electrons into the excited states. These excited electrons return to the ground state when losses energy, this lost energy which is released includes the light emission when a radiative process is involved in the decay process. The energy level difference of excited and ground state is directly related to the energy of the emitted photons in the radiative process hence the emitted light is lower in energy

than the excitation photon as depicted in figure 2.13. In Photoluminescence spectroscopy the emitted photons generate an optical signal which convoluted into spectrums of intensity versus wavelength.

Conventional PL spectroscopy is employed to study the bulk materials where spatial resolution is not needed. Therefore, the main idea of a micro photoluminescence is that the spot size of the excitation source which excites the sample is focused down to the size of wavelength scale i.e. size of the spot of few microns [49] and is focused to the detector.

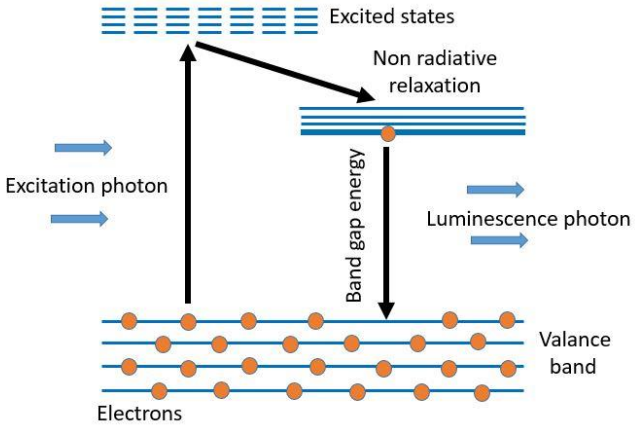

Figure 2.13 Showing the conventional photoluminescence excited with photons resulting in luminescence from radiative recombination

Figure 2.14 shows the Photoluminescence experimental setup which we used to measure the Photoluminescence from carbon dots samples. Now to study the effect and the intrinsic properties of carbon dots fluorescence enhancement due to 1D Photonic crystal structures, it is important to probe these Nano dots and Nano crystal individually at micron scale. The one way of investigating these is to use Micro-PL, as the name suggest the size of the spot should be less or nearly few micrometers. Figure 2.14 demonstrating the setup we used in our for Micro Photoluminescence measurement. Which includes Argon laser (488nm) as an excitation source, with lenses assembly including line filters and 50:50 beam splitter and 20 X objective lens and for possible detection of emitted light from the sample, we have used Portable compact CCD Spectrometer model no. CS200 thorlabs.

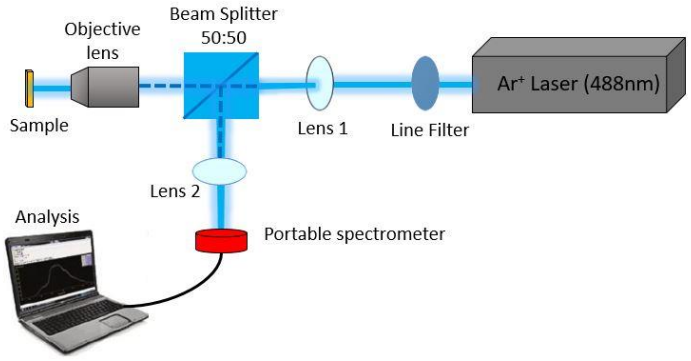

Figure 2.14 Showing the Micro Photoluminescence setup done in our lab

We have also tried to study the effect of polarization on these Carbon dots a nanocrystal by inserting s and p polarizers in between line filter and lens1. PL being the most sensitive technique for probing semiconductors and nanocrystals. Photoluminescence quantum yield is an important parameter to measure materials luminescence. Quantum yield of a material is defined as ratio of emitted number of photons per absorbed number of photons [50]. There are many methods which can be used to measure Quantum yield of a material, calculating the absolute value of Photoluminescence quantum yield is a tricky job, there are appropriate setups to measure it directly. One can use the comparative method to measure the quantum yield using the formula given as [51],

$$Q\ (sample) = Q\ (reference)\ \frac{I\ (sample)}{I(reference)}\ \frac{Absorbance\ (referecne)}{Absorbance\ (sample)}$$

Where Q is quantum yield of specimen and reference sample, I is the integrated fluorescence intensities of specimen and reference sample respectively. This method uses the quantum yield of known samples also known as standard references. This formula is applicable only when the specimen emission and absorbance wavelength is near to standard reference wavelengths of known quantum yield. We have used R6G as a known reference sample as the absorbance of carbon dot is similar to the R6G sample. From the above equation we have calculated the ratio of Quantum yields Sample with 1 D Photonic crystal to the sample over glass, we have observed a significant enhancement in Photoluminescence quantum yield in sample over 1D Photonic crystal as discussed in chapter 5.

2.10. Raman Spectroscopy

Raman spectroscopy is an important tool to characterize the materials molecular structure, as the name suggest it mainly works on the principle of Raman effect. The basic principle of Raman effect is scattered light interacting with specimen sample. The scattering of light can be elastic or inelastic. If the scattered light is at the same wavelength as of the incident one, then the scattering is known as elastic scattering which is also known as Rayleigh scattering and for inelastic scattering the scattered light is at different wavelength than the monochromatic incident light, it also known as Raman scattering. Raman scattering occurs due to vibrational molecules; therefore, Raman spectroscopy mainly determines the molecular vibrations [52]. Raman Signal being the weaker signal say about 0.000001 % of the incident light than the Rayleigh scattered light. Now to collect Raman signal, it is important to prevent the Rayleigh scattered light. It consists of high intensity laser beam, which excites the sample and the scattered light is detected through the spectrometer. The difference between the incident light energy and scattered light energy is known as Raman shift. The spectrometer is in turn gives the final curves between the scattered light intensity and Raman shift which is usually given in terms of wavenumber (cm^{-1}).

2.11 Summary

In this chapter, techniques used to fabricate 1D Photonic crystals and techniques used to characterized them such as uv- vis reflectance spectroscopy discussed briefly. Moreover, we have discussed all the necessary characterizations to characterize vanadium dioxide, tungsten doped vanadium dioxide and carbon dots. We have described the working principle of spectroscopies and microscopies such as scanning electron microscopy, transmission electron microscopy and x-ray absorption spectroscopy. Moreover, Certain optically homemade setup for characterization of VO_2/1DPhonic crystal and W-VO_2/1D Photonic crystal as well as carbon dots with Dielectric Bragg reflectors and metallic cavity are characterized with high temperature reflectance spectroscopy and Micro Photoluminescence spectroscopy which are discussed briefly in this chapter.

2.12 References

[1] Pandey J P, Transfer matrix method for one-dimensional photonic crystals, *J. of Ramanujan Society of Math. and Math. Sc*, **2017**, 6,121-130.

[2] John S, Toader O, Busch K, Photonic Bandgap Materials, *Encyclopedia of Physical Science and Technology*, *Academic Press*, **2003**, 133-145.

[3] Pendry J. B, Calculating photonic band structure, *J. Phys. Cond. Mat*., **1996**, 8, 10851108.

[4] Taflove A, Computational electrodynamics, *The Finite-Difference Time - Domain Method*, Artech House, Boston, London, **1995**.

[5] Pendry J B and MacKinnon A, Calculation of photon dispersion relations, *Phys. Rev. Lett*. **1992**, 69, 27722775.

[6] Knight J C, Birks T A, Russell P J and Rarity J G, Bragg scattering from an obliquely illuminated photonic crystal fiber, *Appl. Opt.* , **1998**, 37, 449-452.

[7] Li Z Y, Lin L L, and Zhang Z Q , Spontaneous Emission from Photonic Crystals: Full Vectorial Calculations, *Phys. Rev. Lett.*, **2000**, 84, 43414344.

[8] Hardhienata H, Aziz A I, Rahmawati D, Alatas H, Transmission Characteristics of a 1D Photonic Crystal Sandwiched by Two Graphene Layers, *11th International Symposium on Modern Optics and Its Applications*, **2018**, 1057, 012003.

[9] Hoekstra H J W M , *Optical and Quantum Electron*. **1997**, 29, 157-171.

[10] Bra¨uer G, Szyszka B, Vergo¨hl M, Bandorf M, Magnetron sputtering – Milestones of 30 years, *Vacuum*, **2010**, 84, 1354–1359.

[11] Xiang Y U, Chengbiao W, Yang L, Deyang Y U, Tingyan X, Recent Developments in Magnetron Sputtering, Plasma Science & Technology, **2006**, 8, 3.

[12] Kelly P J, Arnell R D, Magnetron sputtering: a review of recent developments and applications, , Vacuum, **2010**, 56 159 172.

[13] https://physics.mff.cuni.cz/kfpp/povrchy/method/magsputt-principles.

[14] Valligatla S, Chiasera A, Varas S, Bazzanella N, Rao D N, Righini G C, Ferrari M, High quality factor 1-D Er3+-activated dielectric microcavity fabricated by RF-sputtering, *Optics Express* **2012,** 20, 21214-21222.

[15] Lundin D, Minea T and Gudmundsson J T, High power impulse magnetron Sputtering: Fundamentals, Technologies, Challenges and Applications, Elsevier Science Ltd, **2019**.

[16] https://www.tn.ifn.cnr.it/facilities/rf-sputtering-facility/rf-sputtering-principles.

[17] High Reflectivity YDH/SiO2 Distributed Bragg Reflector for UV-C Wavelength Regime *IEEE Photonics Journal*, **2018**,10, 2.

[18] Duc T, Liu S, Zeng X, Lic C, Long Y, High-power impulse magnetron sputtering deposition of high crystallinity vanadium dioxide for thermochromic smart windows applications, *Ceramics International*.

[19] https://byjus.com/chemistry/principle-of-uv-visible-spectroscopy/

[20] The Beer-Lambert Law, *J. Chem. Educ.* **1962**, 39, 7, 333.

[21 Grinter H C and Threlfall T L, UV-VIS Spectroscopy and Its Applications, Springer.

[22] Challa S. S. R. Kumar, UV-VIS and Photoluminescence Spectroscopy for Nanomaterials Characterization.

[23] https://jascoinc.com/learning-center/theory/spectroscopy/uv-vis-spectroscopy/diffuse-reflectance/

[24] Zhang R, Fu Q S, Yin C Y *et al.* Understanding of metal-insulator transition in VO_2 based on experimental and theoretical investigations of magnetic features. *Sci Rep* **2018**, 8**,** 17093.

[25] Amelinckx S, van Dyck D, van Landuyt J, van Tendeloo G, Electron microscopy: principles and fundamentals. VHC, Weinheim, 1997.

[26] Pennycook S J and Nellist P D, Scanning transmission electron microscopy: Imaging an Analysis, Springer, **2011**.

[27] https://www.nanoscience.com/techniques/scanning-electron-microscopy/

[28] R. F. Egerton, Physical Principles of Electron Microscopy. New York: Springer, **2005.**

[29] Gauvin R, Review of transmission electron microscopy for the characterization of materials, 30 July **1997.**

[30] Zhao W, Xia B, Lin L, Xiao X, Liu P, Lin X, Peng H, Zhu Y, Yu R, Lei P, Wang J, Zhang L, Xu Y, Zhao M, Peng L, Li Q, Duan W, Liu Z, Fan S & Jiang K, Low-energy transmission electron diffraction and imaging of large-area graphene, , *Science advances*, **2017**, 3(9).

[31] Fultz B and Howe J, Transmission electron microscopy and diffractometery of materials, Springer, **2005**.

[32] W. Zhou and Z. Lin, Scanning Microscopy for Nanotechnology. New York: Springer, 2006.

[33] R. Guinebretire, X-ray Diffraction by Polycrystalline Materials. London: Antony Rowe Ltd, **2007.**

[34] Authier A, Lagomarsino S and Tanner B K, X-ray and neutron dynamic diffraction, Springer, **1997**.

[35] https://cms.eas.ualberta.ca/xrd/how-xrd-works/

[36] B. D. Cullity, Elements oF X-Ray Diffraction. Addison-Wesley, **1956.**

[37] Description of Crystallite Orientation in Polycrystalline Materials Having Fiber Texture, *J. Chem. Phys*, **1964**, 40, 2608.

[38] http://pd.chem.ucl.ac.uk/pdnn/peaks/broad.htm

[39] Method for Determining Crystal Grain Size by X-Ray Diffraction Cryst. Res. Technol. 2018, 1700157.

[40] Zanchet D, Hall B D and Ugarte D, Characterization of Nanophase Materials. Wiley-Vch Verlag GmbH, **2000.**

[41] http://pd.chem.ucl.ac.uk/pdnn/peaks/size.htm

[42] Mote V D, Purushotham Y and Dole B N, *Journal of Theoretical and Applied Phys*ics **2012**, 6, 6.

[43] Warren BE, Averbach BL. *J Appl Phys.* **1952** 23 497.

[44] Perkowitz, S. Optical Characterization of Semiconductors: Infrared, Raman and Photoluminescence Spectroscopy, Academic Press: London, **1993.**

[45] Weisbuch C, Vinter B, Quantum Semiconductor Structures, *Academic Press: Boston*, **2014.**

[46] Xu W, Zeng Z, Jiang J H, ChangY T, Yuan L, Discerning the Chemistry in Individual Organelles With Small-Molecule Fluorescent Probes. *Angew. Chem. Int. Ed*. **2016**, 55, 13658–13699.

[47] Haney C M, Wissner R F, Petersson E J, Multiply Labeling Proteins for Studies of Folding and Stability. *Curr. Opin. Chem. Biol*. **2015**, 28, 123–130.

[48] Fletcher KA, Fakayode SO, Lowry M, Tucker SA, Neal SL, Kimaru IW, McCarroll ME, Patonay G, Oldham PB, Rusin O, Strongin RM, Warner IM. Molecular fluorescence, phosphorescence, and chemiluminescence spectrometry. *Anal Chem*., **2006,** 78, 4047-68.

[49] Perkowitz S, Optical characterization of semiconductor. Infrared, Raman and Photoluminescence Spectroscopy, *Academic Press*, **1993**.

[50] Fries F & Reineke S , Statistical treatment of Photoluminescence Quantum Yield Measurements, , **2019**, 9 15638.

[51] Würth C, Grabolle M, Pauli J. et al. Relative and absolute determination of fluorescence quantum yields of transparent samples. *Nat Protoc*,**2013**, 8, 1535–1550.

[52] Smith E and Dent G, Modern Raman Spectroscopy: A Practical approach, *Wiley*, **2005.**

Chapter 3

1-D Photonic crystal incorporated with VO_2 nanostructures based photonic absorber for smart window applications

3.1 Introduction

Energy efficient coating designs of glasses for windows and doors are vital in energy saving buildings [1]. As we have seen in chapter 1, energy consumed by any building is nearly 40% of the total energy consumed by the entire world [2]. Exchange of heat between the inner ambience of building and the outdoor environment through these glass doors and windows are one of the major contributor to consumption of energy of a building. Therefore, regulating heat through fenestration of building windows and doors can significantly contribute to overall energy consumption [3]. For hot days, infra-red radiation entering the building should be regulated such it will minimize the usage of air-conditioning and for colder days it should maintain and limit the temperature by consuming less energy required for heating. A constructive way to achieve this is by implementing the energy efficient designs for building fenestration. Vanadium Dioxide thermochromic coating for glass windows are the potential candidate which are studied extensively for building fenestration purpose [4, 5]. Monoclinic vanadium Dioxide VO_2 (M) is a functional material which can undergo the reversible metal to insulator transition above a critical temperature (Tc) of 68 °C along with infra-red modulation of solar irradiation [6, 7]. VO_2 thin films has been widely studied for functional coatings in smart glass industry. The transition from semiconducting to metallic phase is followed by the crystallographic phase change from Monoclinic M phase to rutile R phase [8]. Due to this phase change there is drastic change in optical and electrical performance of Vanadium Dioxide. As already discussed in chapter 1, the MIT transition leads to abrupt change from IR transparent semiconducting M state to infrared (IR) blocking metallic R

state with corresponding change in their band diagram. This MIT transition, not only changes the optical transmission drastically but also it leads to the change in electrical resistance by few orders of magnitude [9]. This makes Vanadium Dioxide a promising candidate for infra-red memory devices [10] and has been extensively studied for smart windows coating and IR based optical absorbers [11, 12].

On the other hand, as we have seen in chapter 1, Planar 1-D Photonic crystals are simple artificial structures which can form the optical band gaps by localizing the light modes [13, 14]. These artificial structure can control the flow of light by allowing certain wavelength to pass through and blocking the rest. 1-D Photonic crystals also known as Distributed Bragg Reflectors (DBRs), consists of one dimensional periodic array of alternating materials of high and low refractive index respectively. DBRs yield very high reflectivity in the region known as stop band. DBR based Photonic crystals has various applications in increasing the emission from heterstructured LEDs [15] where it is used as back reflector. Bragg reflectors substrates can be directly used as absorptive medium [16, 17]. Apart from that, these structure play vital role in wider applications of thermos-photovoltaics and IR photodetectors for energy conservation [18 - 21]. DBR has widespread applications in Bio-Sensing devices [22, 23], in chemical sensors [24, 25] and IR imaging Devices [26]. 1D Photonic crystal hybrid structures are intensively studied in order to achieve near to perfect absorption by forming localized photonic modes.

There are reports on enhancement of visible transmittance of VO_2 thin film using anti reflecting coatings [27]. But modulating the IR solar radiation using DBR would be a novel approach to achieve the near to perfect absorption by tuning the band gap of the photonic crystal in IR region. This research topic has grabbed many attentions due to its practicality and feasibly of these designs at industrial level. Although there are reports of theoretical predication of absorption enhancement using this type VO_2 with 1D Photonic crystal nanocomposite structure [28, 29]. Here we have experimentally checked the performance of 1D photonic crystal based DBR, fabricated with SiO_2/TiO_2 alternating layers hybridized with VO_2 (M) nanocomposite thin films. We have observed a significant reduction in optical transmission and reflection in the IR region.

3.2 Materials and Methods for synthesis

3.2.1 Chemicals and material Used

All chemicals are used as purchased without any further purification. Ammonium meta-vanadate (NH_4VO_3, 99%, Sigma – Aldrich), ethylene glycol ($C_2H_6O_2$, 99.8%, Sigma-Aldrich), Polyvinylpyrrolidone (PVP, Sigma Aldrich), Ethanol, Silicon dioxide (SiO_2) and titanium dioxide (TiO_2) sputtering targets of two-inch diameter, double side polished glass slides.

3.2.2 Synthesis Procedure of VO_2(M)

Ammonium metavanadate (NH_4VO_3) and ethylene glycol ($C_2H_6O_2$) were used as vanadium precursors. In a typical synthesis, 1g of NH_4VO_3 was mixed with 50 ml of ethylene glycol in a 100 ml round bottom flask and this reaction mixture was placed at 160°C in an oil bath for around 2 hours under constant stirring. After vigorous stirring for 2hrs, yields a purple color precipitate. The precipitate is an amorphous vanadyl ethylene glycol complex (VEG). This complex was cooled to room temperature before washing. After the complex is cooled completely, it was centrifuged three to four times with copious amount of ethylene glycol and finally it is centrifuged with ethanol to remove residuals from the complex precipitate. This washed purple precipitate was dried for 4 hours at 60 °C and finally it is heated in a vacuum oven in the ambient atmosphere at 190°C for 30 minutes. The purple complex upon heating turned into a black powder of VO_2 (M), which is crystalline in nature as shown in the characterization below. This crystalline VO_2 (M) powder was further annealed at 650 °C for 2 hours with a ramp rate of 5 °C/minute in an Argon air flow in a tube furnace. As VO_2 (M) is very sensitive to the temperature and prone to oxidation very quickly. Therefore, before heating, tube furnace was purged with argon gas for 30 minutes to remove the excess oxygen from the chamber to avoid oxidation of VO_2 powder. After tube furnace was cooled to room temperature completely only then Argon flow was stopped to prevent the sample oxidation. The annealed VO_2 (M) powder was retained with dark blue grayish color, which leads to the formation of VO_2 (M) powder with higher crystallinity.

3.2.3 Fabrication and characterization of Distributed Bragg Reflectors

To fabricate Distributed Bragg Reflector, Si wafers and glass substrates are used. Before fabricating DBR, both substrates are subsequently cleaned with DI water, Acetone and ethanol for 10 min each in ultrasonic bath and dried in vacuum oven for an hour properly before the use. RF Magnetron sputtering as discussed in chapter 2 are used to fabricate the DBR's. To fabricate the DBR's, alternate layers of Silicon Dioxide (SiO_2) and Titanium Dioxide (TiO_2) are deposited over the glass substrate in argon ambient. The thickness of each layer is calibrated with RF Power and time manually. Quartz meter is used to control the deposition rate. To fabricate the DBR, glass slides of size 0.5 × 0.5 cm^2 are used. Before the deposition of layers, the base pressure of the sputtering is kept at ~ 1×10^{-7} mbar. Whereas while depositing the layers of SiO_2 and TiO_2 the active pressure is measured ~ 9.2×10^{-3} mbar. After depositing SiO_2 and TiO_2 layers by keeping RF power and time fix, the thickness of layers is measured with profilomter (Vecco, Dektak 150). The DBR structure fabricated is a quarter wave stack, with thickness of SiO_2 and TiO_2 layers are calculated with equation $d = \lambda/4n$, where λ is the wavelength where Bragg reflector stop band has to be tuned with 'n' is the refractive index of the respective layers. To tune the Bragg reflector with stop band wavelength at λ_o = 1350 nm, the thickness of corresponding SiO_2 and TiO_2 layers are calculated and experimentally calibrated around t_{SiO2} ~ 230 nm and t_{TiO2}~ 130 nm respectively. This DBR is fabricated with four stacks of alternate layers and measured reflectivity is found to be ~ 60% according to equation 2.2 in chapter 2. The other DBR which is used in experiments is tuned at stop wavelength λ_o ~ 1600 nm, with respective thickness of t_{SiO2} ~ 275 nm and t_{TiO2} ~ 150 nm respectively. Before fabricating the DBR's, their reflectivity is simulated using Transfer matrix method calculation in MATLAB. The simulated and experimental reflectivity data of DBR's for a certain number of layers are in good match with each other. Therefore, this shows the reliability of fabricated DBR's with the RF deposition system with calibrated parameters. Apart from that AFM surface measurement of Fabricated DBR's gives the good results of surface smoothness. As shown in Figure 3.1, the surface roughness was found to be around ± 2 nm. Therefore, we are able to fabricate very high quality tunable Distributed Bragg Reflectors with dielectric materials using RF magnetron Sputtering system.

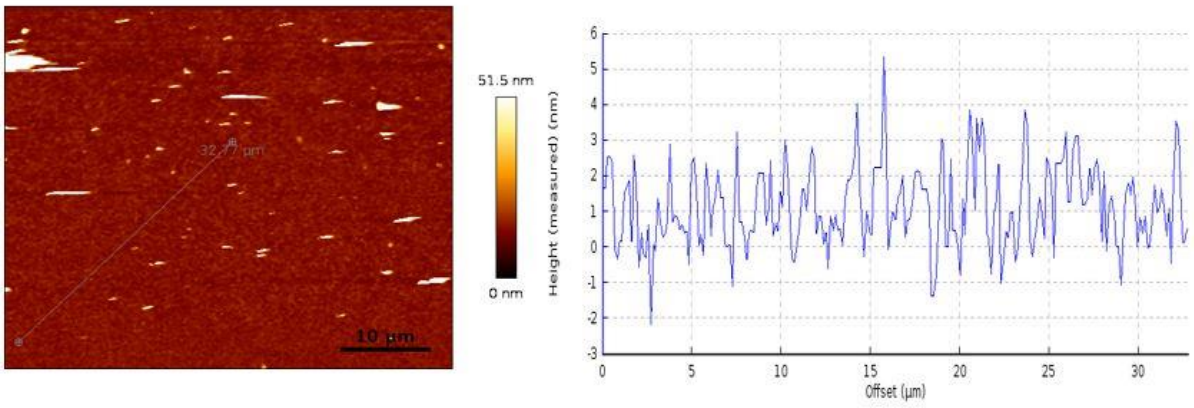

Figure 3.1 Showing the AFM image of SiO2/TiO2 Bragg reflector fabricated over glass substrate with surface roughness of ± 2 nm.

3.3 Characterization of VO_2 nanoparticles

3.3.1 structural and morphological analysis of VO_2 nanoparticles

Upon the reaction of ammonium methavanadate (NH_4VO_3) powder and ethylene glycol ($C_2H_6O_2$) under heat treatment Vanadium from V^{5+} oxidation state reduced to V^{4+} oxidation state and a purple colored vanadyl complex has formed followed by the release of N_2 [30]. As reported in literature [31] FTIR spectrum having sharp absorption peaks around 550 cm^{-1} and 1062 cm^{-1} respectively. Which represents V– O and V=O bonds corresponds to edge-sharing vibrations, the other peak around 880 cm^{-1} corresponds to the vibration due to bending. O–H and H–O–H of H_2O molecule belongs to the peak at 1631cm^{-1} and 3437 cm^{-1} which is due to bending and stretching of the molecule respectively. Apart from them, peak around 1379 cm^{-1} corresponds to the vibrations due to bending of $-CH_2$ of unreacted organic molecule. There is no trace of C=O, C=C and $-CH_3$ peaks in the FTIR spectrum. Therefore, the structure of the vanadyl complex from above analysis is predicted as shown in Figure below,

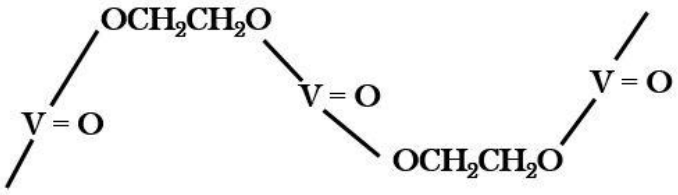

In the above structure, ethylene glycol plays the role of the cross-linking reagent which attaches to the central metallic ion and forms a linear chain. To further characterize the Vanadyl complex X-ray diffraction is employed and data is shown in Figure 3.2. The XRD peaks of Vanadyl complex are in good match with the peaks shown in JCPDS no. 49-2497.

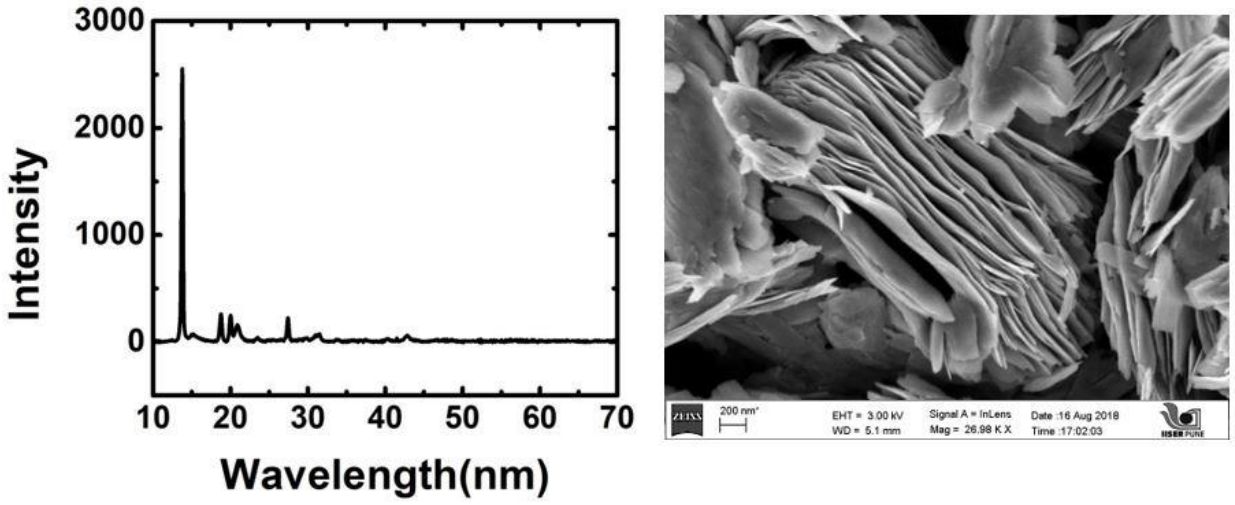

Figure 3.2 (a) Showing the XRD diffraction peaks associated with Vanadyl complex and (b) showing the FESEM image of planar sheet like morphology of vanadyl complex.

The main peak around $2\Theta = 13.46^{o}$ is associated to the Vanadyl complex given as $VO(OCH_2CH_2O)$, the following reaction equation to obtain this complex is as follow,

$$NH_4VO_3 + C_2H_6O_2 \rightarrow N_2 + VO(OCH_2CH_2O)$$

The FESEM images of vanadyl complex has a planar sheet – like morphology as shown in Figure 3.2 (b), with average length of each sheet in the order of few micrometers. As reported, pyrolysis of Vanadyl complex in inert environment leads to the formation of V_2O_3 phase. To obtain VO_2(M) pure phase the above complex should undergo pyrolysis in air environment. the pyrolysis reaction in air as follows,

$$VO(OCH_2CH_2O) + O_2 \rightarrow VO_2 + H_2O + CO_2$$

While pyrolsis of complex to obtain VO_2(M), ambient enviroment , time of pyrolysis and tempertuare are the most important factors. From the FESEM image of Vanadyl complex it is

assumed that the complexs are acting as the seeds for the vanadium dioxide morphology. From Figure 3.3 (a) depicting the XRD diffraction patteren of Pure Phase VO_2(M). The $VO(OCH_2CH_2O)$ complex diffracton peak disappear completely after 30 min of pyrolysis in air atmosphere and a black coloured VO_2(M) powder is obtained. There is no peak associated complex appear in Vanadium Dioixde XRD pattern. The further pyrolysis of complex trun the pure phase VO_2(M) into V_2O_5. Formation of yellow coloured V_2O_5 indiacte the oxidation of the VO_2(M). therefore, the appropiate time to yeild Pure Phase VO_2(M) is 30 min for 190 °C in air atmosphere. Figure 3.3 (a) showing the XRD patteren of VO_2(M) corresponds to JCPDS: 82 – 0661.

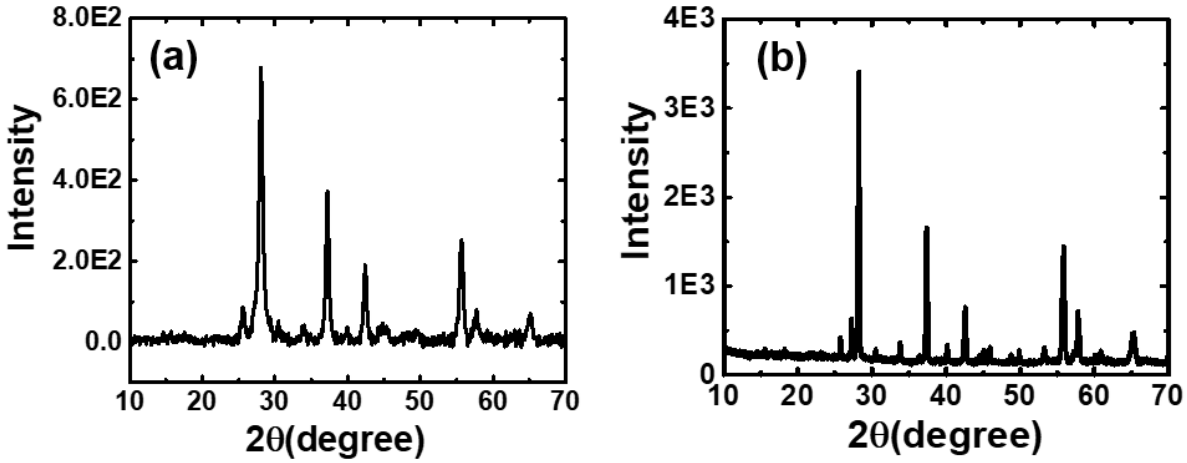

Figure 3.3 (a) XRD pattern of Moderately crystalline VO_2 formed by annealing at 190ºC in ambient atmosphere and (b) XRD pattern of Highly crystalline VO_2 formed by annealing Moderately crystalline VO_2 at 650ºC in argon atmosphere.

Figure 3.3 (b) showing the XRD diffraction pattern of VO_2(M) nanoparticle post annealed at 650°C, resulting powder also showing the peaks associated at VO_2(M) but with increased intensity by orders of magnitude. Therefore, post annealing of moderately crystalline VO_2(M) at high temperature under inert environment results in the formation of Highly crystalline VO_2(M) nanoparticles distributed uniformly as shown in EDS data in Figure 3.4. EDS peaks clearly indicates the atomic ratio of vanadium and oxygen throughout the sample which is found to be nearly 40 % for Vanadium and nearly 60% for oxygen. No other elemental impurity is detected in the EDS data which confirm the purity of VO_2(M) phase.

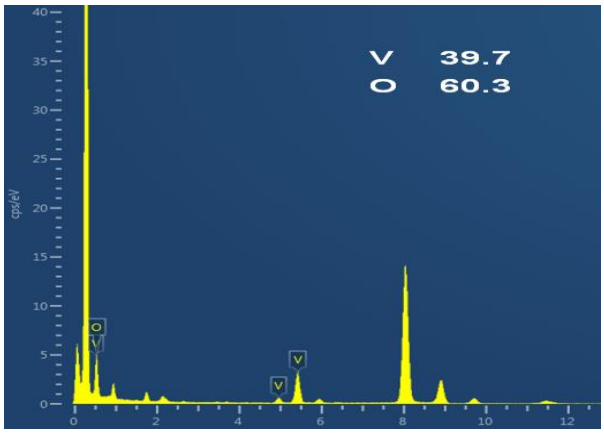

Figure 3.4 Showing the EDS of VO_2 confirming the atomic ratio of vanadium and oxygen.

Moderately crystalline and highly crystalline VO_2 (M) nanostructures images with Transmission electron spectroscopy (TEM) and Field emission-scanning electron microscopy are shown in Figure 3.5 along with vanadyl complex morphology, both theses spectroscopies gives lot of information about the formation mechanism of VO_2 (M) nanostructures.

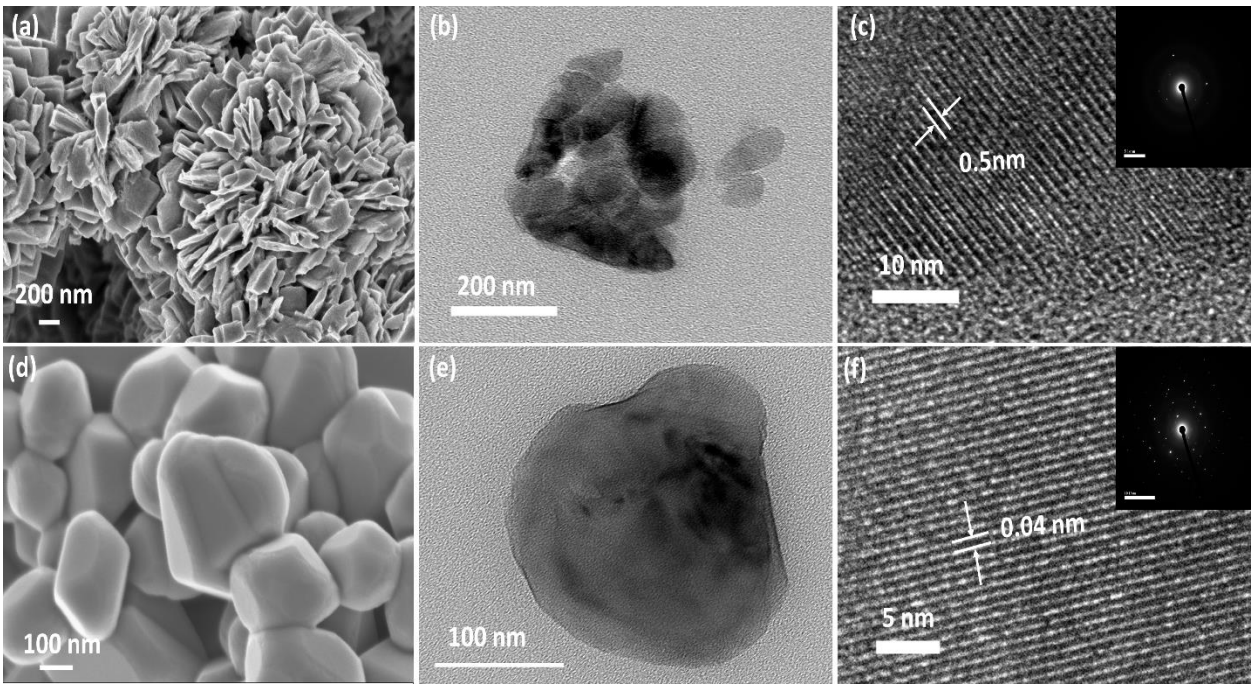

Figure 3.5 (a) and (d) showing the FESEM images of Moderately crystalline (MC) and Highly crystalline (HC) VO_2 nanoparticles. (b) and (e) showing the TEM images of cluster of MC VO_2 nanostructures and regular shaped polyhedrons of HC VO_2 with (c) and (f) showing the HRTEM images of MC and HC VO_2 nanostructures along with inset showing the SAED pattern.

As shown in Figure 3.5, the morphology and crystallinity of as-prepared Moderately crystalline and highly crystalline VO_2 nanostructures are estimated by FESEM and High - Resolution TEM images. Figure 3.5 (a) Showing the Moderately crystalline VO_2 nanostructures having rod like morphologies with vanadyl complex act as seed for VO_2 (M) Nano rods. The Nano rods are aggregated together due to large surface energy, therefore an aggregated pile of rods obtained from this synthesis method. The Transmission electron spectroscopy as shown in Figure 3.5 (b) also confirms the formation of the Nano rods with size of the rods varying from 100 to 200 nm accumulated into a cluster. Figure 3.5 (c) showing the High resolution TEM images and it gives the information about the crystalline phase of VO_2 (M) nanostructures. From HR-TEM images the calculated inter-planar distance of moderately crystalline VO_2 (M) nanostructure are found to be around 3.4 A^o and this inter-planar distance is associated with (011) miller plane of the MC VO_2 (M) with JCPDS: 82 – 0661. Highly crystalline VO_2 (M) as already discussed in Figure 3.4 (b) XRD diffraction, is synthesized by post – annealing of the as – synthesized MC VO_2 by annealing at 650^{o}C in argon ambient. As shown in FESEM image of Figure 3.5 Highly Crystalline VO_2 (M) nanoparticles are uniformly distributed and have regular and clear grain boundaries. It is evident from the above analysis that with increase in temperature the particles which are aggregated into the cluster, transformed into more regular shaped particles. As reported in literature [32] when the particles are annealed at temperature more than 500^{o}C, it will lead to formation of uniformly distributed particles. The particle size is also consistent with the Debye-Scherer calculation from the XRD diffraction pattern. The particles annealed at the relatively low temperature, obtain small crystalline size particles having large surface energy which causes them to accumulate together. Upon increasing the annealing temperature, the surface energy of the large crystalline size decreases and therefore, it reduces the accumulation of the particles. And if the particle size is more than 500 nm, it will lead to less accumulation of particles together. As shown in Figure 3.5 (d) FESEM images of highly crystalline VO_2 nanoparticles have polyhedron morphology. This Morphology is also confirmed by the TEM image in Figure 3.5 (e) and Figure 3.5 (f) gives the HR-TEM image of Highly crystalline VO_2 nanostructure with calculated inter-planar spacing of 2.42 A^o, with inter-planar spacing associated with (200) miller plane.

Figure 3.4 (a) and 3.4 (b) shows the XRD of MC and HC VO_2 (M) nanoparticles. It is quite evident from the above results that after thermolysis, the peak corresponds to the Vanadyl complex vanishes completely and peaks corresponds to the monoclinic VO_2 starts to appear with the orientation along the (011) miller plane with main peak around $2\Theta = 27.95^{o}$. Also the FWHM (Full width half maximum) of Highly crystalline VO_2 (M) nanoparticles synthesized at higher temperature decreases as compared to the MC VO_2 (M) nanoparticles. Also the peak intensity of HC VO_2 (M) also enhances significantly as compared to MC VO_2 (M). The another important characterization which determines the structural phase transition is High temperature *in situ* XRD to determine the transition from the monoclinic phase of VO_2 (M) to the VO_2 rutile phase around the transition temperature. Figure 3.6 shows the high temperature XRD of Moderately crystalline VO_2 nanostructure.

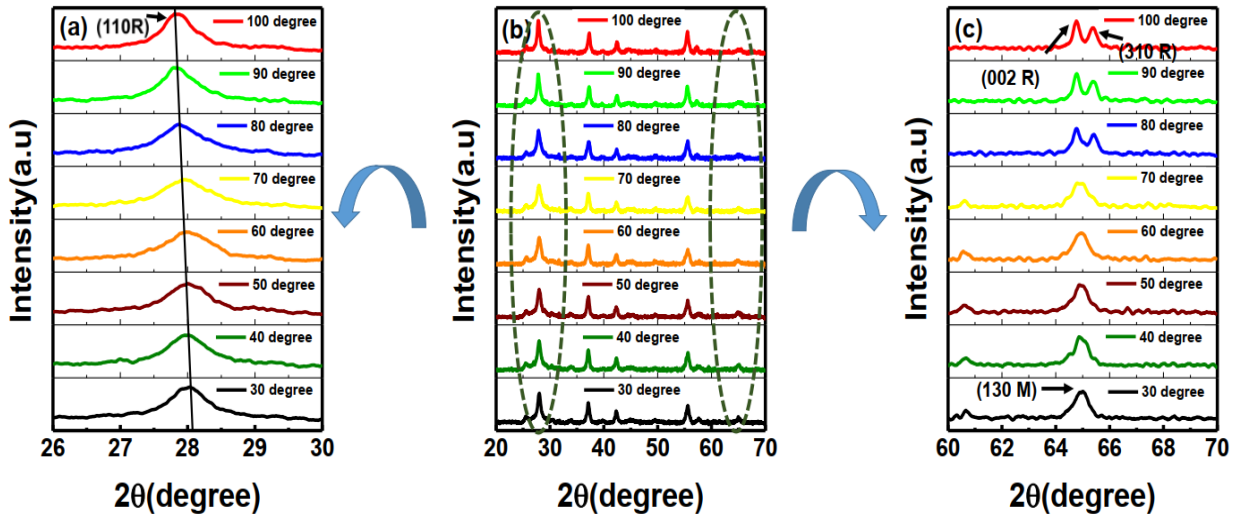

Figure 3.6 Showing the high temperature XRD of Moderately crystalline VO_2 nanostructures with (a) showing with increase in temperature the highest peak intensity shifting in the range of 26 - 30º towards the lower angle 2Θ along with (b) showing the XRD diffraction with various temperature range and transition temperature (MIT) from VO_2(M) to VO_2(R) around the critical temperature of 68ºC and (c) showing the another signature of this transition with gradual splitting of single peak at 65º into two peaks in the range of 62-68º. Along with plane associated with single peak is (130) monoclinic plane and the two plane associated with doubly peaks are (002) and (310) rutile plane.

The temperature dependent in situ XRD of moderately crystalline VO_2 (M) nanostructures is shown in Figure 3.6 is clearly indicting all the structural changes occurring in Vanadium Dioxide lattice upon applying heat to the nanostructures. With transition taking place from monoclinic VO_2

(M) phase to rutile VO_2 (R) phase The transition temperature is observed to be around 360 K. Previous [33] and our report shows that, the XRD pattern of VO_2 remains into monoclinic phase below the transition temperature of 360 K, with XRD diffraction peaks are in good match with JCPDS – 82 – 0661 which confirms the VO_2 monoclinic phase. Above the transition temperature of 360 K, the XRD diffraction peaks are in good match with JCPDS – 79 – 1655 which is associated with high temperature rutile phase of VO_2 nanostructures. The major XRD signature corresponds to the structural changes, is the shifting of the highest intensity XRD diffraction peak in the range of $26^0 \leq 2\Theta \leq 29^0$ as indicated in the above figure. With, the monoclinic structure transforming into rutile phase the lattice plane corresponds to (011) VO_2 (M) phase transform into (110) VO_2 (R) plane. Second major indication of structural lattice change that can be observed is in the range $64^o \leq 2\Theta \leq 66^o$. In this range the low temperature monoclinic peak of VO_2 (M) associated with plane (310) split into two peaks which corresponds to VO_2 (R) (130) and VO_2 (R) (002) plane. Therefore, temperature dependent XRD gives the evident results of structural phase transition occurring in VO_2 nanostructure due to change in unit cell dimensions while transforming from monoclinic VO_2 (M) to rutile VO_2 (R) Phase.

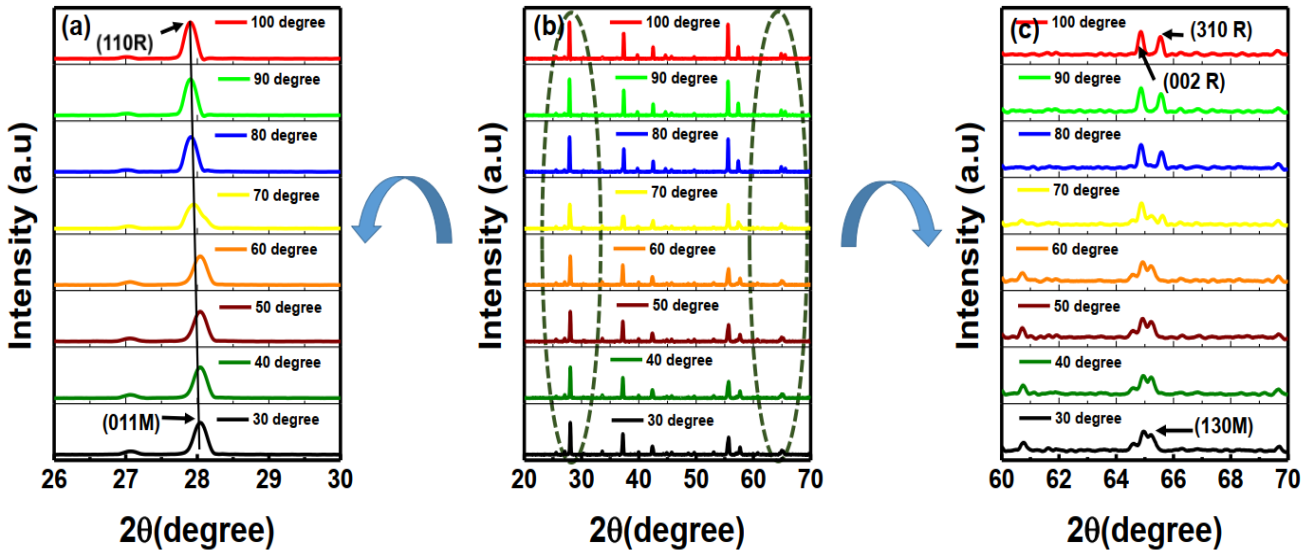

Figure 3.7 Showing the High temperature in situ XRD diffraction pattern of Highly crystalline VO_2 nanostructures. (a) Indicating the shift in highest intensity peak with change of lattice planes from (011) monoclinic plane to (100) rutile plane of VO_2. (b) showing the XRD diffraction peaks of HC VO_2 with transition occurring near temperature of 360K and (c) showing the gradual splitting of two rutile planes (310) R and (002) R from the monoclinic plane of (130) M.

Similar temperature dependent in situ XRD is carried out for Highly crystalline VO_2 nanostructures. And structural changes in the HC VO_2 lattice upon applied temperature are observed. The peak with highest intensity, shift in the range of $26^{o} \leq 2\Theta \leq 29^{o}$ as shown in the figure 3.7 (a). The visibility of two sharp peaks in the region of $64^{o} \leq 2\Theta \leq 66^{o}$ are clear evidences of structural phase transition from monoclinic to rutile phase above the phase transition. Therefore, these results establish the phase transformation from monoclinic to rutile above 340 K. Form structural point of view, below the phase transition temperature the vanadium atoms remain in Zig - Zag kind of orientation which corresponds to the insulting behavior of the VO_2 (M) and above 340 K there is a shift in linear vanadium atoms chain which transforms the lattice into VO_2 (R) phase. Therefore, above characterizations are quite sufficient to confirm the VO_2 (M) phase transformation.

3.3.2 Fabrication of VO_2 – PVP composite thin films

To fabricate VO_2 thin films over the glass or other substrates, the uniform deposition of VO_2 nanoparticles is a challenge. VO_2 nanoparticles being highly non dispersive and in soluble in nature. There are quite few solvents which can be dispersive for VO_2 nanoparticles. A polymer matrix to embed VO_2 nanoparticles is most suitable route to fabricate large area coating. As Vanadium Dioxide can undergo into many oxidation states and V_2O_5 being the most suitable oxidation state therefore it is very important to find the suitable host for VO_2 nanostructures without tempering it's thermochromic properties. Polyvinyl Pyrrolidone (PVP) being most compatible polymer agent for VO_2 nanostructures to form a composite to fabricate thin films as it provides an effective insulation against the oxidation. We have used PVP with average molecular weight of 10,000. And the VO_2 and PVP ratio is kept around 1:10 parts with 1 ml of ethanol and whole composite solution heated at 60 ^{o}C for at least 12 hrs. to form a uniform slurry. The composite solution should not be heated at higher temperature than 60^{o}C. VO_2 powder is thoroughly gridded with clean motor pestle before the mixing VO_2 into PVP as it prevents the aggregation of VO_2 particles, After the slurry is formed it is uniformly casted on a glass slide with spin coating. VO2 thin films are spin coated over glass substrates of size 0.5 × 0.5 cm2 and 60 µl of VO2/PVP composite is taken in all cases. To vary the thickness of the film, the spin coater speed is adjusted. To fabricate the thin film of thickness around 110 ± 10 nm we have used spin

coating with rpms of 4000 for 40 second to deposit over Distributed Bragg reflector. The FESEM image of VO_2 thin film over glass is shown in figure below 3.8.

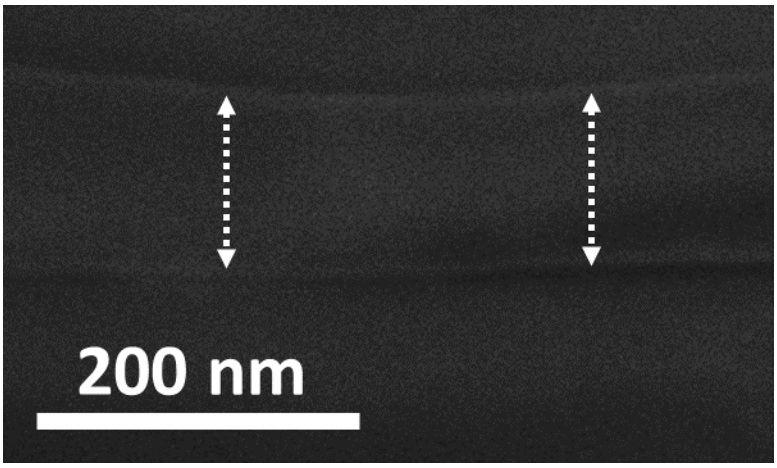

Figure 3.8 Showing the FESEM images of VO_2 thin film over glass with estimated thickness of 110 ± 10 nm.

3.3.3 The optical characterization of VO_2 – PVP thin films

The main parameter which determines the performance of VO_2 thin film is transmission modulation i.e., change in optical transmission of VO_2 thin film with increase in temperature. Figure 3.9 (a) and (b) showing the optical transmission of moderately crystalline and highly crystalline VO_2/PVP composite thin films in response to the external temperature. In our report we have observed, both moderately crystalline and highly crystalline VO_2/PVP nanocomposite thin films have similar transmission reduction with temperature enhancement. Thin films were fabricated by depositing equal amount of VO_2 material over all substrates to fabricate thin films. From the figure 3.9, it is quite evident that the change in transmission is more profound when temperature reaches to and above 360 K. Thin film fabricated with moderately crystalline VO_2 nanostructure composite as estimated thickness around 110 ± 10 nm as shown in Figure 3.8. From figure 3.9 (a) as the temperature increases from 300 K to 380 K, the optical transmission reduces from 67 % to 53 % at the wavelength of 1300 nm and from 73 % to 55 % at wavelength of 1600 nm respectively. Therefore, the optical modulation i.e. ΔT is nearly 14 % at wavelength 1300 nm is calculated and nearly 10 % at wavelength of 1600 nm for highly crystalline VO_2 thin films which similar to that of the moderately crystalline VO_2 thin films when temperature increase from 300 K

to 380 K. This variation in transmission modulation is due to the change in structural phase change from semiconducting monoclinic to metallic rutile structure of VO_2/PVP thin films. Similar change in transmission has been reported [34] which shows ~ 10 % change in VO_2 thin films at the wavelength of 1300 nm as the temperature increases.

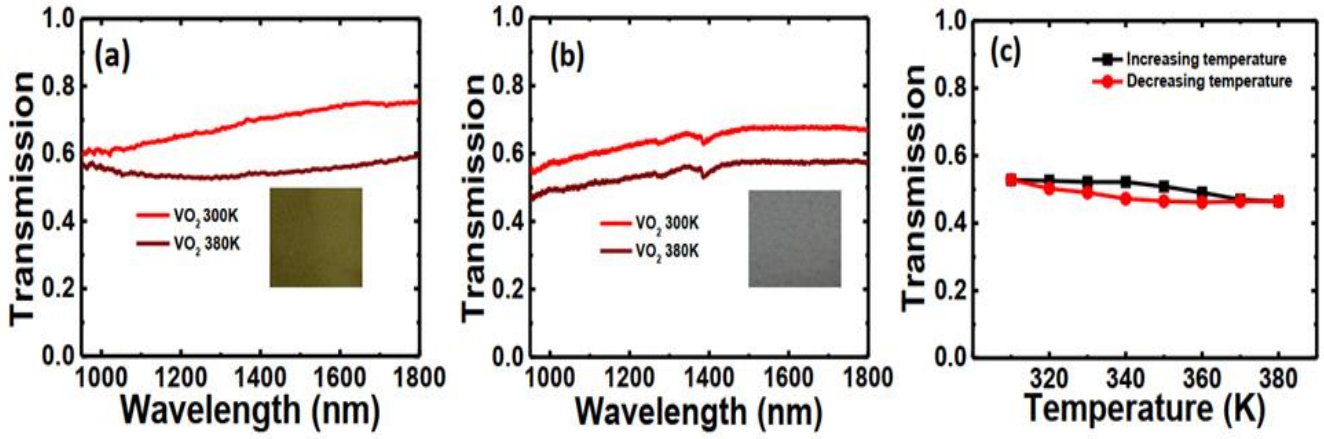

Figure 3.9 (a) showing the transmission spectra of moderately crystalline VO_2/PVP thin films fabricated over glass with temperature increasing from 300K to 380K along with transmission change of nearly 14%. (b) showing the optical transmission of highly crystalline VO_2/PVP thin films having transmission change of nearly 10 % which is similar to moderately crystalline VO_2 thin films with increases in temperature from 300 K to 380 K and (c) showing the reversible transmission hysteresis of Moderately crystalline VO_2 thin films and the hysteresis width of 0.05 at transition temperature of 340 K. (Insets showing the thin films optical image of MC and HC VO_2 thin films)

Figure 3.9 (c) showing the reversible transmission hysteresis of moderately crystalline VO_2/PVP thin films in response to thermal energy. The thin films were fabricated over glass and the hysteresis is measured at the wavelength of 1600 nm. The width of the transmission hysteresis upon reversible measurement is calculated to be around 0.05 at the transition temperature of 340 K. Our reported transmission hysteresis width is quite narrow, which is associated with thin film fabricated with uniformly distributed particles and with good crystallinity having small granular size particle of Moderately crystalline VO_2 nanostructures [35, 36]. In general, the exact cause of hysteresis is widely unknown. Research work done so far suggests, crystallite grain size and stress are the major causes of hysteresis width. Stress can occur due to two reasons, one is external which occur due to thermal expansion mismatch of VO_2 thin film and substrate and other one is internal which mainly occur due to voids, grain and boundaries etc. of VO_2 nanostructures itself. From

our observation both moderately crystalline and Highly crystalline VO_2 nanostructure thin films have similar optical performance in terms of optical modulation around the phase transition temperature, therefore for further measurement and studies, we have employed moderately crystalline VO_2 / PVP composite due to ease to synthesis method in the air ambient environment. Figure 3.10 demonstrating the effect of VO_2 thickness on optical transmission performance. As observed VO_2 thickness has strong influence on transmission performance on transforming from monoclinic to rutile state in IR region. In figure 3.10 we have optimized the film thickness and by measuring its thickness with FESEM cross sectional image. The Inset of Figure 3.10 (a) showing the thickness of the films used which is around 110 ± 10 nm. The film undergo transmission modulation of around i.e. $\Delta T \sim 14$ %. Upon increasing the film thickness by reduce the spin coating speed to 3000 rpm, the film thickness of 150 ± 10 nm is formed as shown in the inset of figure 3.10 (b) exhibiting transmission modulation of around $\Delta T \sim 9$ % with increase in temperature from 300 K to 380 K respectively.

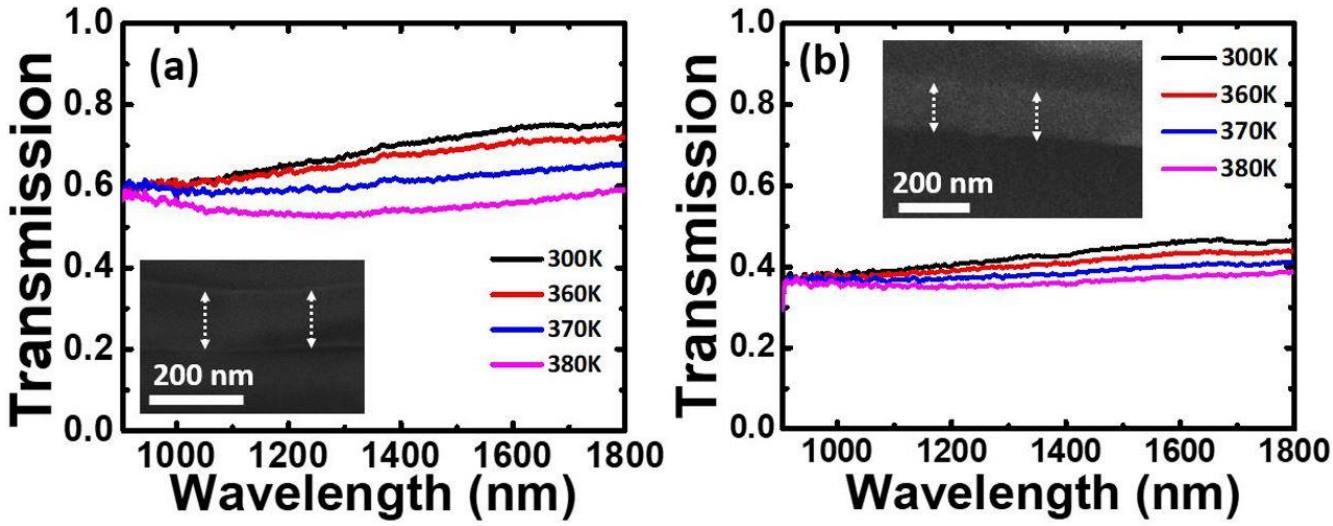

Figure 3.10 (a) Showing the transmission modulation of VO_2 thin film on glass with thickness around 110 ± 10 nm and (b) showing the transmission modulation of VO_2 thin film with thickness around 150 ± 10 nm (inset showing the FESEM cross section of the thin films.

As there can be enhanced scattering in VO_2 nanostructures in thick films which leads to decrease in transmission with increase in thickness of VO_2 thin film. Our results matches well with

the previous reported literature where the thickness of VO_2 film between 95 – 150 nm is exhibiting the reasonably good transmission switching in IR region. For further studies we have optimized the VO_2 thickness to be around 110 ± 10 nm to employ over 1D Photonic crystals tuned in Infra – red region.

3.3.4 The temperature dependent performance of VO_2/ 1D Photonic crystal

The hybrid structure of Vanadium Dioxide incorporated with 1D Photonic crystal is illustrated in Figure 3.11 below.

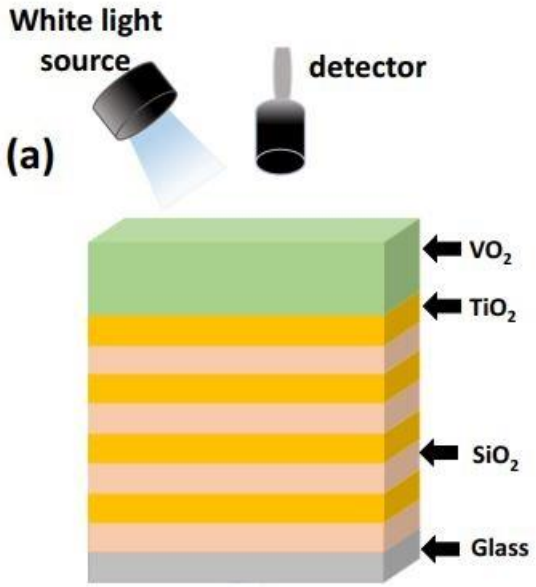

Figure 3.11 (a) showing the schematic diagram of VO_2 /1D photonic crystal structure in reflection measurement mode illuminated with white light source.

Photonic crystal structures are the key component among advanced optically engineered structures for photovoltaic applications such as absorption enhancement. The goal of the above design is twofold: first it decreases the light reflection at the top surface as it allowed particular wavelength of light to get reflected. Second, this structure provides sufficient photon path, or lifetime, within

he absorbing material. Figure 3.13 (b) shows the optical transmission of DBR which is 40 % transmitting and central wavelength of stop band tuned at $\lambda_o \sim 1350$ nm. DBR is fabricated with periodicity of four stacks of SiO_2 and TiO_2 material. As already discussed, Periodicity is the reason which leads to the formation of Photonic Stop Band which leads to ~ 0 % transmission for certain desirable wavelength of light. Since both SiO_2 and TiO_2 have high transmission in entire wavelength spectrum with very high melting point, these properties make this material a potential candidate for Photonic Crystal fabrication for smart window application. On employing the VO_2 layer over 40 % transmitting DBR, the optical transmission further reduced to 30 %. With decrease in transmission there is slight shift of ~ 60 nm of the transmission spectra towards the higher wavelength i.e. from 1350 nm to 1410 nm. The overall decrease in optical transmission is ~ 25% as compared to the optical transmission of VO_2 thin film fabricated over glass. Now as the temperature increases, the optical transmission of VO_2 further decreases ~ 20 % at temperature 380 K. The decrease happens in the broad wavelength of spectrum i.e., from 1250 – 1550 nm. Therefore, even few stacks of the distributed Bragg reflector are capable of achieving reasonably good amount of reduction in optical transmission. Hence this VO_2/DBR design can be highly effective for hybrid optical absorbers for application in thermochromic based smart glass technology.

Now, by increasing the number of periodic stack to a certain number, we can achieve ~ 100 % reflecting DBR. As we have already discussed in the introduction upon increasing the periodic stacks in the Distributed Bragg reflector can increase the reflection to 100 % efficiency or by increasing the contrast between refractive index between periodic layers, will also increase the reflection as well bandwidth of the stop band. Figure 3.12 is showing the simulated reflectivity curves with different periodic layers,

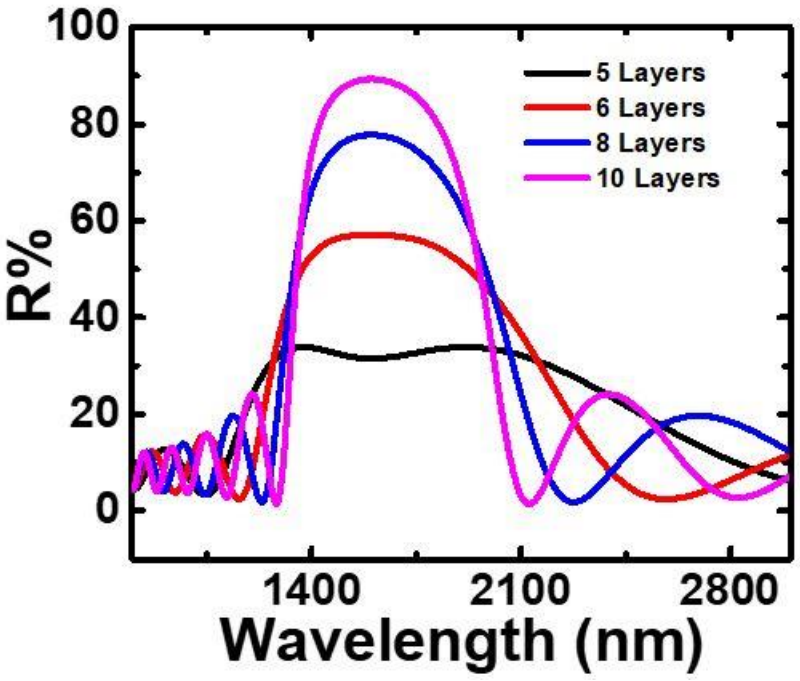

Figure 3.12 Showing the simulated result of reflection of Bragg reflector tuned at 1600 nm with varying the no. of periodic stacks.

Therefore, from figure 3.12, increasing the number. of periodic stacks for a certain refractive index contrast not only lead to increment of optical reflection but also its lead to relatively sharper stop band as the number of stacks increases. This kind of DBR's will be beneficial for optoelectronic devices to increase the mono-chromaticity of the emitted light. Thus, Bragg reflector with nearly 10 % transmission with consecutive reflection of nearly ~ 98 % is fabricated by increasing the SiO_2/TiO_2 periodic stacks from four to seven with central stop band wavelength λo ~ 1600 nm as shown in Figure 3.13 (b).

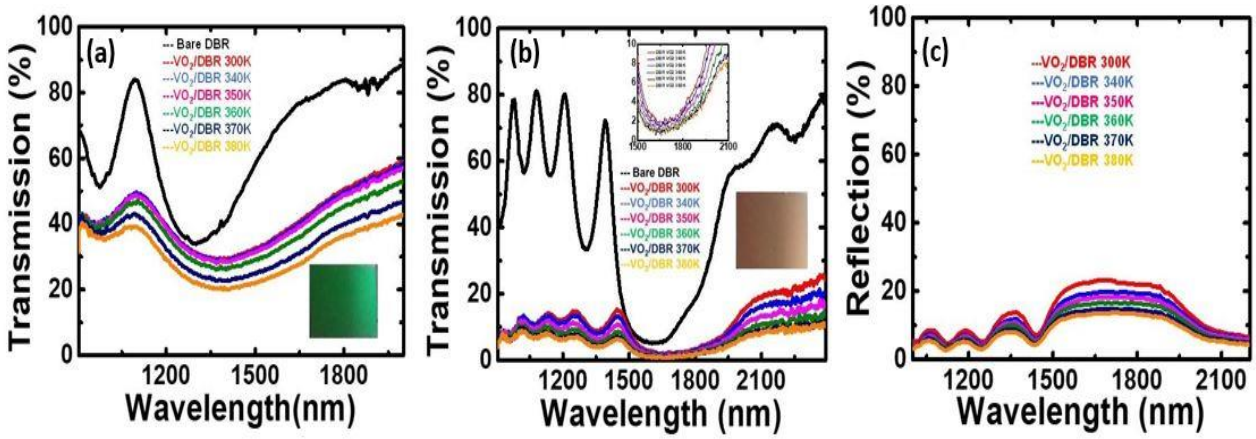

Figure 3.13 (a) showing the optical transmission of Bare DBR with 40 % transmission and central stop band wavelength λ_o around 1300 nm employed with MC VO_2 thin film. The optical transmission decreases significantly from 34 % to 20 % with increase in temperature to 380 K along with slight red shift of 60 nm. (b) showing the transmission spectra of nearly 90 % reflecting DBR with transmission near to 10 % tuned at 1580 nm. As the temperature increases from 300 K to 380 K, the transmission reduced to 0.6 % along with red shift of the spectra. The inset figure showing the transmission change in the stop band with calculated fractional change in transmission T_{380K}/ T_{300K} ~ 2 though the range of wavelength. And (c) is showing the consecutive change in reflection with increase in temperature of VO_2/DBR structure.

Figure 3.13 (b) VO_2/DBR structure, when the temperature increases to 380 K, the optical transmission reduces to 0.6 % and the stop band wavelength red shift to 1668 nm. Therefore, by increasing few stacks can lead to complete reduction of optical transmission with nearly 100 % reflection, 1-D photonic crystal based VO_2 thin films can achieve effectively near to unit absorption at the tuned wavelength. Therefore, it is quite evident that number of periodic stack plays crucial role in absorption enhancement. In Figure 3.13 the reduction in optical transmission in the Bragg reflector stop band is not clearly visible. But the fractional transmission change which is ~ T_{380K} / T_{300K} nearly ~ 2 in the entire wavelength region. The figure in inset clearly showing the reduction in transmission with increase of temperature above 340 K. The consecutive reflection spectra of VO_2/DBR structure is shown in Figure 3.13 (c). At temperature near to room temperature i.e., 300 K the VO_2/DBR structure has ~ 30 % reflectivity. And with increase in temperature, the reflectivity of the structure further decreases to ~ 15 % correspondingly in the infra-red region. As Our measurements of transmission and reflection with increasing temperature are done on our home build set up, we have also measured these spectra with Shimadzu UV 3600

Plus integrating sphere at room temperature to keep the account of both specular and diffusive reflections and optical scattering which is an important parameter in absorption measurements.

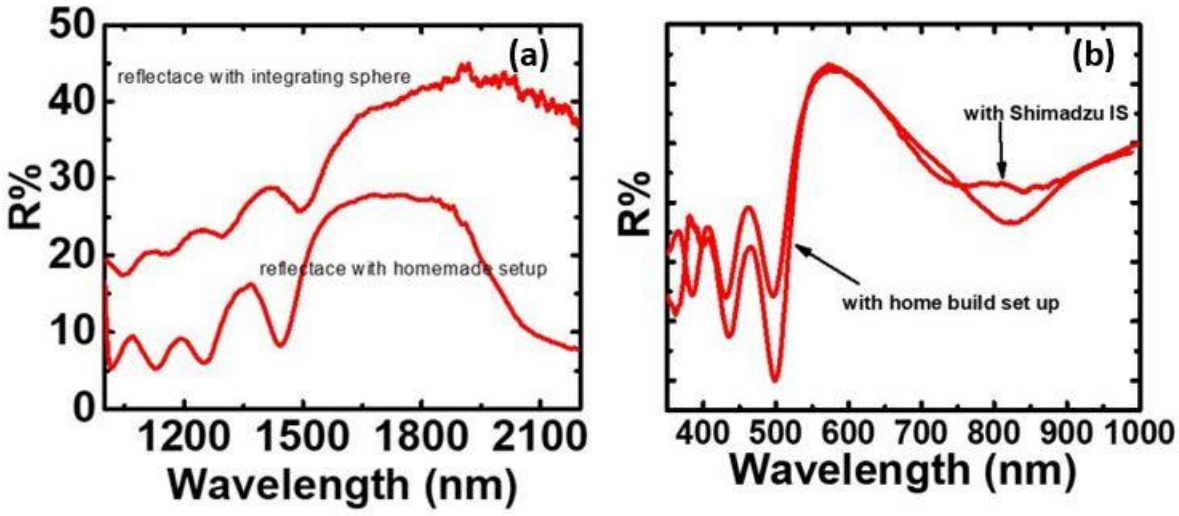

Figure 3.14 showing reflection measurement of VO_2/DBR structure with and without integrating sphere.

As shown in Figure 3.14, the specular reflectivity spectra on our home build set up have relatively sharper and more characteristic features of the DBR. Whereas, the reflectivity spectra of the same structure of VO_2/DBR have broader spectrum with suppressed DBR features. And the intensity of the integrated sphere reflectivity measurement is relatively higher in case of reflectivity spectra on our home build set up. Whereas, no such intensity difference is observed in the reflectivity spectra of the bare DBR taken from the both setups as shown in Figure 3.14 (b). therefore, this indicated that reflectivity measured with Integrating sphere of VO_2/DBR structure has the substantial influence of diffuse reflection and optical scattering. Although the theoretical calculation of reflection and transmission coefficient of VO_2/DBR structure [36] does not included any consideration about the effect of diffuse reflection and scattering parameter. Therefore, the data presented in this thesis is analyzed with specular reflectivity set up in our lab. Therefore, the above results are significant to show that there is an effective enhancement in absorption of VO_2/DBR structure assuming there are no significant scattering losses. Figure 3.15 (a) and (b) both showing the slight red shift in wavelength with angle dependent transmission and reflection. The possible reason of this shift could be the additional layer of VO_2(M) over the Bragg reflector.

Due to this addition layer the overall optical thickness of the Bragg reflector changes which can causes the shift of the optical interference reflected from the VO_2/DBR structure towards the higher wavelength [37]. The red shift in the above plots can also be explained by the Matlab simulation curve based on transfer matrix calculations [38,39]. Figure 3.15 shows that non uniformity of VO_2 thin film leads the deviation in effective refection angle of the incident light towards the lower angles from the normal, hence causes a red spectral shift in the reflectivity and transmission spectra.

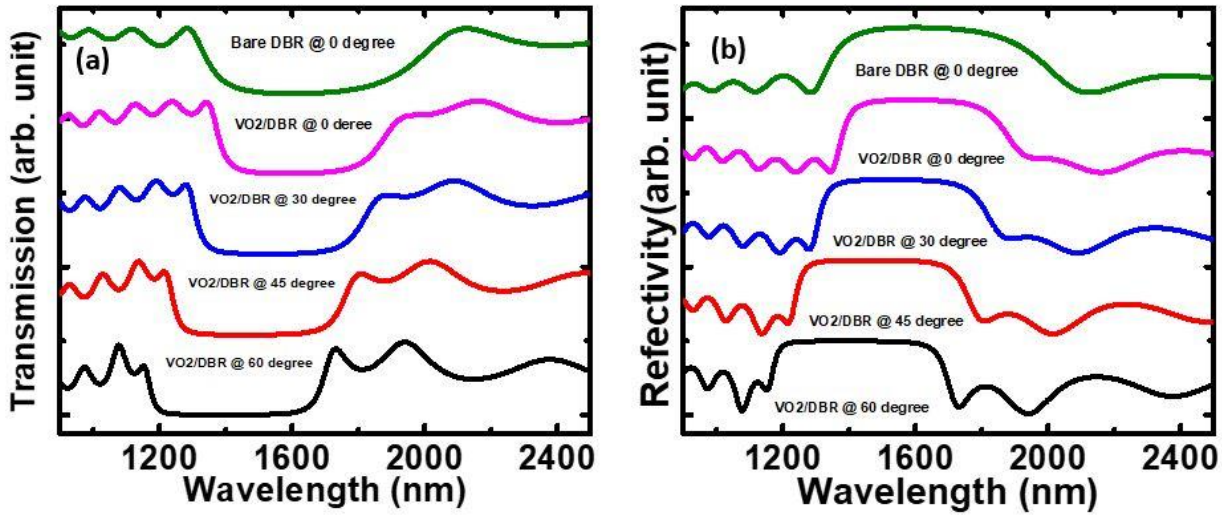

Figure 3.15 showing the transfer matrix based calculation for VO_2/DBR structure (a) angle dependence transmission and (b) angle dependence reflectivity.

The transfer matrix calculation for non-normal incident angle has shown significant red spectral shift for light refracted at lower angle of incidence. while calculating reflection and transmission coefficient from transfer matrix method, the refractive index of VO_2 is assumed to be ~ 2.3 at the wavelength of 1600 nm. Also the scattering losses are not considered while calculating transmission and reflectivity parameter from TMM calculation. Therefore, here we are assuming angle dependent reflectivity and transmission are the reason of red spectral shift with s-polarized light incident at lower angle in the VO_2/DBR structure. As we have performed our experiment by keeping angle of incidence ~ 30°. It is highly likely, that the non-uniformity of VO_2 thin film surface causes the change in effective refraction angle of the incident light which transverse from the VO_2 thin film and goes into DBR and shift the whole transmission spectra towards the higher

wavelength. As our experiment are also performed at some angle deviated from the normal, we are assuming the right explanation of spectral shift is due to bending of light when passing through the VO_2 thin films during our specular reflectivity measurement. As we have neglected the optical scattering contribution in our analysis which can also contributes due to non-uniform surface of VO_2 thin films. However, it is quite complex to take the account of optical scattering and it require the more complicated analysis of Kubelka-Munk [40] which is out of context of this thesis and the present findings.

3.4 Summary

In summary, optical absorption enhancement of VO_2/1-D Photonic crystal structure by employing VO_2 thin film over SiO_2/TiO_2 based Bragg Reflectors tuned in IR region is demonstrated experimentally. Here, we have reported regulated optical transmission and reflection based on MIT of VO_2 nanostructures.

VO_2 nanostructures have been synthesized by thermolysis at temperature of 190°C of vandyl complex in the air ambient. Highly crystalline VO_2 nanostructures were synthesized by post annealing of moderately crystalline structure at 650 °C in argon atmosphere. For both MC and HC VO_2 nanostructures high temperature XRD confirms the phase transformation from monoclinic to rutile at and above 340 K respectively. VO_2 thin films fabricated with PVP composite exhibits optical transmission of ~ 14 % and ~ 10 % for MC and HC VO_2/PVP thin films respectively. VO_2 thin films with both crystallinity exhibits nearly similar transmission. Therefore, for the ease of synthesis in air environment which does not require high temperature annealing, MC VO_2 is employed for the further experimental study. It has been observed that DBR fabricated with four periodic stacks of SiO_2/TiO_2 able to obtain the ~ 20 % change in optical transmission. Upon increasing the periodicity of the stacks from four to seven has transmission of DBR ~ 10% with quite high reflection in stop band tuned around 1600 nm. Therefore, this controlled fabrication is very important parameter for designing a smart window with optimal number of layers for desired optical effects.

On casting MC - VO_2 over a high quality DBR with ~ 90 % reflection, there is nearly 100 % decrease in the optical transmission i.e. it reaches to 0.6 % at the temperature of 380 K with the

corresponding decrease in reflection with increase in temperature in the infra – red region of wavelength. This makes these hybrid VO_2/1D Photonic crystal based structure a potential candidate for Vanadium Dioxide based temperature regulated thermochromic absorbers for smart window applications and IR based sensors. Moreover, our hybrid design is more practical and simpler to implement even for large scale production as synthesized MC VO_2 can be synthesized with an ease in large quantity. The robustness of 1-D Photonic crystal fabricated could be easily implemented even for retrofitting applications. Further works in this direction is continued in chapter 4. There we have tailored the transition temperature of VO_2 by simple synthesis protocol using dopants. This will be useful for more advance applications to incorporate suitably doped VO_2 along with flexible 1D Photonic crystals made on flexible substrates tuned in the the entire IR wavelength even near to room temperature.

3.5 References:

[1] Meng Y, Li X, Wang S, Lau C, Hu H, Ke Y, Tan G, Yang J, Long Y, Flexible smart photovoltaic foil for energy generation and conservation in buildings, *Nano Energy*, **2022,** 91 , 106632.

[2] Aburas M, Soebarto V, Williamson T, Liang R, Ebendorff-Heidepriem H, Wu Y, Thermochromic smart window technologies for building application: A review, *Applied Energy*, **2019,** 255, 113522.

[3] Ye H, Long L, Zhang H, Gao Y, the energy saving index and the performance evaluation of thermochromic windows in passive buildings, Renewable Energy, **2014**, 66 , 215-221.

[4] Liang R, Sun Y, Aburas M, Wilson R, WuY, An exploration of the combined effects of NIR and VIS spectrally selective thermochromic materials on building performance, *Energy and Buildings*, **2019,** 201,149-162.

[5] Long L, Ye H, Discussion of the performance improvement of thermochromic smart glazing applied in passive buildings, *Solar Energy*, **2014**, 107, 236-244.

[6] Rajeswaran B, Pradhan J K, Ramakrishna S A and Umarji A M Thermochromic VO2 thin films on ITO-coated glass substrates for broadband high absorption at infra-red *frequencies J. Appl. Phys.* **2017** 122 163107.

[7] Cao Z, Xiao X, Lu X, Zhan Y, Cheng H and Xu G A simple and low-cost combustion method to prepare monoclinic VO2 with superior thermochromic properties *Sci. Rep*. **2016** 6 39154.

[8] Zhang Z, Gao Y, Chen Z, Du Z, Cao C, Kang L and Luo H Thermochromic VO2 thin films solution-based processing, improved optical properties, and lowered phase transformation temperature *Langmuir* **2010** 26 10738.

[9] Shao Z, Cao X, Luo H and Jin P Recent progress in the phase-transition mechanism and modulation of vanadium dioxide materials *NPG Asia Mater*. **2018**, 10, 581.

[10] Fan L, Chen Y, Liu Q, Chen S, Zhu L, Meng Q, Wang B, Zhang Q, Ren H and Zou C Infrared response and optoelectronic memory device fabrication based on epitaxial VO2 film *ACS Appl. Mater. Interfaces* **2016** 8 32971.

[11] Zhou J, Gao Y, Zhang Z, Luo H, Cao C, Chen Z, Dai L and Liu X VO2 thermochromic smart window for energy savings and generation *Sci. Rep*. **2013** 3 3029.

[12] Xu F, Cao X, Luoc H and Jin P Recent advances in VO2-based thermochromic composites for smart windows *J. Mater. Chem. C* **2018** 6 1903.

[13] Joannopoulos J D, Johnson S G, Winn J N and Meade R D Photonic Crystals: Molding the Flow of Light (Princeton, NJ: Princeton University Press) **2011.**

[14] Muallem M, Palatnik A, Nessim G D and Tischler Y R Room temperature fabrication of dielectric Bragg reflectors composed of a CaF2/ZnS multilayered coating *ACS Appl. Mater. Interfaces* **2014** 7 474.

[15] Lu Y J, Shan C X, Jiang M M, Li B H, Liu K W, Li R G and Shen D Z Enhanced emission from ZnO-based double heterostructure light-emitting devices using a distributed Bragg reflector *RSC Adv.* **2014** 4 1657.

[16] Lin S Y and Fleming J G Origin of absorption enhancement in a tungsten, three-dimensional photonic crystal *J. Opt. Soc. Am. A* **2003** 20 153.

[17] Iasilli G et al Luminescent solar concentrators: boosted optical efficiency by polymer dielectric mirrors *Mater. Chem. Front*. **2019** 3 429.

[18] Mbakop F K, Djongyang N and Ra¨ıdandi D One–dimensional TiO2/SiO2 photonic crystal filter for thermophotovoltaic applications *J. Eur. Opt. Soc. Rapid* **2016** 12 23.

[19] Atwater H A and Polman A 2010 Plasmonics for improved photovoltaic devices Nat. Mater. 9 205.

[20] Fahr S, Rockstuhl C and Lederer F Metallic nanoparticles as intermediate reflectors in tandem solar cells *Appl. Phys. Lett*. **2009** 95 121105.

[21] Barve A V, Lee S J, Noh S K and Krishna S Review of current progress in quantum dot infrared photodetectors *Laser Photon. Rev.* **2010** 4 738.

[22] Inan H, Poyraz M, Inci F, Lifson M A, Baday M, Cunningham B T and Demirci U Photonic crystals: emerging biosensors and their promise for point-of-care applications *Chem. Soc. Rev.* **2010** 46 366.

[23] Pitruzzello G and Krauss T F Photonic crystal resonances for sensing and imaging *J. Opt*. **2018** 20 073004.

[24] Adl H P, Bayat F, Ghorani N, Kandjani S A and Tajalli T A defective 1-D photonic crystal-based chemical sensor in total reflection geometry *IEEE Sens.* J. **2016** 17 4046.

[25] Beregovski Y, Hennig O, Fallahi M, Guzman F, Clemens R, Mendes S and Peyghambarian N Design and characteristics of DBR-laser-based environmental *sensors Sens. Actuators* **1998** 53 116.

[26] Devarapu G C R and Foteinopoulou S Mid-IR near-perfect absorption with a SiC photonic crystal with angle-controlled polarization selectivity *Opt. Express* **2012** 20 13041.

[27] Zhu M, Qi H, Wang B, Wang H, Zhang D and Lv W Enhanced visible transmittance and reduced transition temperature for VO2 thin films modulated by index-tunable SiO2 anti-reflection coatings *RSC Adv*. **2018** 8 28953.

[28] Rashidi A, Hatef A and Namdar A On the enhancement of light absorption in vanadium dioxide/1D photonic crystal composite nanostructures *J. Phys. D: Appl. Phys*. **2018** 51 51375102.

[29] Rashidi A, Hatef A and Namdar A Modeling photothermal induced bistability in vanadium dioxide/1D photonic crystal composite nanostructures *Appl. Phys. Lett*. **2018** 113 101103.

[30] Zou J, Peng Y and Lin H A low-temperature synthesis of monoclinic VO2 in an atmosphere of air *J. Mater. Chem. A* **2013** 1 4250.

[31] Zhang H, Xiao X, Lu X, Chai G, Sun Y, han Y, Xu G, A cost-effective method to

fabricate VO_2 (M) nanoparticles and films with excellent thermochromic properties, *Journal of Alloys and Compounds* **2015** 636 106 – 112.

[32] Xiao X, Zhang H, Chai G, Sun Y, Yang T, Cheng H, Chen L, Miao L, Xu G, A cost-effective process to prepare VO_2 (M) powder and films with superior thermochromic properties, *Materials Research Bulletin*, **2014,** 51 , 0025-5408.

[33] Wu C, Zhang X, Dai J, Yang J, Wu Z, Weib S and Xie Y, Direct hydrothermal synthesis of monoclinic VO2(M) single-domain nanorods on large scale displaying magnetocaloric effect, *J. Mater. Chem*., **2011**, 21, 4509.

[34] Xygkis M, Gagaoudakis E, Zouridi L, Markaki O, Aperathitis E, Chrissopoulou K, Kiriakidis G and Binas V Thermochromic behavior of VO2/polymer nano composites for energy saving coatings *Coating*s **2019** 9 163.

[35] Taha, M. et al. Insulator–metal transition in substrate-independent VO2 thin film for phase-change devices. *Sci. Rep*. **2017** 7, 17899.

[36] Rashidi A, Hatef A and Namdar A On the enhancement of light absorption in vanadium dioxide/1D photonic crystal composite nanostructures *J. Phys. D: Appl. Phys*. **2018** 51 51375102.

[37] Lova P Selective polymer distributed Bragg reflector vapor sensors *Polymers* **2018** 10 1161

[38] Gik H Y MSc Thesis University of Hull **2005.**

[39] Leem J W, Guan X Y and Yu J S Tunable distributed Bragg reflectors with wideangle and broadband **2014.**

[40] Kokhanovsky A A Physical interpretation and accuracy of the Kubelka–Munk theory *J. Phys. D: Appl. Phys.* **2007** 40 2210–16.

Chapter 4

W - Doped VO_2 nanostructures incorporated with tunable 1-D Photonic crystal as flexible Photo absorbers

4.1 Introduction

As discussed in chapter 1, Vanadium Dioxide VO_2 (M) is a well-studied material which exist in various complex polymorphs such as VO_2 (M), VO_2 (R), VO_2 (B), VO_2 (A), VO_2 (C), VO_2 (D) and VO_2 (P) [1]. Out of all these polymorphs, VO_2 (M/R) Phase is widely studied which shows reversible semiconductor to metallic transition around the temperature of 340 K [2]. Similarly, we have also briefly discussed in the chapter 3 that this transition occurs due to change in crystallographic variation in lattice upon reaching a certain temperature. Hence, semiconductor phase of VO_2 exists when lattice is in monoclinic phase which transmits the Infra-red (IR) radiations and the high temperature rutile phase, which is metallic in nature, reflects the IR radiations. This reflection of IR light by the metallic phase coated over glass substrate doesn't provide a reflection efficiency of more than 30% to 40%. To make it more efficient for practical design for smart glass industry, we have employed VO_2 (M) with tuned crystallinity, using its changing optical properties around temperature of 68°C along with a 1-D Photonic crystal structure. This 1-D Photonic crystal can regulate the selective wavelength of light by reflect it with ~ 100 % efficiency. So far VO_2(M/R) material is the only candidate which also come under the class of correlated material shows MIT (metal to Insulator transition) behaviors at such low temperature. But 68 °C is still quite high temperature for the various practical applications for commercial purpose in smart glass industry for smart window panel applications to contribute significantly in efficient building plans [3, 4]. However, this transition temperature can be reduced to room temperature by doping vanadium precursor with large ionic radius and high valance metallic ions than V^{4+}. Most frequently used dopant for this purpose are tungsten and molybdenum as they induce very large change in transition temperature even with small doping concentration [5]. There are various methods which can be used to synthesized W - doped VO_2(M) nanostructure. These are high cost chemical vapor deposition [6], magnetron sputtering [7], pulsed laser

deposition [8] and physical vapor deposition [9] etc. There are chemical routes which can be followed to synthesize pure VO_2 nanostructures. Sol gel method [10], homogenous precipitation [11] method and hydrothermal method [12] are the few examples of chemically assisted synthesis of VO_2 nanostructures. All these hydrothermal methods can be used to make high purity VO_2 nanocrystals due to ease of synthesis and can be used for large scale production due to low cost of these synthesis methods. VO_2 with various morphologies can also be synthesized using this method. One of this method involves the sealed autoclaves in which reaction is conducted at relatively high temperature under high pressure which leads to oxidation-reduction of reactions, along with precipitation and recrystallization. VO_2 synthesized with this method actually offers better crystallinity and crystals with few defects and have enhanced thermochromic properties. However, it was also noted that the quality of VO_2 thin films fabricated by dispersing Vanadium Dioxide nanoparticles into the polymer assisted resins can also perform equally well as compared to costly processes mentioned above. In this report, we have employed one step hydrothermal method and used vanadium precursors along with tungsten dopant to reduce the MIT transition temperature. Tungsten due to metallic nature, with ionic radius larger than V^{4+} ion, breaks the direct bonds of V-V ions, as a results there is formation of V^{3+} and W^{6+} ionic pairs [13, 14]. This causes the required reduction in the transition temperature for useful applications. Besides, there are theoretical calculations [15] which justify decrease of Tc with tungsten and molybdenum dopant with VO_2 nanostructures.

Flexible 1D Photonic crystal is the key component for flexible electronic and has various applications in thermal energy efficient devices [16]. Photonic crystal based structure can be used here to enhance the effective optical absorption. It is, therefore, utilized in many such application as optical absorbers [17]. There are various reports where 1-D Photonic crystals can act as back reflector or an absorptive medium for various luminescent materials [18], hence structure based on flexible 1D Photonic crystal is an important component for smart glass applications such as smart windows or doors in buildings for energy saving purpose [19]. Optical sensors designed with VO_2 layers sandwiched between two Bragg reflector has already been reported [20]. There are reports on smart windows which employs flexible polymer based 1D Photonic crystals [21,22]. Polymer based 1D Photonic crystals has limitations in fabricating uniform reflective surface, as spin coating over large area substrates are quite difficult. In this Chapter, we will report flexible 1D Photonic crystal fabricated over 5mm thick PET substrate with magnetron sputtering. We have

fabricated high quality 1D Photonic crystal with few layers of SiO_2/ Ta_2O_5. We have fabricated thin films having uniform sputtered over large area with high reflectivity, which will serve the purpose of making smart windows working more efficiently as it also offers retrofitting of windows. There have been theoretical predictions of VO_2 hybridized 1-D Photonic crystal structures that can enhance Infra-red absorption [23], Chapter 3 gives experimentally modified design of the theoretical predication [24, 25] however, that design also have few limitations for practical implementation. In this chapter, we are implementing a further improved design with flexible 1D Photonic crystals which can be tuned at IR wavelengths by fabricating SiO_2/Ta_2O_5 based alternating layers on a PET substrate and employing tungsten doped VO_2 nanoparticles over it. In this chapter, we have implemented VO_2(M) and tungsten doped VO_2(M) over flexible 1-D Photonic crystal and observed significant change in optical transmission and reflection even near to room temperature. On incorporating W - VO_2 over 1-D photonic crystal, the optical transmission almost vanishes in the stop band region of the photonic crystal, with corresponding decrease in reflection. Both optical transmission and reflection measurements are carried out at varying temperatures. We observed a definite optical absorption enhancement in W - VO_2 over 1 - D photonic crystal structures fabricated over PET substrates. Therefore, we propose that these flexible hybrid structures provide more practical design for smart glass industry. As a result, this hybrid structure is a suitable design for smart windows in building and automobiles which can also be retrofitted over existing glass windows as well.

4.2 Materials and Methods for synthesis

4.2.1 Chemicals and material Used

All chemicals are used as purchased without any further purification. Vanadium Dioxide sulphate ($VOSO_4$, 99%, Sigma – Aldrich), ammonium tungstate ($(NH_4)_{10}W_{12}O_{41}.xH_2O$, Sigma – Aldrich), sodium hydroxide (NaOH, 99%, Sigma – Aldrich), ethanol and polyvinylpyrrolidone (PVP, Sigma – Aldrich) and de – ionized water, Silicone Dioxide (SiO_2) and tantalum oxide (Ta_2O_5) sputtering targets of 0.25-inch thickness and 2-inch diameter, Pre cleaned microscope glass slides (J. Melvin Freed Brand) and Polyethylene terephthalate (PET sheet, 5 mm thickness) sheets.

4.2.2 Synthesis Procedure of VO_2(M) and W- doped VO_2 (M) nanoparticles

To synthesized VO_2 and W - doped VO_2 nanoparticles, a modified facile hydrothermal method is followed. In a typical chemical reaction, we synthesized pure monoclinic VO_2 nanoparticles. In 20 ml of deionized water, 20 mmol of vanadium oxide sulphate was added and dissolved completely by constant magnetic stirring. To obtained solution 10 M Sodium hydroxide (NaOH) solution was added dropwise till the solution pH reached to 9.0. The solution was then centrifuged several time to yield a brown slurry. The obtained slurry was further added and mixed into 15 ml of deionized water. Finally, the resulting brown solution was transferred into 20 ml Teflon line stainless steel autoclave. The autoclave is tightened and kept into pre-heated oven at 260 ^{o}C for 8 hours. After the reaction took place, the autoclave was allowed to cool down completely to room temperature. A black precipitate is collected, the isolated precipitate was centrifuged with deionized water and ethanol at least three times and the product obtained after subsequent washing was dried at 60 ^{o}C in an oven for at least 12hrs.

To synthesize the tungsten doped VO_2 nanoparticles, appropriate amount of ammonium tungstate with different atomic percentages is added in the above synthesis method to produce W - doped VO_2 nanoparticles. Here, we have synthesized 0.7 – 1.3 at % W - doped VO_2 samples. Ammonium tungstate was added to the 15 ml of deionized water, for complete dissolution it is magnetically stirred for 30 min at 70 ^{o}C. Brown slurry was added to the above solution after it cooled down completely and stirred for another 30 min, then transferred into the autoclave which is kept at 260 ^{o}C for 8 hours. By changing the atomic ratio of ammonium tungstate, different composition of tungsten doped VO_2 (M) nanoparticles are obtained.

4.2.3 Calculation of atomic ratio for tungsten doping concentration

Molecular weight of Ammonium tungstate = 2956. 30 amu

Atomic weight of tungsten = 183.84 amu

Each ammonium tungstate contributes 12 tungsten atom

Weight of vanadium oxide sulphate taken = 3.26 g

Therefore, required amount of ammonium tungstate to be taken for 1.1 at% of W =

= (2956.30 × 35.8) / 2196

~ 48 mg

4.2.4 Fabrication and characterization of Distributed Bragg Reflectors

SiO_2 / Ta_2O_5 deposited alternately to fabricate periodic stacks using Moorefield's Minilab ST80A magnetron sputtering deposition system. 0.5 × 0.5 cm^2 glass and PET substrates are used to fabricate DBR's in Infra-red range. Before the deposition, the base pressure of the sputtering chamber was noted around ~ 1×10^{-7} mbar. While fabricating SiO_2 and Ta_2O_5 the sputtering chamber was kept at 7.0×10^{-3} mbar. Profiliometer (Veeco, Dektak 150) was used to calibrate the thickness of SiO_2 and Ta_2O_5 layers. Four Bragg reflectors over PET substrate with stop band central wavelength are tuned at λ_0 ~ 1530 nm, 1560 nm, 1680 nm and 1615 nm respectively. Bragg reflectors fabricated over glass substrate, the central stop wavelength is chosen to be λ_o~ 1530 nm and 1560 nm with four and seven stacks of SiO_2/Ta_2O_5. Thickness of individual layer of Bragg reflectors is chosen to be quarter of the stop wavelength i.e., $d = \lambda/4n$, therefore, all the Bragg reflectors fabricated here are quarter wavelength stacks with angle of incidence assumed to be normal. Here, λ is the central wavelength of the stop band, n is the refractive index of the materials used i.e. n_{SiO2}– 1.45 and n_{Ta2O5}– 2.13 respectively. Therefore, thickness for DBR tuned at 1530 nm are calculated to be d_{SiO2}~ 264 nm and d_{Ta2O5}~ 180 nm and for DBR tuned at 1560 nm the thicknesses were calculated as, d_{SiO2} ~ 270 nm and d_{Ta2O5}~ 185 nm respectively. All thickness was calibrated experimentally using the Profiliometer. For Bragg reflectors fabricated over PET, the thicknesses are calibrated as follows - for λ_0 ~ 1615 nm, d_{SiO2} ~ 290 nm and d_{Ta2O5}~ 200 nm and for λ_0 ~ 1680 nm, d_{SiO2} ~ 280 nm and d_{Ta2O5}~ 190 nm respectively. Fabricated 1D Photonic crystals over PET and glass both have comparable surface roughness of about ± 2nm as measured with AFM. Therefore, 1 D photonic crystals fabricated over PET substrate were quite uniform over large area of the substrate.

4.2.5 Fabrication of VO_2/PVP and W-VO_2/PVP composite thin film

To fabricate thin films of VO_2 and W-doped VO_2 along with Polyvinyl Pyrrolidone (PVP) composite over glass and PET substrate, the as-synthesized VO_2 and Tungsten Doped VO_2 nanoparticles were first grinded into a fine powder and then dispersed into PVP. The Molecular weight of the PVP used was nearly 10,0000. To disperse VO_2 and W- doped VO_2 nanoparticles into Polyvinyl Pyrrolidone (PVP), the ratio of nanoparticles with PVP is kept to be 1:4. Some different concentration ratio of W-VO_2 and VO_2 with PVP also tried but the best results of transmission modulation are observed with 1:4 ratios only. Therefore, one part of VO_2 and W - VO_2 nanoparticles were added to 4 part of PVP and mixed with 1 ml of ethanol for at least 12 hours to form a uniform slurry. The obtained slurry was later spin coated over glass and PET substrate and dried at 70°C for 5hrs. Uniform films of VO_2 and W - doped VO_2 with PVP composite were fabricated over glass and PET substrate of size 0.5 × 0.5 cm^2. The amount of VO_2/ PVP and W-VO_2/ PVP is same in all cases to fabricate thin films i.e. 60 µl of slurry is used to fabricate all thin films. Thickness of the films are calibrated by changing the speed of spin coating. The film thickness over the PET substrate is found to be ~ 160 ± 10 nm. which is calibrated at the spin coating of 3500 rpm measured with FESEM cross-section as shown in Figure 4.1 below.

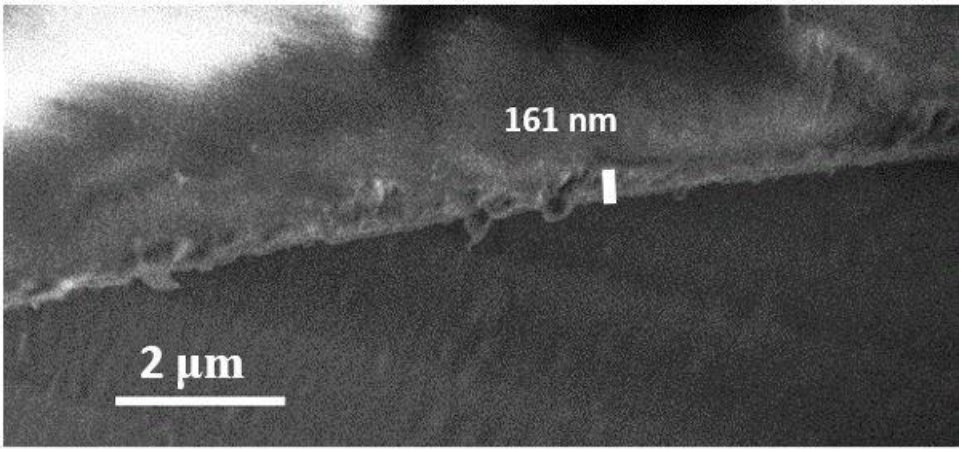

Figure 4.1 Showing the FESEM cross sectional image with VO_2 thin film deposited with thickness of 160 ± 10 nm.

While preparing the thin films over the PET substrate, PET substrate was subjected to rigorous surface treatments to ensure the good adhesion of the thin films. PET substrate was first cleaned

with IPA through sonication before use. Also these substrates are quite robust and can survive the temperature of 150°C. This factor is very important for heating performance of PET substrate as s as these are heated and cooled several times during the experiments. We have also provided the specification of PET bought from Sigma-Aldrich in the material section above.

4.3 Structural characterization of VO_2 (M) and W – doped VO_2(M)

4.3.1 Morphological analysis of VO_2 (M) and W - doped VO_2 (M) nanostructures

VO_2 (M) and W - doped VO_2 (M) synthesized by one step hydrothermal method indicates irregular morphologies as shown in Figure 4.2.

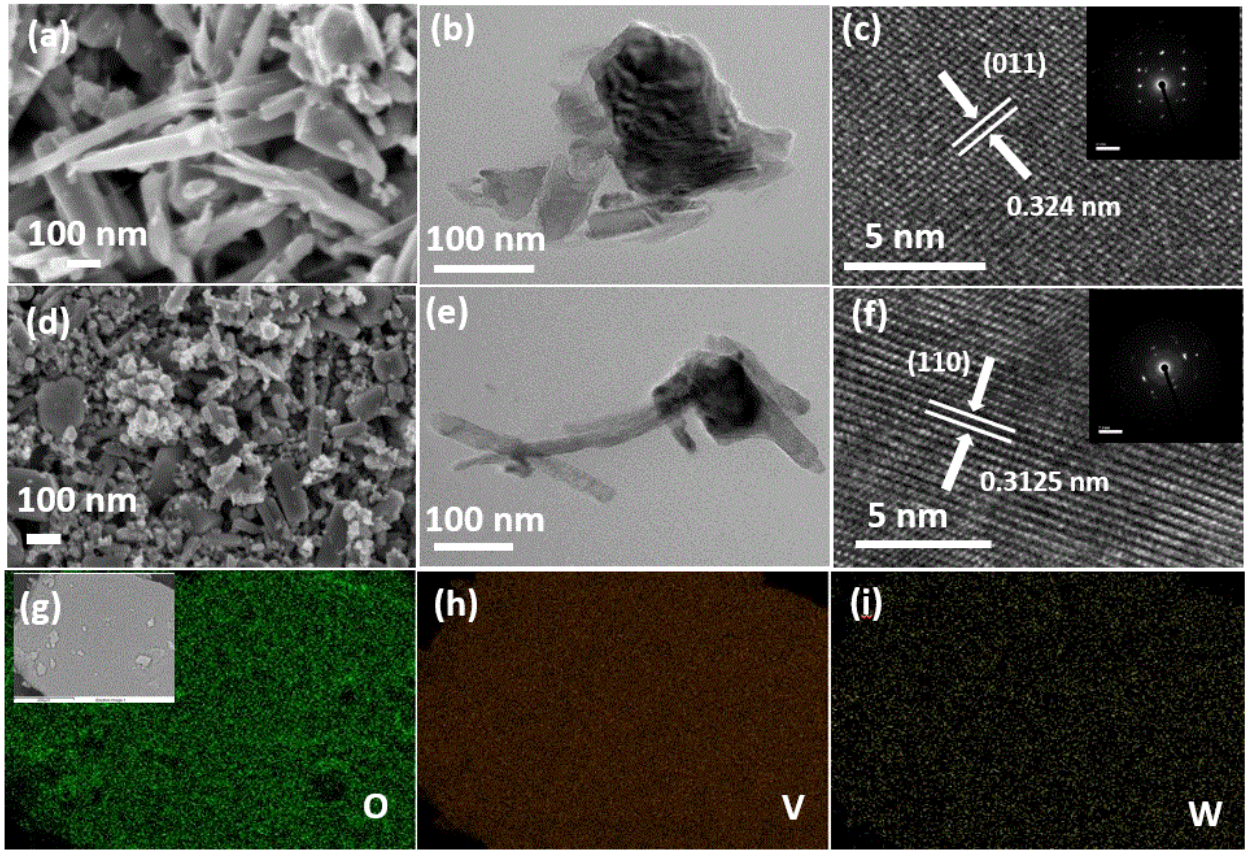

Figure 4.2 (a) and (d) representing the FESEM images of the Pure VO_2 and 1.1 at % W-doped VO_2 nanostructures. With (b) and (e) showing the TEM images of Pure VO_2 and 1.1 at % W-doped VO_2 nanostructures clustered together along with fig (c) and (f) representing the High Resolution TEM lattice fringes of both Pure VO_2 and 1.1 at % W-doped VO_2 nanostructures, inset including the SEAD pattern and fig. (g), (h) and (f) showing the elemental mapping of EDS indicating the uniform distribution of elements O, V and W at 1.1 at % W-doped VO_2 nanostructures only.

Both pure VO_2 (M) and tungsten doped VO_2 (M) nanoparticles exhibits Nano rod like morphologies. The size of rods varies from 70 to 100 nm. However, few of these rods are uneven in length as shown in FESEM images of Figure 4.2 (a) and 4.2 (d). There is no significant difference between the morphologies pure VO_2 (M) and tungsten doped VO_2(M) nanostructures was observed. As shown in Figure 4.2, figure 4.2(c) and 4.2(f) are showing the HR TEM images of Pure VO_2 (M) and W-doped VO_2(M), Pure VO_2(M) displaying the lattice fringes spacing of 0.324 nm which is associated with (011) plane of monoclinic phase of VO_2(M). HR TEM images of W- doped VO_2 has the lattice spacing of 0.312 nm and the associated plane to this spacing is (110). These results are in good agreement with the reported rutile phase of the VO_2. It is also evident that the rods are favored to grow in the direction of plane along (110). The formation of clear fringes in high resolution TEM images is a good indication of good crystallinity of as synthesized VO_2 nanostructures. Whereas, in tungsten doped VO_2, we don't see any lattice fringe belonging to WO_3 in the HRTEM image. Therefore, this clearly indicates the complete incorporation of tungsten atoms into the vanadium dioxide crystal lattice and transforming it into rutile structure even at room temperature [26]. To know the tungsten is doped uniformly and homogenously into vanadium dioxide, Figure 4.2 (g) – (k) showing the EDS elemental mapping also known as Energy Dispersive X-ray spectroscopy as discussed in Chapter 2. EDS of W-doped VO_2 nanostructure represent the elemental mapping of W, O and V respectively. The elemental mapping clearly indicates that the tungsten is homogenously doped into vanadium Dioxide. Figure 4.3. Showing the elemental mapping of Pure VO_2 along with the atomic ratios.

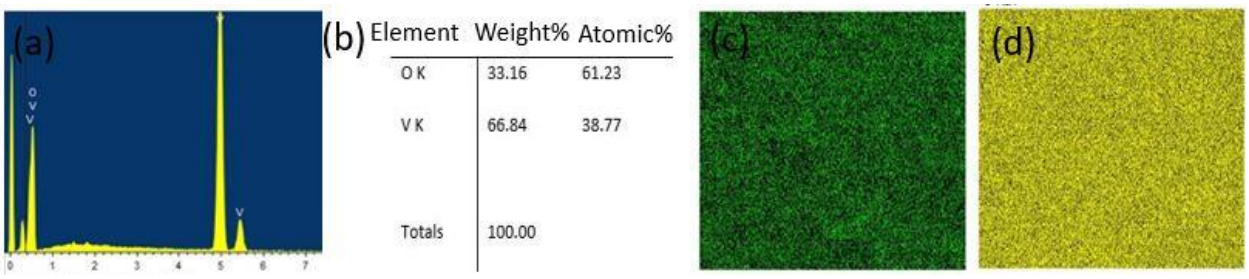

Figure 4.3 (a) and (b) are atomic ratio of Vanadium and oxygen in Pure VO_2 and (c) and (d) are elemental distribution of vanadium and oxygen in Pure VO_2 (M).

Therefore, both FESEM and TEM images giving the morphological evidences of complete incorporation of tungsten into vanadium dioxide lattice. In general, the physical properties of VO_2

material are highly dependent upon this morphology due to surface and size effects [27, 28]. Although there is no unified general rule which can relate the morphology to their physical property of nanostructure. Nevertheless, inducing a dopant into the material will causes the strain in the crystal and changed surface or interfacial energy leads to increase in surface to volume ratios. Still we do not see any morphological change between Pure VO_2 and 1.1 at. % W- doped VO_2 nanostructures. Therefore, from our observation it is difficult to give an exact explanation for the observed random morphologies of both nanostructures. Although there are differences in crystallinity of VO_2 and 1.1 at. % W - VO_2 nanostructures which clearly indicated as XRD peak splitting. This will be discussed in the next section.

4.3.2 Structural analysis of VO_2 (M) and W - doped VO_2 (M) nanostructures

XRD diffraction pattern of pure VO_2 (M) with different atomic ratio of tungsten doped VO_2 (M) nanostructures are shown in Figure 4.4. Pristine VO_2 (M) diffraction peaks are in good match with standard XRD pattern of VO_2 in monoclinic phase with JCPDS: 82 – 0661. As we have already discussed the doping the suitable amount of tungsten in VO_2(M) expedite the formation of rutile phase VO_2(R) at the room temperature itself. XRD diffraction peaks of 1.1 at. % W - VO_2 nanostructure are in good match with JCPDS: 79-1655 of rutile phase. XRD pattern of doped VO_2 nanostructure clearly indicating the absence of tungsten and its derivative peaks. Therefore, confirming the incorporation of tungsten atoms in the VO_2 lattice completely. One of the indication of transformation from monoclinic to rutile phase with doping is the shifting of diffraction peak at 27° toward the lower angles. This shifting is due to the substitution of W^{6+} ions in the vanadium dioxide lattice. According to the Bragg's law, as the tungsten ion is larger in size than the vanadium atom, the calculated inter-planar distance will increase hence, this results into the shifting of peak as shown in Figure 4.4 (b). vanadium dioxide lattice will expand and it undergoes notable amount of tensile stain when doped with tungsten atoms [29]. Due to this tensile strain there is structural phase transformation from the monoclinic to rutile even at room temperature which lead to the change in the unit cell dimension. For Pure VO_2 (M) nanostructure, the highest peak is at 2Θ = 28.15 with corresponding lattice plane (011) having the d – spacing of 0.324 A°. Upon optimal doping of tungsten with 1.1 at. %, the highest peak will be shifted to 2Θ = 27.86 and the d spacing is measured to be around 0.312 A°. No XRD diffraction peak corresponds to ammonium tungstate

or any other tungsten impurity in XRD is the clear confirmation of formation of VO_2 (R) phase even at the room temperature. From figure 4.4 (b) it is quite evident that optimal doping for obtaining VO_2 (R) phase is 1.1 at. %.

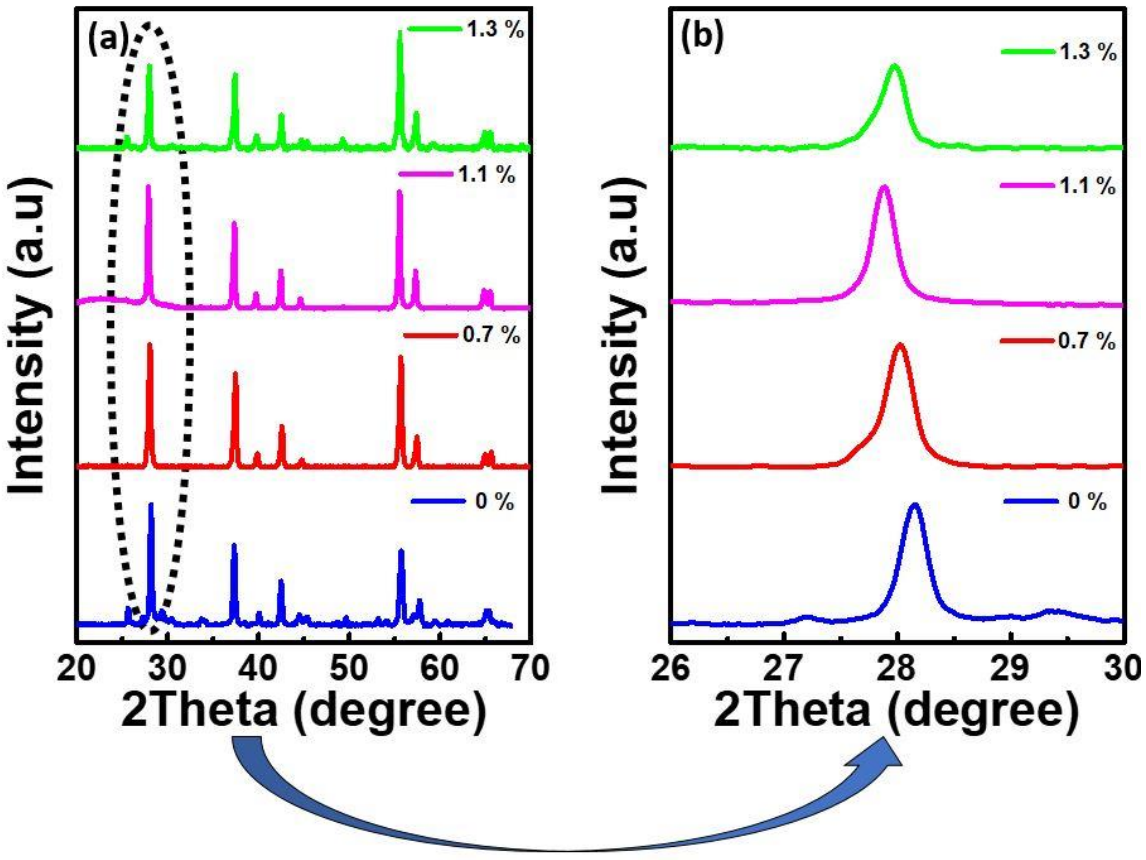

Figure 4.4 Representing the XRD diffraction pattern of Pure VO_2(M) and W-VO_2 (M) with concentration of tungsten as an dopant with (b) giving the magnified view of the highest and the characteristic peak which is at $2\Theta = 28.15^{o}$ with corresponding lattice plane of (011) M1 phase shift towards the lower angle i.e. $2\Theta = 27.86^{o}$ which corresponds to (110) R1 Phase.

To further characterize and confirm the phase transformation of VO_2 monocline to VO_2 rutile with doping we have performed high temperature *in situ* XRD measurement for Pure VO_2 (M) and 1.1 at. % tungsten doped VO_2 nanostructures. HT – XRD of Pure VO_2 (M) is shown in Figure 4.5 (a) clearly indicating the structural transformation from monoclinic VO_2(M) to rutile VO_2 (R) at and above the temperature of 68^{o}C [30]. Below the temperature of 68 ^{o}C, XRD peaks were matching with monoclinic phase (JCPDS: 82 – 0661) and as the temperature increases above 68^{o}C, the XRD peaks are in good match with rutile Phase of VO_2 as confirmed by JCPDS: 79-

1655. Apart from this, there is significant shift in highest intensity peak in range of 26º≤ 2Θ≤ 29º, with increase in temperature is observed. Along with peak shift, the (011) miller plane associated with monoclinic phase of VO_2 transforms into (110) rutile plane of VO_2 Phase. In addition, there is splitting of single peak around 65º into double peak in the range of 64º≤ 2Θ≤ 66º, upon increasing the temperature, the single peak at 68º below transition temperature corresponds to (310) M plane of monoclinic phase, and above the phase transition, the twin peaks corresponds to (130) R and (002) R rutile planes. Therefore, HT-XRD confirms the phase transition from monoclinic to rutile phase above the transition temperature of 68ºC.

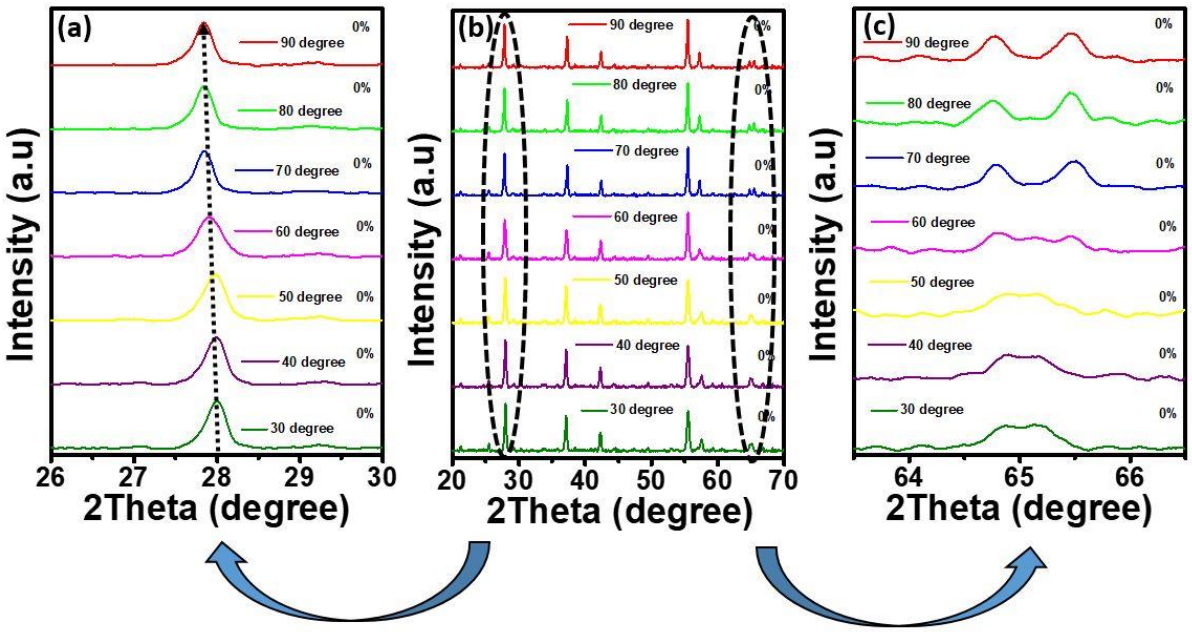

Figure 4.5 Representing the High temperature XRD of Pure VO_2 (M) with (a) showing the shift in the highest intensity peak in the range of 27º≤2Θ≤28ºwith temperature increase above transition temperature of 68ºC and (b) showing the XRD of Pure VO_2 nanostructure with increase in temperature and (c) showing the gradual splitting of the single peak corresponds to (130)M plane of monoclinic phase into doubly peaks corresponds to (002) R and (310) R planes associated with rutile phase.

Figure 4.6 representing the high temperature XRD of 1.1 at. % tungsten doped VO_2 nanostructure. Figure 4.6 (a) showing the highest intensity peak with increase in temperature and no shift of peak is observed with increase in temperature. The single peak around 65º splits into two peaks in the range of 64º≤ 2Θ≤ 66º just above the temperature of 30 ºC. These are significant evidences to

show that 1.1 at. % tungsten doped VO_2(M) is already in the rutile phase around the room temperature.

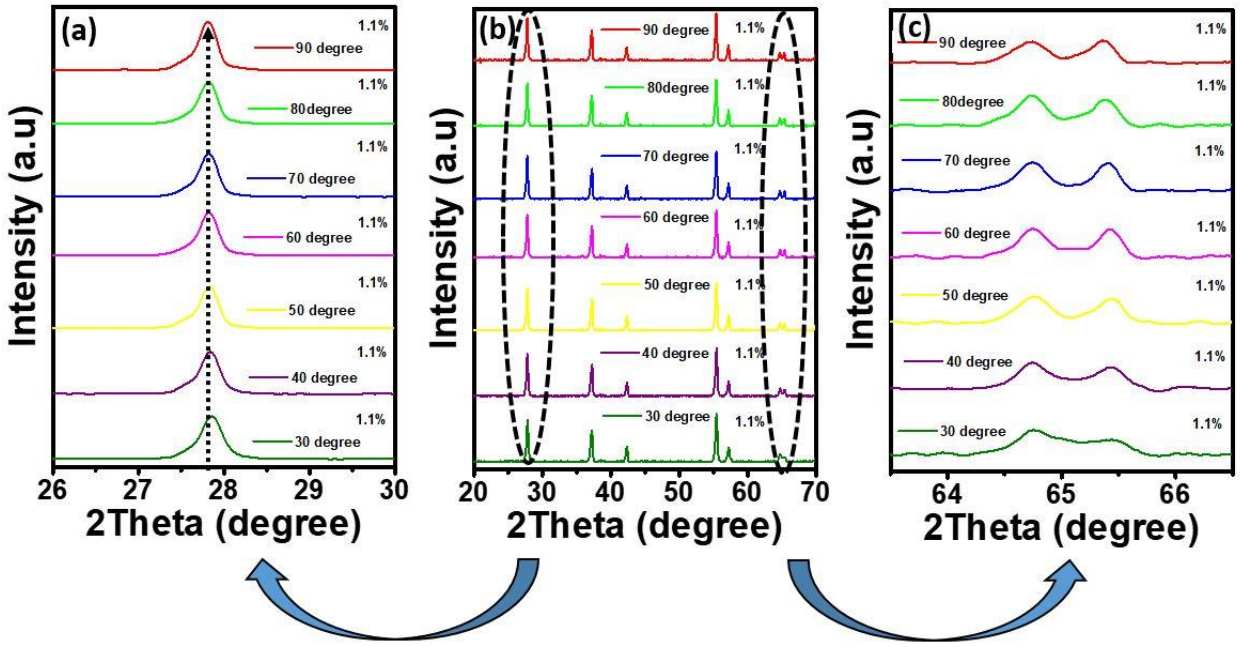

Figure 4.6 representing the High temperature XRD of 1.1 at.% tungsten doped VO_2 nanostructure (a) showing that there is no shift in the highest intensity peak in the range of $27^{o} \leq 2\Theta \leq 28^{o}$ with increase in temperature and (b) showing the XRD pattern of 1.1 at. % doped W-doped VO_2(M) both below and above the transition temperature and (c) showing the gradual splitting of single peak corresponds to (130) M monoclinic phase into double peaks corresponds to (002) R and (310) R planes of the rutile phase above the 30ºC.

Hence, 1.1 at. % tungsten doped VO_2(M) thin films with PVP is employed on PET and glass substrate for further optical analysis along with Pure VO_2 for comparison.

4.4 Optical analysis of VO_2 (M) and W - VO_2(M) thin films

As shown above, Tungsten doping into VO_2 (M) nanostructure is an effective way to reduce the transition temperature from 68°C to room temperature. From our observations and analyses, it is found that 1.1 at % for W- doping is the best performer among all the doping atomic concentration. The Figure 4.7 (shown below) clearly indicates that 1.1 at. % doped W-VO_2 transmission spectra is already in lower IR transmitting state as compared to other doping concentrations.

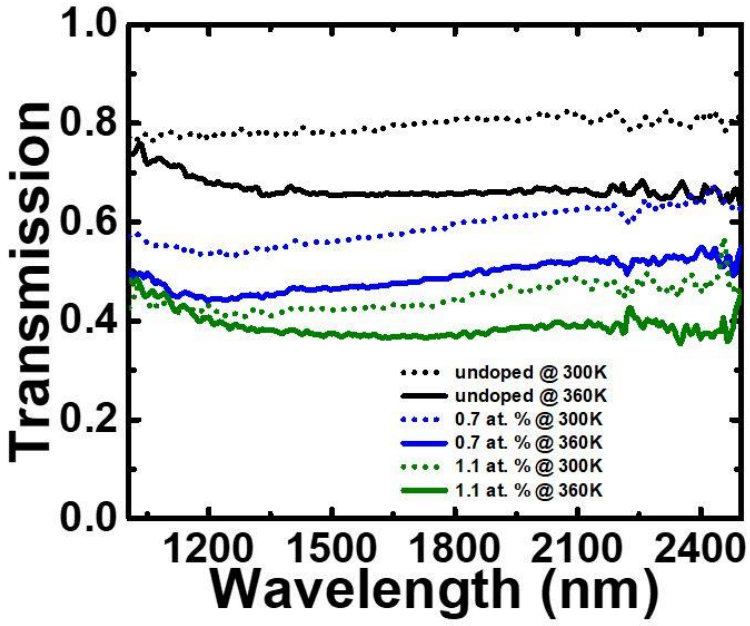

Figure 4.7 Representing the transmission spectra of Undoped VO_2 (M) , VO_2(M) with 0.7 at. % doping and VO_2 (M) with 1.1 at. % doping concentration respectively.

Now optical transmission spectra of 1.1 at. % W – doped VO_2 thin films with Undoped VO_2 thin films for comparison is shown in Figure 4.9. The inset represents the reversible thermal hysteresis while increasing and decreasing the temperature. It has been observed that for undoped VO_2 optical transmission modulation of VO_2 thin films i.e. $\Delta T \sim 16$ % with increase in temperature from 300 K to 380 K and for 1.1 at. % W - doped VO_2 the transmission modulation is found to be $\Delta T \sim 7$ % with increase in temperature. The thickness of thin films with PVP composite was measured with FESEM cross section imaging as shown in Figure 4.1 above. To make the films of

equal and uniform thicknesses, equal amount of sample is taken in all cases i.e. 60 µl. The thickness of the films are measured to be ~ 160 ± 10 nm. The thin films are fabricated via spin coating the VO_2/PVP slurry over the PET and Glass substrate as shown in Figure 4.8. But as PET substrates offer flexibility so further measurements were carried out on PET substrates. From Figure 4.8 (a), the undoped VO_2 /PET structure showing the transmission around 73 % at the temperature of 300 K, with increase in temperature, there is significant change in transmission of the VO_2/PET thin film around the temperature of 340 K.

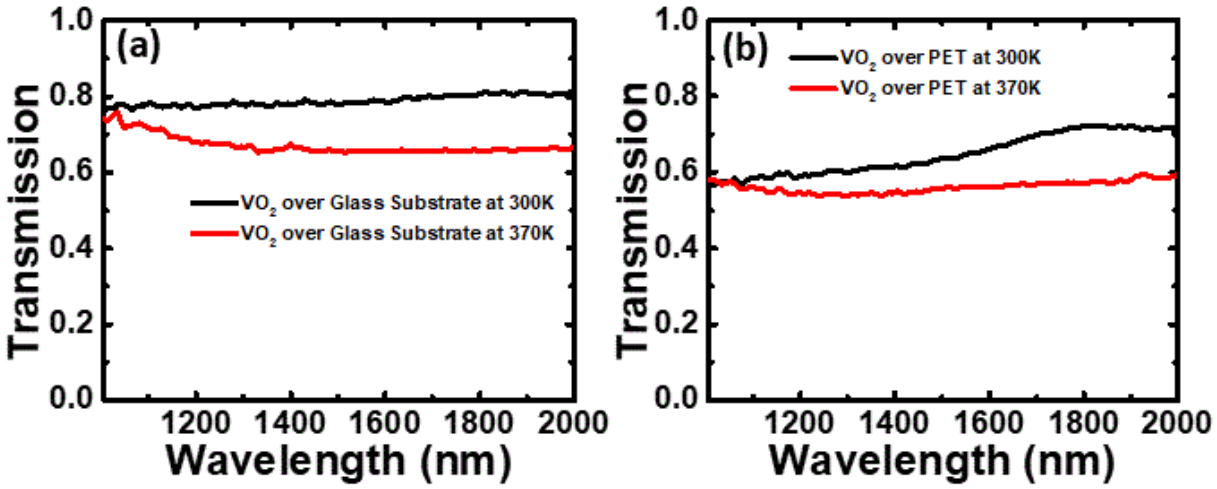

Figure 4.8 (a) Representing the transmission spectra of undoped VO_2 /PVP thin film over glass substrate and (b) showing the transmission spectra of un doped VO_2/PVP over PET substrate with increase in temperature from 300K to 370K, both films showing the nearly equal transmission modulation of ~ 16 % with increase in Temperature.

The transmission of the thin film decreases to 57 % when temperature reaches to 370 K at wavelength 1730 nm, hence the calculated optical transmission modulation at wavelength of 1730 nm is (ΔT) ~ 16 % with increase in temperature from 300 K to 370 K. Therefore, the as synthesized undoped VO_2 (M) nanoparticles has a phase transition around the temperature of ~ 340 K with good optical transmission modulation as the phase transforms from monoclinic to rutile and is matching well with the previous reported literature [30]. Similarly, for 1.1 at. % W-doped VO_2 thin film, the transmission drops from 43 % to 37 % with increase in temperature from 300 K to 370 K, therefore the calculated optical transmission modulation is (ΔT) ~ 7 % which is a notable change in transmission around and above the temperature of 310 K. From the inset figures, the

optical picture of both undoped VO_2 and 1.1 at. % W – doped VO_2, the thin films are visibly transparent in nature. From the results it is quite evident that phase transition temperature for 1.1 at. % W – doped VO_2 reduces from 340 K to 310 K as supported by the previous reports, tungsten dopant promotes the slight distortion in vanadium dioxide lattice by forming the bonds between V-V bond with W^{6+} ions, which leads to the reduction of transition temperature [32]. However, if the tungsten is doped in Vanadium dioxide lattice in higher amount, it leads to excess amount of free tungsten ions which will hinder the phase transition temperature and VO_2 (M) properties.

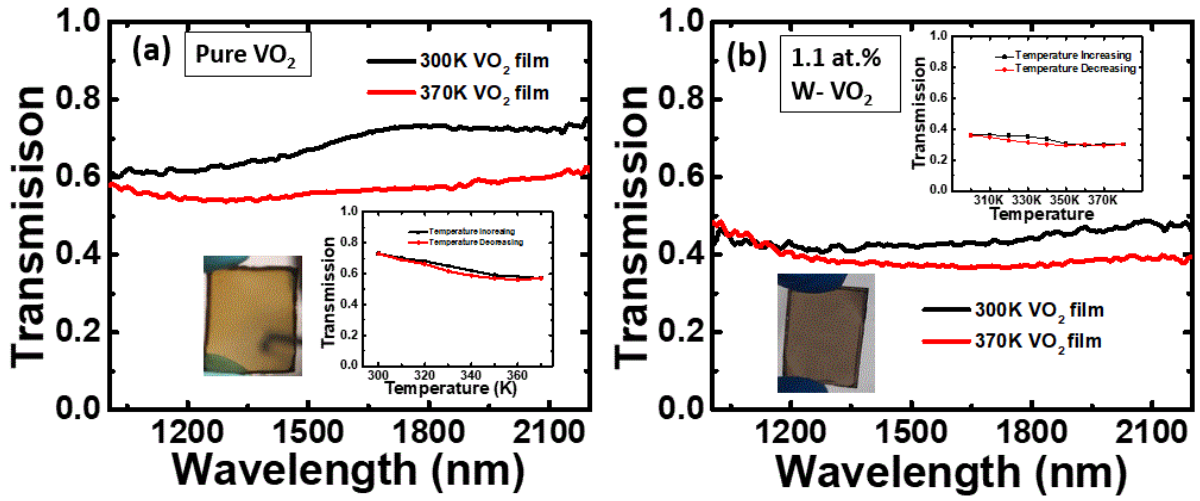

Figure 4.9 (a) Showing the transmission spectra of undoped VO_2 with PVP over PET substrate with increase in temperature from 300 K to 380 K, the transmission modulation of thin film is nearly $\Delta T \sim 16$ % at wavelength of 1735 nm along with inset showing the reversible hysteresis of transmission with increasing and decreasing temperature and (b) showing the transmission spectra of 1.1 at. % tungsten doped VO_2 thin film with transmission modulation of $\Delta T \sim 7$ % with optical picture in inset along with reversible temperature hysteresis.

Inset of Figure 4.9 (a) and (b) showing the reversible thermal hysteresis loop with increasing and decreasing temperature of both undoped VO_2 and 1.1 at. % W - doped VO_2 thin films. The thermal hysteresis width of both undoped and doped VO_2 thin film is calculated to be 0.04 at the transmission wavelength of 1730 nm. The hysteresis width of the reversible thermal loop is quite narrow. Narrow hysteresis width imputes, the small granular size of the undoped VO2 and tungsten doped VO_2 nanostructure. Also it represents good crystallinity of the nanostructures with good thermal response of the film [32, 33]. From the optical analysis of VO_2 and W - VO_2 thin film indicates the substantial transmission reduction in undoped VO_2 thin films and 1.1 at. % W – VO_2

thin films around the temperature of 340 K and 310 K respectively. Therefore, these thin films with flexible 1D Photonic crystal tuned in IR region are an efficient way to enhance the optical absorption. Therefore, further experiments are carried on glass as well as PET based DBR substrates.

4.5 The Fabry – Perot type optical effect on W-VO_2/ 1-D Photonic Crystal structure

The schematic in Figure 4.10 displaying the temperature dependent reflection and transmission measurement of the Pure VO_2 and 1.1 at. % W-doped VO_2 incorporated with Flexible PET based 1-D Photonic crystal.

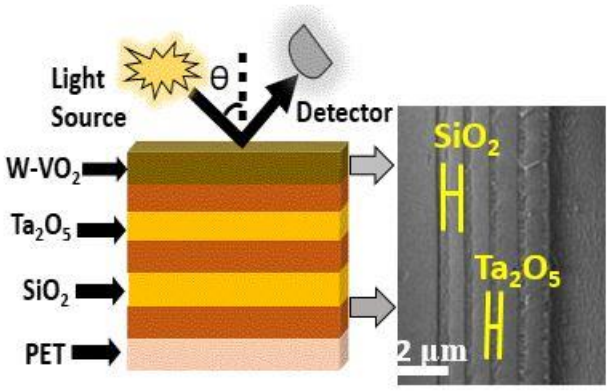

Figure 4.10 Representing the schematic of W-VO_2 / 1D Photonic crystal structure in reflection geometry along FESEM cross sectional image of SiO_2/ Ta_2O_5 DBR fabricated over PET substrate.

Flexible substrate such as PET is a promising candidate to offer flexibility in order to maintain the structural integrity if employed over the smart glasses such smart windows or smart doors etc. Figure 4.11 (b) and (c) showing the PET DBR which has transmission ~ 40 % and it is fabricated by alternately depositing SiO_2/Ta_2O_5 five stacks over PET substrate. The central stopband wavelength of the tuned DBR is around ~ 1595 nm. 160 ± 10 nm thick Undoped VO_2 thin film is spin coated over PET DBR. The optical transmission from the overall structure further reduces to nearly 16% along with the red shift in the transmission spectra from 1595 to 1620 nm i.e. ~ 40nm red shift in VO_2/DBR structure. As we have already discussed in chapter 3, the possible reason of

this optical shift can be the fabrication of extra layer over DBR due to which there is increase in overall optical thickness of the structure which causes the overall interfere pattern from the VO_2/DBR structures to be shifted toward the higher wavelength when the light passes through the overall structure [34, 35]. The undoped VO_2/DBR/PET structure displaying ~ 46 % reduction in transmission as compared to the film over VO_2/PET structure. This transmission further reduces to 14 % as the temperature increase to 380 K. This decrease in transmission occur in the wide range of wavelength i.e. from 1400 – 1800 nm, although variation in transmission curves as the temperature increases is not clearly visible in the stop band but the variation in transmission can be significantly seen in side bands of the photonic crystal where photonic crystal capable of transmitting substantially.

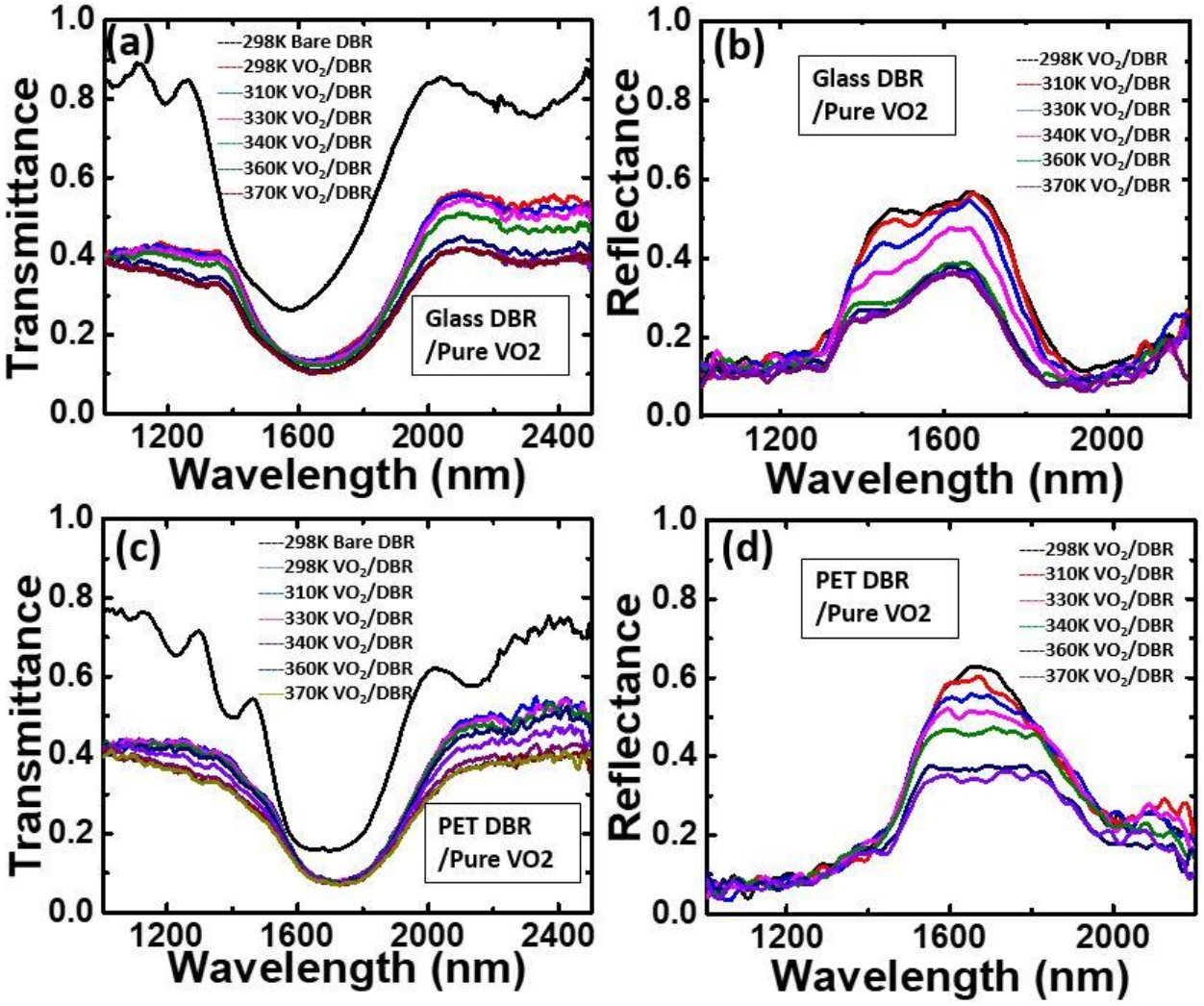

Figure 4.11 (a) showing the transmission of undoped VO_2/DBR over PET substrate DBR is tuned at 1595 nm with transmission ~ 40 % on increasing the temperature to 380 K , the overall transmission through the structure decreases to ~ 17 % with red sift of 40 nm i.e. from 1595 nm to 1630 nm respectively. (b) showing the reflectance measurement from the overall structure with increase in temperature to 380K (c) representing the DBR over PET tuned at central stop wavelength around 1610 nm and it transmission from the structure reduces to ~ 1600 nm at 2100 nm along with (d) corresponding reflectance spectra of the undoped VO2/DBR structure with temperature increases to 370 K.

However, we have calculated fractional change in transmission i.e. T_{380K}/T_{300K} in the entire wavelength region and it is calculated to be ~ 2. Figure 4.11 (b) showing the corresponding reflection spectra of the undoped VO_2/DBR/PET structure. As the DBR is ~ 70 % reflecting in the stop band as compared to the side bands, decrease in reflection with increase in temperature is clearly visible in the stop band wavelength region as compared to the side bands. Therefore, the

optical reflection band significantly decreases ~ 30 % at and around the wavelength of 1595 nm as the temperature rises to 380 K. whereas, the transmission in the side bands of the bare DBR is nearly 90 % along with the reflection which is 50 %, consequently prominent variation in the reflection with increase in temperature cannot be visibly observed in the side band of the reflection measurement. We have calculated the fractional reflection change i.e. R_{300K} /R_{380K} in the entire wavelength region and it is calculated to be ~ 1.5 in wavelength raging form 1300 -1700 nm. There is one to one correspondence between the transmission and reflection measurement of VO_2/DBR/PET Structure. Therefore, we concluded that even few stack of Bragg reflector was able to enhance the optical absorption significantly of the undoped VO_2(M) thin film.

Figure 4.11 (c) and (d) representing the reflection and transmission spectra of flexible Bragg reflector tuned at stopband central wavelength at and around 1680 nm, the Bragg reflector is fabricated with seven stacks of SiO_2/Ta_2O_5 over PET substrate.

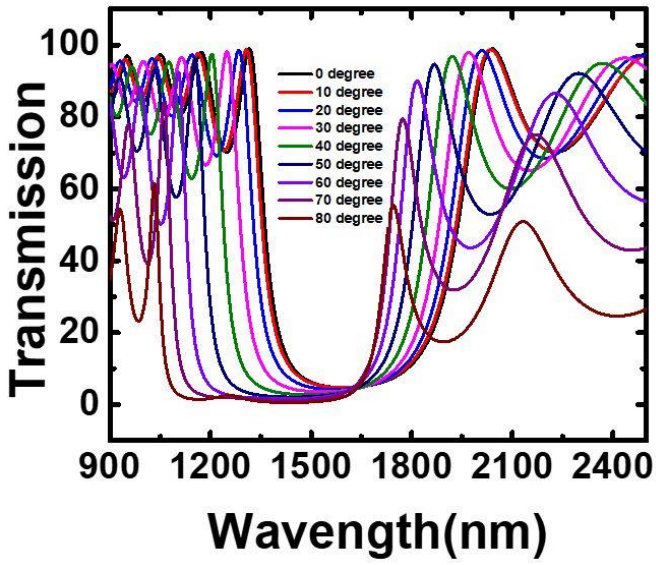

Figure 4.12 Showing the transfer matrix based transmission calculation showing red shift when incident angle deviated from normal.

The fabricated Bragg reflector have ~ 16 % transmission and it further reduces to ~ 0.07 % in stop band ranging from 1500 to 1800 nm after depositing VO_2 over it with the slight red shift of ~ 30 nm. The MATLAB simulation curves based on transfer matrix calculation method in Figure 4.12 above is showing the red shift when the incident light deviates from normal incident angle.

Thereofre, incorporating the W- VO_2 (M) thin film over flexible 1-D Photonic crytsal which is 100 % reflecting would lead to unit absorption enhacement around the room temperture itself, therefore, this strcture is very benfifical for regulating solar heat flux.

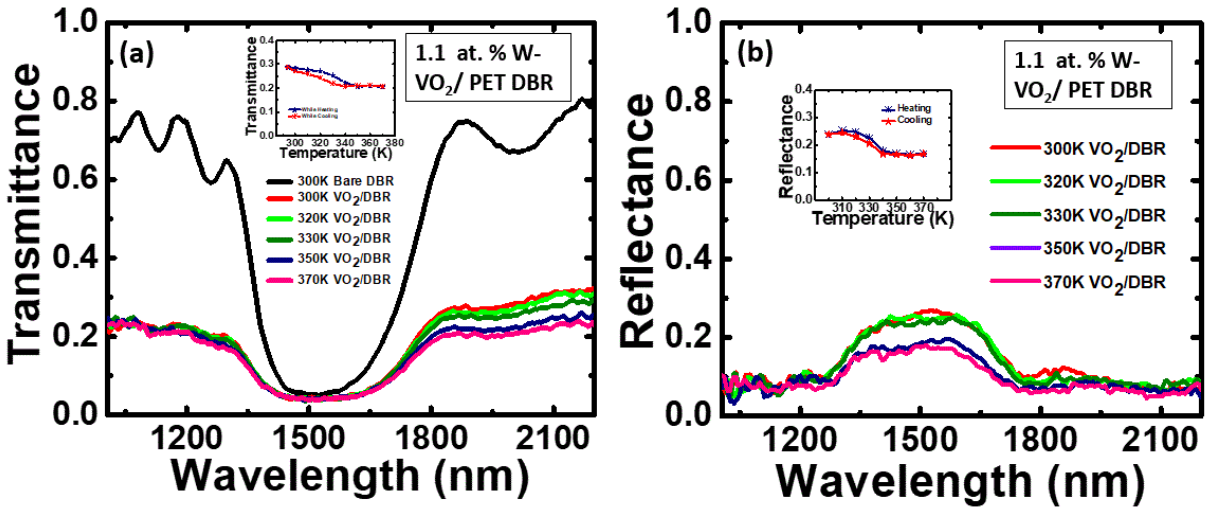

Figure 4.13 (a) showing the transmission spectra of W-VO_2 over flexible DBR tuned at 1515 nm having transmission ~ 95 % . with increase in temperature the transmission modulation i.e. ΔT ~ 7 %, above the wavelength of 1800 nm with the fractional change in transmission i.e. T_{300K}/T_{380K} ~ 1.4 which is calculated in the entire wavelength region, along with inset showing the hysteresis with width of 0.02 and (b) showing the corresponding reflectance of the W-VO_2/ DBR structure with increase in temperature along with inset showing the hysteresis width of ~ 0.02 around the temperature of 320K.

Figure 4.13 (a) and (b) representing the tranmsittance and reflectance curves of 1.1 at. % W - doped VO_2 incorporated with flexible DBR. The fabricated DBRs have 95 % reflection in the tuned wavlength region of around 1515nm (details of the fabrication process are given in section 4.2.4). The tuned bragg reflector has ~ 5 % tranmission in the stop band region and is fabrictaed by depositing seven stacks of SiO_2/Ta_2O_5 alternatly. By employing W – doped VO_2 over high quality Bragg Reflector, the optical tranmission goes to nearly zero in the stop band region raging from 1300 to 1800 nm at room temperture itself. Although the change may not be clearly visible but the fractional transmission change with increase in temperture is found to be T_{300K}/T_{380K} ~ 1.4 in the overall wavelength region. Figure 4.13 (a) Inset showing the hystersis of W – VO_2/ DBR structure which has a width of 0.02 at the transition tempeture of W-VO_2 i.e. at 310 K. Correspondingly, Figure 4.13 (b) displaying the reflection spectra of hybrid W-VO_2/DBR strcture with change in reflection can be seen signficantly in the stop band region of the DBR as the Bragg is highly

reflecting in nature around the stop band. Therfore, we observed the decrease in reflection from 26 % to 17 % as the temperture increases from 300 K to 370 K, but the relfection in the side band is quite low to observe any change in reflection with increae in tempeture but the fractional change in reflection in the entire wavelength region is found to be R_{380K}/R_{300K} ~ 1.5 which is same for side bands as well as for the stop band wavelength region.

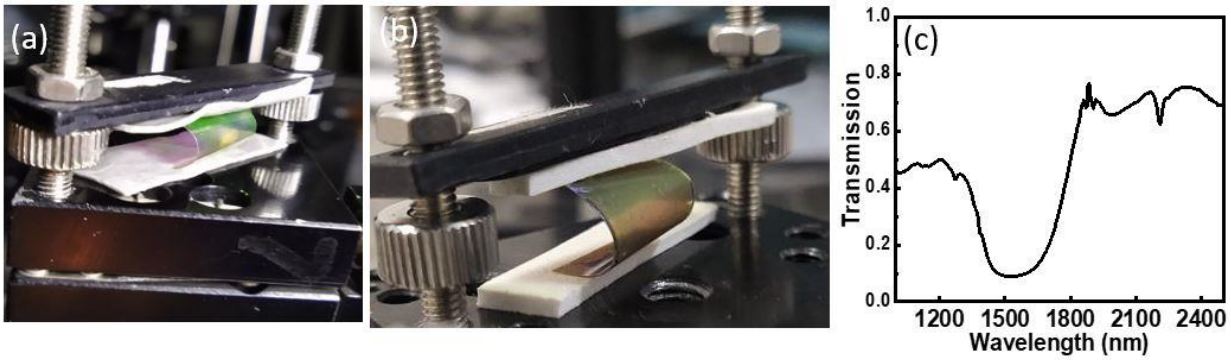

Figure 4.14 (a) showing the optical image of Bended DBR substrate (b) showing the optical image of bending VO_2 film over DBR substrate with (c) showing the optical transmission performance of the same.

Figure 4.14 (a) and (b) showing the W - doped VO_2/ DBR struture also subjected to compressive bending and the optical transmission spectra of bended strctures is also shown in Figure 4.14 (c). it is quite evident from the transmission spectra that film has retained its optical performance even after it is subjected to bending. Therefore, our modifed design of regulating outdoor temperature using W-doped VO_2/ DBR over flexible substate is proved to be quite robust and economical model for smart glass applications as an optical absorber.

4.6 Summary

In the summary of this work, we have proposed an economical and optimal design for smart glass application consisting of tungsten doped VO_2 nanostructure incorporated with 1D flexible Photonic crystal fabricated over PET substrate via magnetron sputtering of SiO_2/Ta_2O_5 in the IR region. We have experimentally demonstrated the nearly perfect extinction of IR with W-VO_2/DBR structure. High quality Bragg reflectors were fabricated with varying number of stacks over PET substrate as it offers flexibility. The transmission properties of both pure VO_2 and W-

doped VO_2 were studied on both Glass and PET substrate. Good crystallinity VO_2(M) and W-doped VO_2(M) were synthesized by the one step facile hydrothermal method. Structural transformation of both VO_2 and W- VO_2 were confirmed by High Temperature XRD and room temperature XRD to confirms that 1.1 at % is an optimal tungsten doping concentration. Thin films of VO_2 and W- VO_2 with PVP composite gives good optical transmission performance. Therefore, the transmission modulation of VO_2 thin films ~ 16 % and for W-doped VO_2, the optical transmission modulation is found to be ~ 7 % with change in temperature from 300 K to 370 K. 1D Photonic crystal fabricated with four stacks of SiO_2/Ta_2O_5 able to give ~ 40 % transmission, upon increasing the numbers of stacks to seven, the 1D Photonic crystal is able give ~ 5% transmission with stop band tuned at 1680 nm, therefore, tuning the number of stacks can control the transmission. On employing W – doped VO_2 over the high quality 1D Photonic crystal, the optical transmission of the W-VO_2/DBR structure almost vanishes (0.005 %) in the wavelength lies into stop band ranging from 1300 nm to 1800 nm even at the room temperature. Therefore, these structures are capable of regulating the solar radiation and thermal emissivity in the IR wavelength region. As these structures also offers flexibility therefore, this is an optimal design for retrofitting of the existing windows as well. Hence, we have proposed a hybrid architecture of W-VO_2 with flexible 1D Photonic crystal as a potential design for energy efficient and IR heat shielding smart glass applications.

4.7 References

[1] Zhang L, Xia F, Yao J, Zhu T, Xia H, Yang G, Liu B and Gao Y, Facile synthesis, formation mechanism and thermochromic properties of W-doped VO2(M) nanoparticles for smart window applications, *J. Mater. Chem. C*, **2020**, 8, 13396.

[2] Li W, Ji S, Li Y, Huang A, Luo H and Jin P, Synthesis of VO2 nanoparticles by a hydrothermal assisted homogeneous precipitation approach for thermochromic applications, *RSC Adv.*, **2014**, 4, 13026.

[3] Xu F, Cao X, Luo H and Jin P Recent advances in VO2-based thermochromic composites for smart windows J. Mater. Chem. C **2018** 6 1903–19.

[4] Yang J, Xu Z, Ye H, Xu X, Wu X and Wang J Performance analyses of building energy on phase transition processes of VO2 windows with an improved model *Appl. Energy* **2015** 159 502

[5] Goodenough, J. B. J. Solid State Chem. **1971**, 3, 490.

[6] Nag J, Hanglund R F, Synthesis of vanadium dioxide thin films and nanoparticles, *J. Phys.: Condens. Matter* **2008** , 20, 264016.

[7] Liu S, Fang H, Su Y, Hsieh J, Metal-insulator transition characteristics of Mo- and Mn-doped VO2 films fabricated by magnetron cosputtering technique, *Jpn. J. Appl. Phys.* **2014** 53, 063201.

[8] Warwick E A, Binions R, Advances in thermochromic vanadium dioxide films, *J. Mater. Chem. A.* 2014 2 3275–3292.

[9] Kiri P, Hyett G, Binions R, Solid state thermochromic materials, *Adv. Mater. Lett.* **2010** 2 86–105.

[10] Vostakola M F, Mirkazemi S M and Yekta B E, Structural, morphological, and optical properties of W-doped VO2 thin films prepared by sol-gel spin coating method, *Int. J. Appl. Ceram. Technol.*, **2019**, 16, 943.

[11] Li X F and Schaak R E, ZnO-templated synthesis and metal–insulator transition of VO2 nanostructures, *Chem.Mater*., **2019**, 31, 2088.

[12] Zou J, Xiao L, Zhu L and Chen X Y, One-step rapid hydrothermal synthesis of monoclinic VO2 nanoparticles with high precursors concentration, *J. Sol-Gel Sci. Technol*.,**2019**, 91,302.

[13] Chen L, Huang C, Xu G, Miao L, Shi J, Zhou J and Xiao X Synthesis of thermochromic W-Doped VO2 (M/R) nanopowders by a simple solution-based process *J. Nanomater*. **2012** 491051.

[14] Pan G, Yin J, Ji K, Li X, Cheng X, Jin H and Liu J, Synthesis and thermochromic property studies on W doped VO2 films fabricated by sol-gel method *Sci. Rep*. **2017** 7 6132.

[15] Tan X, Yao T, Long R, Sun Z, Feng Y, Cheng H, Yuan X, Zhang W, Liu Q, Wu C, Xie Y, Wei S. Unraveling metal-insulator transition mechanism of VO_2 triggered by tungsten doping. *Sci Rep*. **2012** 2 466.

[16] Park T H et al Thermo-adaptive block copolymer structural color electronics *Adv. Funct. Mater.* **2021** 31 2008548.

[17] Zhou D and Biswas R, Photonic crystal enhanced lighttrapping in thin film solar cells *J. Appl. Phys.* **2008** 103 093102.

[18] Curtin B, Biswa R and Dalal V, Photonic crystal based back reflectors for light management and enhanced absorption in amorphous silicon solar cells *Appl. Phys. Lett*. **2009** 95 231102.

[19] Zeng R, Chini A, Srinivasan R S and Jiang P Energy efficiency of smart windows made of photonic crystal *Int. J.Constr. Manag*. **2017** 17 100–12.

[20] Wang X, Gong Z, Dong K, Lou S, Slack J, Anders A and Yao J Tunable Bragg filters with a phase transition material defect layer *Optics Express* **2016** 24 20365.

[21] Lova P, Manfredi G and Comoretto D Advances in functional solution processed planar 1D photonic crystals *Adv. Funct. Mater*. **2018** 6 1800730.

[22] Zhang T, Yang J, Yu X, Li X, Yuan X, Zhao Y, Lyu D, Men Y, Zhang K and Ren L Handwritableonedimensional photonic crystals prepared from dendronizedbrush block copolymers *Polym. Chem*. **2019** 10 1519.

[23] Rashidi A, Hatef A and Namdar A On the enhancement of light absorption in vanadium dioxide/1D photonic crystal composite nanostructures *J. Phys. D: Appl. Phys*. **2018** 51 375102.

[24] Rashidi A, Entezar S R and Hatef A Tunable multispectral near-infrared absorption with a phase transition of VO2 nanoparticles hybridized with 1D photonic crystals *Nanotechnology* **2020** 31 335701.

[25] Singh D U, Bhoite O and Narayanan R Temperature tunable optical transmission using IR based 1D photonic crystals of VO2 nanostructures *J. Phys. D: Appl. Phys.* **2020** 53 245106.

[26] Wang N, Goh Q S, Lee P L, Magdassi S and Long Y Onestep hydrothermal synthesis of rare earth/W-codopedVO2 nanoparticles: reduced phase transition temperature and improved thermochromic properties *J. Alloys Compd*. **2017** 711 222.

[27] Yan W, Qu Y, Gupta T D,Darga A, Nguyên D T, Page A G, Rossi M, Ceriotti M and Sorin F Semiconducting nanowire-based optoelectronic fibers *Adv. Matter*. **2017** 29 1700681.

[28] Yan W, Burgos-Caminal A, Gupta T D, Moser J E and Sorin F Direct synthesis of selenium nanowire mesh on a solid substrate and insights into ultrafast photocarrier dynamics *J. Phys. Chem. C* **2018** 122 25134–41.

[29] Whittaker L, Wu T L, Patridge C J, Sambandamurthy G and Banerjee S Distinctive finite size effects on the phase diagram and metal–insulator transitions of tungsten-doped vanadium(IV) oxide *J. Mater. Chem.* **2011** 21 5580.

[30] Wu C, Zhang X, Dai J, Yang J, Wu Z, Wei S and Xie Y Direct hydrothermal synthesis of monoclinic VO2(M) single-domain nanorods on large scale displaying magnetocaloric effect *J. Mater. Chem.* **2011** 21 4509.

[31] Shao Z, Cao X, Luo H and Jin P Recent progress in the phase-transition mechanism and modulation of vanadium dioxide materials *NPG Asia Mater*. **2018** 10 581–605.

[32] Gomez-Heredia C L et al Measurement of the hysteretic thermal properties of W-doped and undopednanocrystallinepowders of VO2 *Sci. Rep*. **2019** 9 14687.

[33] Zeng W et al Size and crystallinity control of dispersed VO2 particles for modulation of metal–insulator transitiontemperature and hysteresis *CrystEngComm* **2019** 21 5749–56.

[34] Lova P Selective polymer distributed Bragg reflector vapor sensors *Polymers* **2018** 10 1161.

[35] Leem J W, Guan X Y and Yu J S Tunable distributed Bragg reflectors with wideangle and broadband high-reflectivity using nanoporous/dense titanium dioxide film stacks for visible wavelength applications *Opt. Express* **2014** 22 18519.

Chapter 5

1-D Photonic crystal hybridized Carbon dots for enhanced Photoluminescence

5.1 Introduction

Material based on carbon such as graphite, diamond, carbon nanotubes and graphene [1] are well known for their fluorescent properties. Carbon dot as such is all inclusive term which includes many materials composed of Nano sized carbon. Carbon material with size less than 10 nm are termed as carbon dots [2]. This material possesses intrinsic fluorescence property [3] and fluorescent properties can be manipulated by modification in their size and surface states [4]. In general fluorescent materials based on carbon has sp^2/sp^3 hybridized carbon [5], depending on the chemical treatment, nitrogen, oxygen and other functional groups get attached with the carbon core [6]. Carbon dots mainly includes Graphene Quantum Dots (GQDs) [7 – 10], Carbon Nano dots (CNDs) and Polymer assisted Carbon Dots (PDs) [11 – 13]. As shown in Figure 5.1. Below, Graphene based quantum dots composed of few layers of graphene with chemical groups attached to the edges of the dot. GQDs are anisotropic in nature with height of dots less than the lateral dimension. Carbon Nano dots are spherical in size. Carbon Nano dots and carbon quantum dots possess different origin of the PL as carbon Nano dots have no crystal lattices whereas carbon quantum dot has crystal lattices. At last polymer assisted carbon dots are composed of self-assembled carbon core attached with cross linked or aggregated polymers.

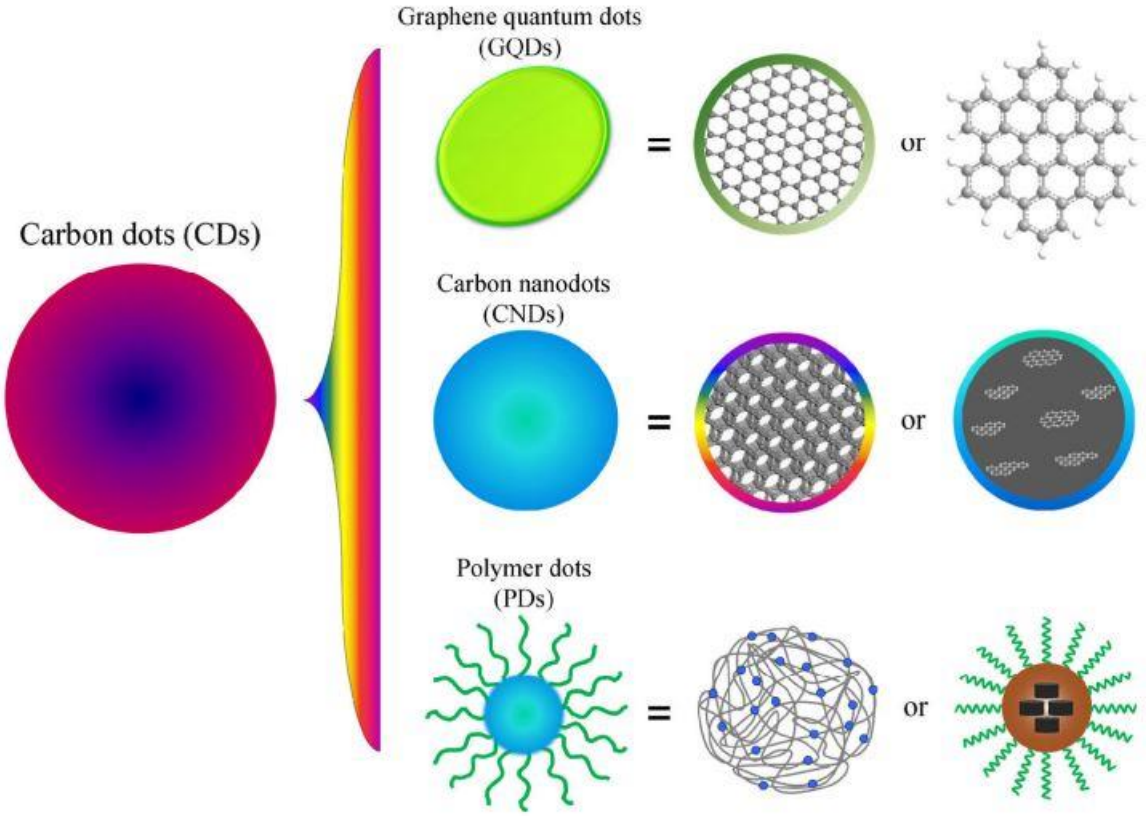

Figure 5.8 Showing the carbon dots categorized as graphene carbon dots, carbon Nano and quantum dots and polymer assisted carbon dots (above figure is adapted from ref [14]).

All these carbon dots have photoluminescence property (PL). Photoluminescence mechanism influenced by methods of chemical synthesis involved. Synthesis protocol determines the chemical surface groups attached and intrinsic structure which affects the Photoluminescence to a greater extent. In general, the synthesis of Carbon dots is based on two approaches. Namely top – down approach, in which large carbon structure breaks into smaller carbon parts via chemical treatments and ultrasonic treatments [15]. The other approach is bottom - up approach in which small carbon structures can be converted into desired size of carbon dots [16]. We will briefly discuss these two approaches in the subsequent sections.

5.1.1 Top – down approach

This approach based on the oxide cutting the carbon rich material source which includes carbon rods [17], carbon fibers [18] and graphene powders [19]. Carbon in these sources occupies sp^2 hybridized filled orbitals which is not able to give fluorescence due to large band gap. Therefore, to make them luminescent, their size and surface states were modified. The very common method used in oxide cutting is using concentrated oxidizing acids such as Nitric acid and mixture of Nitric acid and Sulfuric acid [20]. In this process the carbon source is cut up into small pieces, as Nitric and sulfuric acid consists of other chemical groups which get attached to the resulting carbon pieces known as Carbon graphene dots, carbon Nano – quantum dots. This approach includes the methods such as pyrolysis, carbonization, hydrothermal method, solvo - thermal method and reactive ion etching methods etc. However, the top – down approach requires expensive materials, harsh conditions and longer duration of reactions.

5.1.2 Bottom - up approach

This approach is a viable and an efficient method to synthesize carbon dots for extensive range of applications. In bottom up approach small molecules are dehydrated at the high temperatures. The molecules containing the chemical groups such as –OH, –C=O, $-NH_2$ and –COOH upon high temperature treatment can result into the formation of carbon dots. Due to high temperature it is difficult to control all parameters during the synthesis process, therefore, resulting carbon dots can have polydispersity. There are other various approaches to synthesize carbon dots using this approach such as by using microwaves [21], hydrothermal method [22], pyrolysing in concentrated acid [23] and so on. Therefore, bottom – up being comparatively easier and economical technique to obtain carbon dots from the small molecules. In this thesis as – synthesized carbon dots are obtained from bottom – up approach from small organic molecules.

In this work we have synthesized carbon dots with blue, green and red emissions via a solvothermal method. In the protocol, Solvents used in the reaction strenuously affects the surface states of the prepared carbon dots. For carbon dots novel applications Photoluminescence of the carbon dots and mechanism behind it is an important aspect of study. Here, the PL emission of carbon dots is not size dependent but rather the surface groups attached to the carbon core are the main reason of

PL emission. Generally, carbon dots synthesized by the solvothermal method possess a very strong PL emission. But obtained carbon dots from this method has broad PL emission as compared to carbon quantum dots. Broadening in PL Peak is due to the inhomogeneous structure of the carbon dots due to attachment of several other functional groups which creates different PL centers. Quantum yield is another aspect for the as – obtained carbon dots, which we will discuss in the brief in the subsequent section.

5.1.3 Quantum Yield

Any fluorescent material has a characteristic property known as quantum yield ϕ_F, which is defined as the ratio of emitted photons to the absorbed no. of photons at absorbing wavelength.

$$\phi = \frac{Number\ of\ photons\ emitted}{Number\ of\ photons\ absorbed}$$

In general, to measure the quantum yield two methods are employed, the absolute method and the relative method. In this thesis we used relative method to calculate the quantum yield of the carbon dots in liquid and in thin films of carbon dots over glass and over Bragg reflector. In the relative method, the quantum yield of the sample under study is calculated by comparing the fluorescence intensity of the sample with the fluorescence intensity of the reference. In this work, we have used Rhodamine 6G as a reference which has 0.95 value of quantum efficiency. The quantum yield is generally reported between 0 and 1 or as a percentage. Whereas, the absolute method requires integrating sphere which doesn't require any reference sample. In this work, we have used relative comparative method which is the most common method to calculate the quantum yield relying on the well-studied reference sample. The most important points to take care in comparative method is that the both sample under study and reference should have identical absorbance at the same excitation wavelength. Provided these conditions, the ratio of quantum yield and their integrated fluorescence intestines can be compared. By relative comparative method we can calculate the quantum yield by using reference of known quantum yield.

$$Qs = Qr\ \left(\frac{A_r}{A_s}\right)\left(\frac{E_s}{E_r}\right)\left(\frac{n_s}{n_r}\right)^2 \qquad \ldots\ldots\ldots\ldots\ldots\ldots\ldots\ldots\ldots\ldots (1)$$

Where, Q = quantum yield

n = refractive index of the solvent

A= Absorbance of the solution

E = Integrated fluorescence intensity

r = subscripts ‘r’ and ‘s’ for the reference and sample under study

5.1.4 Carbon dots and 1D Photonic crystal structure

Carbon being Fluorescence in nature holds great potential in extensive areas of research. It is an excellent candidate in energy saving applications in areas such as light emitting diodes, super capacitors, fuel cells, rechargeable batteries etc., as carbon dots have good luminesce efficiency, good stability and low toxicity [24]. Carbon dot based LEDs devices are an emerging area of research over the past few years because of their applications in liquid crystal display devices in our day today life. In general, LED devices are composed of expensive material ‘phosphors’ which is a rare earth material or toxic metal semiconductor quantum dots. Carbon dots can best candidate to replace these materials. Apart from these applications Carbon dots can be used as an active material in electroluminescent based devices and as a phosphor in LED applications. In carbon based LEDs, a transparent polymer such PVA [25] or transparent epoxy resins is treated as matrix material in which carbon dots are dispersed homogeneously. This step avoids the aggregation of carbon dots to prevent quenching of the PL. There are reports of white light emission from as - synthesized carbon dots via these approaches. These approaches become costly as they require multistep procedures and dispersion of carbon dots in such matrices suppress the PL of carbon dots and make the emission width broader. Other approaches are followed to reduce the self-quenching of carbon dots when integrated with solid state devices such using silane coupling agents [26]. However, to obtain white light emitting devices, having good luminous efficiency and high color rendering index are important parameters. Therefore, to obtain good performing white light emitting CDs with good quantum yield and narrow PL emission bandwidth requires more attention. Narrowing the fluorescence from the carbon dots using an efficient technique is highly required. Herein, in this work, we have proposed to enhance the photoluminescence of red carbon dots by incorporating dielectric based Bragg reflector with stop band tuned at the emission

wavelength and we have synthesized mixed carbon dots based white light emission incorporated with wide stop band metallic cavity structures.

As already discussed in chapter 1, Photonic crystal based structures due to their periodic nature and contrasting refractive indices, it creates photonic stop band gap (PSB) which can prohibit the light of certain frequency. It has been reported by Xuan et.al [27] that photonic crystal structure plays crucial role in modifying the fluorescent property. Jiang et. al [28] also proposed that Photonic crystal band gap structure can increase the fluorescence with the sensing enhanced applications with cocaine detection limit was increased to 10^{-16} mol L^{-1}. Whereas, Miguez et. al [29] proposed the cavity structure made up of dye – doped reflectors with fluorescence is sensitive towards the photonic environment. Hence, there are various studies based on photonic crystal which can alter the Luminesce emission of the carbon dots. As photonic crystals have the property of altering the emission by the change in light incident angle, but using the metal cavity structure which possess exceptionally large stop photonic band gap, make the carbon dot/ cavity structure immune to the incident angle variations. Therefore, in this chapter we have synthesized the tunable emission carbon dots with solvo – thermal method. We have studied the enhanced Photoluminescence emission property on glass substrate and on the dielectric based Bragg reflectors tuned in the visible region. Also, we have fabricated metallic cavities having large stop photonic stop band. We have optimized the mixture of carbon dots of different sizes to get a white light like emission and tried to modify its fluorescence properties. Finally, we will conclude this chapter with various possible opportunity for further experimentation.

5.2 Experimental Section

5.2.1 Chemical and material used

Urea (99 %, sigma Aldrich), Citric acid (99 %, sigma Aldrich), Dimethylformamide (DMF, 99.5 %, sigma Aldrich), ethanol (99.7%, sigma Aldrich), Sodium hydroxide (NaOH, sigma Aldrich), Poly(vinylalchol) (PVA, 99.5%, sigma Aldrich), de – ionized water, Silicone Dioxide (SiO_2) and tantalum oxide (Ta_2O_5) sputtering targets of 0.25-inch thickness and 2-inch diameter, Silver

Sputtering target of 0.25-inch thickness and 2-inch diameter with Pre cleaned microscope glass slides (J. Melvin Freed Brand) and Polyethylene terephthalate (PET sheet, 5 mm thickness).

5.2.2 Synthesis Protocol for carbon dot with Blue, Green and Red emission

In the modified synthesis protocol to obtain blue emitting carbon dots, 3 g of citric acid and 6 g of urea are added into 30 ml of aqueous solution and the solution is stirred continuously for 10 min at the temperature of 70 °C. once a clear transparent solution is obtained, it is transferred to 50 ml poly (tetrafluoroethylene) – lined autoclave. The autoclave is sealed tightly and kept in an oven at the temperature of 180 °C for 8 hours in the air atmosphere. After the reaction, the autoclave is allowed to cool completely to the room temperature on its own. A dark brown colored solution is obtained and is subsequently washed with the solution of ethanol and water. The ratio of ethanol and water is kept around 5:1. The carbon dot solution is washed and centrifuged at 8000 r min^{-1} for 10 minutes for three to four time. The washed precipitate was obtained and dispersed into ethanol to activate the blue emitting carbon dots. To synthesized green carbon dots, similar amount of solutes was added into 30 ml of ethanol solution and stirred for 10 min. at 70 °C and kept for 180 °C for 8 hrs. and subsequently washed with ethanol and dried in oven for 2 hrs. at 60°C. dispersed in ethanol to activate the carbon dots. And to obtain, red carbon dots, citric acid and urea were dissolved in DMF and kept at temperature of 180 °C for 8 hours in air ambient. A dark brown solution is obtained and washed with sodium hydroxide solution, NaOH solution is obtained by adding 1 g of NaOH in 20 ml of D. I water. The washed brown solute is obtained and dried at 60°C and dispersed into ethanol to activate the carbon dots.

5.2.3 Fabrication of Carbon dot with PVP composite thin film

To obtain the thin films of the carbon dots with PVP composite. 20 mg of PVP (10,000 Molecular weight) is mixed with 10 mg of carbon dots and 1 ml of ethanol was added and mixed thoroughly at 60 °C for few hours. The carbon dot and PVP composite is deposited over pre cleaned glass and PET substrate. The spin coated substrates were dried completely for 1 hr. at 60 °C.

5.3 Characterization of as-synthesized Carbon dots

Carbon dots synthesized by solvo - thermal method were characterized by the High resolution transmission electron microscopy (HRTEM) as shown in Figure 5.2

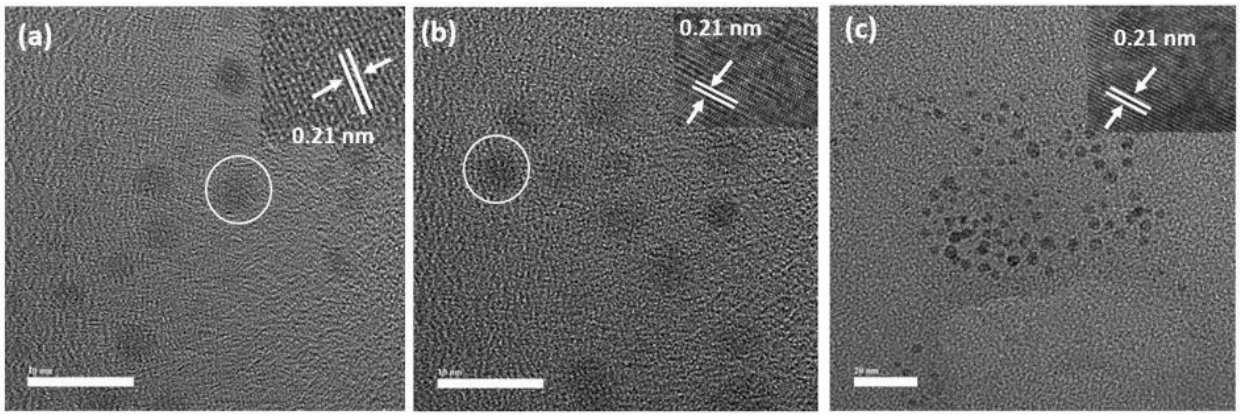

Figure 5.2 Showing the TEM images of blue, green and red carbon dots with inset showing the High resolution TEM images.

TEM images of as –synthesized blue, green and red carbon dots governing the morphologies. As shown in Figure 5.2 (a) – (c), high resolution TEM images showing well resolved lattice fringes. The inter-planar spacing of HR – TEM images of the blue, green and red carbon dots is nearly 0.21 nm which is more or less close to the inter – planar spacing of the carbon graphite with lattice plane associate to dot is (100). TEM images clearly indicating the size of dots from 5 – 10 nm respectively. As all carbon dots has similar sizes, it indicates that emission of different wavelengths is not due to the quantum size effect. But rather it is due to the attachment of functional groups to the carbon core during synthesis. Figure 5.3 showing the Raman spectra of the as – synthesized red carbon dots.

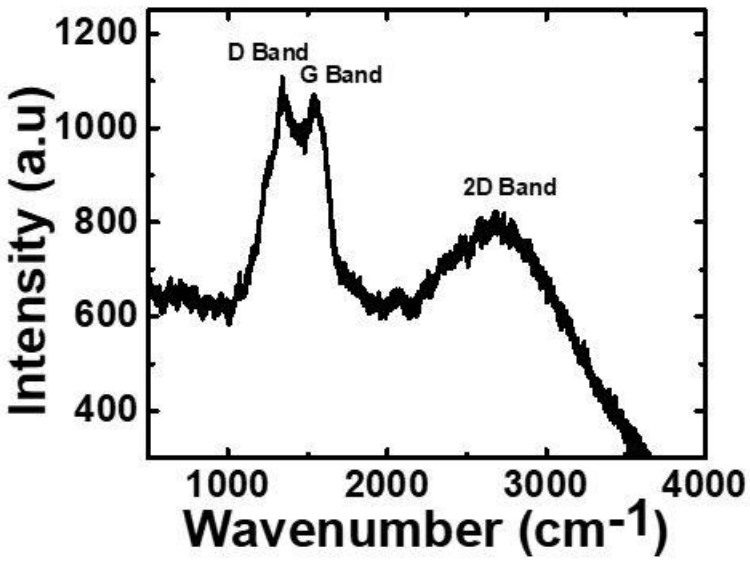

Figure 5.3 Showing the Raman spectra of the as –synthesized red carbon dot.

As shown in Figure 5.3, the Raman spectra of as- synthesized red carbon dots are recorded in the region of 1200 – 1800 cm^{-1}. There two peaks associated with D band and the G band in range of 1100 – 1600 cm^{-1}. The origin of the G band is from sp^2 hybridized carbon of the graphite and D Band originates from the disorder in the structure of the carbon dots. And the 2D Band has broad Raman peak at and around 2700 cm^{-1} which is associated with the aromatic carbon of the graphite [30]. Therefore, the Raman spectra clearly indicates the luminescence of the as – synthesized carbon dots is due to the existence of graphite core and other surface functional groups together. As reported in [31, 32], the FTIR spectra also confirmed the attachment of other functional groups such as O – H, N – H which makes these dots soluble in polar solvents. The as – synthesized carbon dots are characterized optically as shown in the Figure 5.4 (a) in which blue, green and red carbon dots activated with polar solvent such as ethanol, are excited under UV light and emission from the respective dots were studied. Therefore, Figure 5.4 demonstrating the optical picture of light emitted from the carbon dot with naked eye under UV excitation.

Figure 5.4 Demonstrating the optically excited blue, green and red carbon dots dispersed into ethanol under UV excitation.

Different absorption features of blue, green and red carbon dots are observed in the UV-VIS absorption spectra as shown in the Figure 5.5.

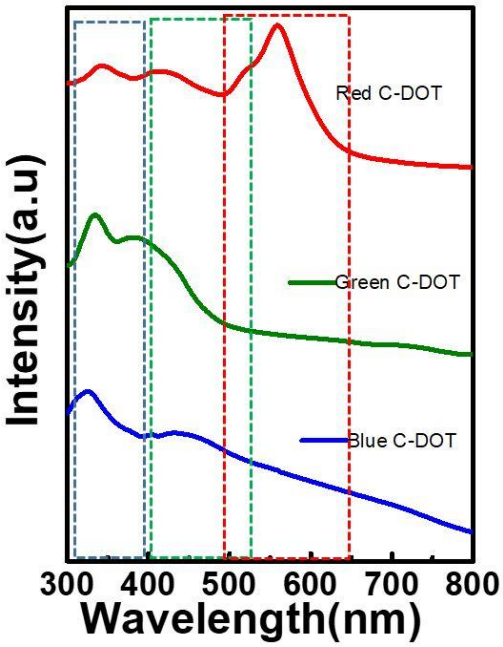

Figure 5.5 Showing the UV –VIS absorption spectra of the blue, green and red carbon dots depicting distinct features.

As shown in the absorption spectra for blue carbon dots, strong absorption peaks were observed at 260 nm and 350 nm wavelength, these peaks are associated with the absorption occurs due to the intrinsic transition of $\pi - \pi^*$ and $n - \pi^*$ due to carbon core. In the absorption spectra of green carbon dots, as that of the blue carbon dots, intrinsic band gaps appear, along with these shoulder band appears at and around 440 nm wavelength which mainly attributes to the absorption occurs due to C = O chemical group attached to the surface of the carbon cores. As in case of the red

carbon dots, there is an additional strong absorption at the wavelength of 550 nm which is attributed to the C = N chemical group attached to the surface of the carbon dots. From the absorption measurement for red carbon dots the intensity of absorption for C = N is higher than the absorption of the intrinsic and C = O chemical groups of the carbon dots. These results evidently suggest that solvents such as ethanol and DMF which modified the surface states of the carbon dots used during the solvo - thermal method are the reason of long range emission in the carbon dots. Figure 5.6 showing the Photoluminescence spectra of the as- synthesized Blue, green and red carbon dots.

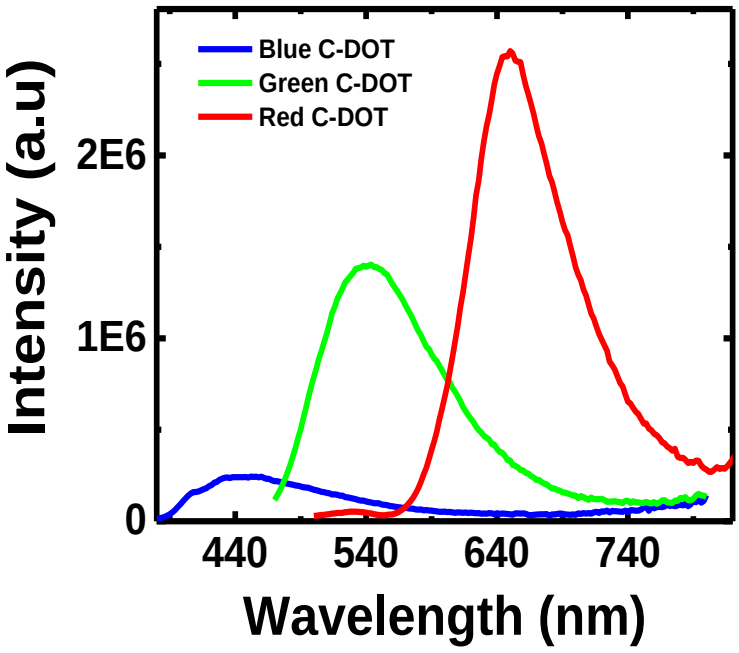

Figure 5.6 Showing the Photoluminescence of the blue, green and red carbon dots with different excitations.

Figure 5.6 demonstrating the Photoluminescence spectra of blue, green and red carbon dots composite thin film. Due to the aggregation of carbon dots re-absorption of photons can take place which leads to, self-quenching hence it can decrease the photoluminescence of the carbon dots. To prevent the self-quenching carbon dots films were obtained by mixing appropriate amount of carbon dots with PVA and ethanol. The surface groups such as carboxyl and amide attached to the surface of the carbon dots forms hydrogen bonds with hydroxyl group of the PVA. This makes the

Carbon dots dispersed well with PVA molecules hence it prevents the aggregation of the carbon dot particles while making the carbon dot thin films. Figure 5. showing the Photoluminescence spectra of the blue, green and red carbon dots under different excitations, blue dots were excited with 360 nm, green carbon dots are excited with 450 nm and red carbon dots are excited with 488 nm. respectively and the spectral shape along with the emission wavelengths are same for the solution and the composite films of the carbon dots. Therefore, this indicated that the PVP/Carbon dot composite prevented the self-quenching of carbon dots. Taking the advantage of the composite stability, carbon dots/PVP composite of blue, green and red dots are mixed with appropriate ratios and optimized ratio of green and red carbon dot mixed together giving a broad wavelength emission which can be excited with a single excitation. The Figure 5.7 showing the broad wavelength emitting green and red carbon dots/PVP composite films PL.

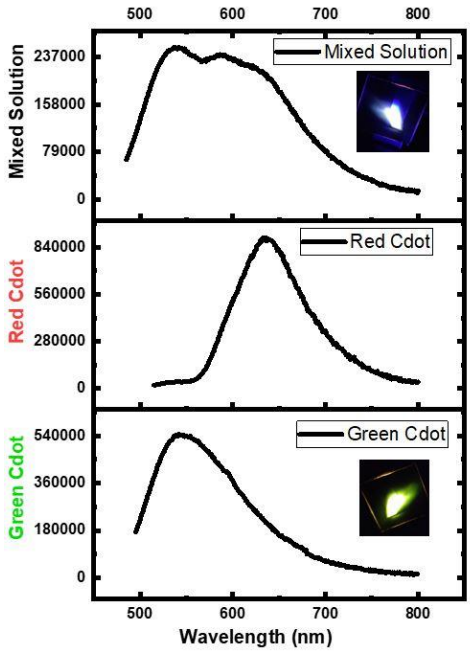

Figure 5.7 Showing the Photoluminescence of green, red and mixture of green – red carbon dots with PVA along with inset showing the optical image of the light emission from the films.

In this study, we have synthesized red, green and blue emission carbon dots with facile solvo - thermal method and upon mixing the red and green carbon dots in appropriate amount with a suitable polymer matrix gives a broad band emission with single excitation. Now this broad band emission can be enhanced significantly using a large stop band metal cavity structure. These mixed

carbons dot thin films showing the emission from the ensemble of carbon dots therefore, carbon dot s with metallic cavities and dielectric stacks over flexible PET substrate holds great potential in enhancing monochromaticity and increased quantum yield. Figure 5.8 (b) showing the photoluminescence enhancement over metallic cavity with metallic cavity reflection spectra shown in Figure 5.8 (a).

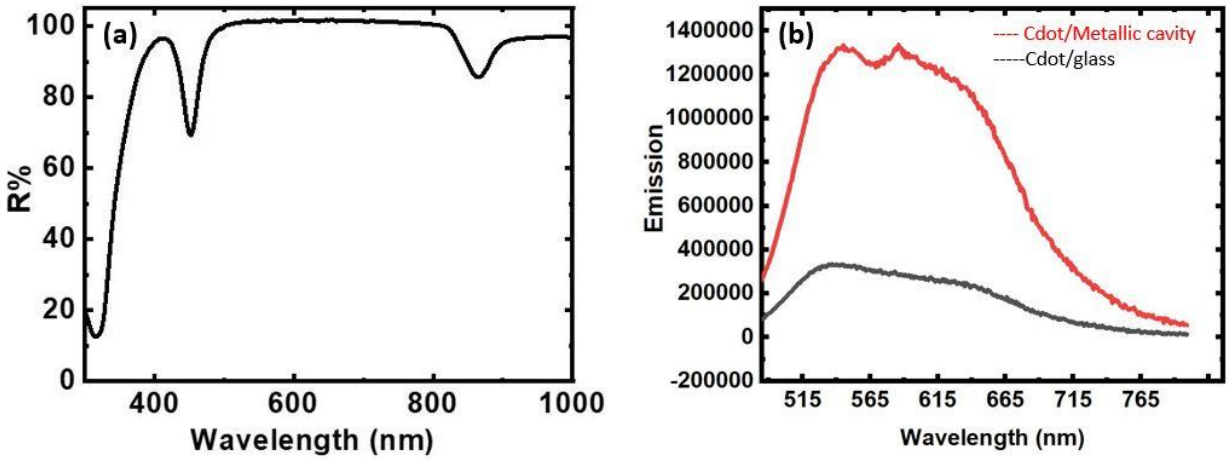

Figure 5.8 (a) Showing the reflection spectra of the metal cavity fabricated with Ag (10nm)/ SiO_2 (400nm) / Ag (10nm) and (b) showing the mixed carbon dots (1:4) of red and green broad emission is enhanced significantly over metallic cavity.

Figure 5.8 (a) showing the metal cavity structure fabricated with Ag (10nm) both sides with 400 nm of SiO_2 sand witched in between, having the reflection band ranging from ~ 500 nm to ~ 900 nm. i.e., having the stop band of 400 nm which quite broad as compared to the alternate dielectric stacks. Figure 5.8 (b) showing the enhancement of mixed carbon dots over metallic cavity structure. It is quite evident from the above data there is nearly six times enhancement in fluorescence of the mixed carbon dots when placed over the metallic cavity as compared to the glass substrate. Apart from the mixed carbon dots over metallic structure, we have employed red carbon dots over dielectric Bragg reflector structure, as Bragg reflector has to be emitted with light at normal incident, which makes it difficult to characterize the sample in the spectrometer. Therefore, we have implemented red carbon dots with emission wavelength of 633 nm over dielectric stack and calculated the enhanced quantum yield ratio, along with it we have performed intensity dependent PL enhancement studies to see the effect in broadening of the red carbon dots over DBR stop tuned at 633 nm. Due to limited excitation sources we couldn't perform the similar

experiments on blue and green emitting carbon dots. Therefore, Figure 5.9 (a) below showing the Bragg reflector tuned at 633 nm along with the optical image of the DBR in right. Figure 5.9 (b) showing the absorption of red carbon dots on glass with optical image shown in inset and Figure 5.9 (c) showing the absorption of red carbon dots over DBR along with optical image of the substrate in the inset.

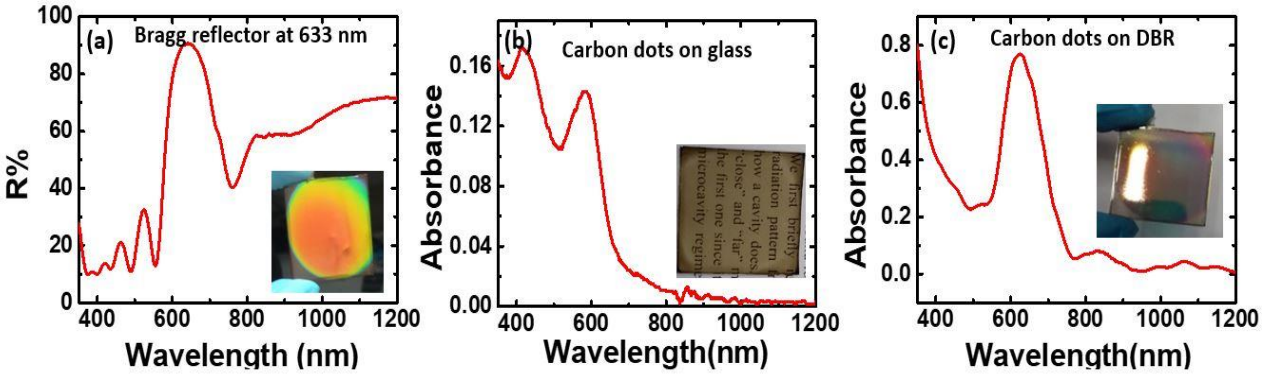

Figure 5.9 (a) Showing the Bragg reflector tuned at 633 nm along with optical image of DBR in inset (b) showing the absorption spectra of carbon dots over glass substrate along with optical image in the inset and (c) showing the absorption spectra of the carbon dots over DBR tuned at 633nm along with optical image shown in the inset.

From figure 5.9 (b) and (c) the absorption of carbon dots over DBR is also enhanced as compared to the carbon dots over the glass. Further studies have been carried out to compare the quantum yield ratios of carbon dots over glass than the carbon dots over DBR. Figure 5.10 showing the Photoluminescence measurement done with excitation of 488 nm with the set up described on chapter 2 of experimental section.

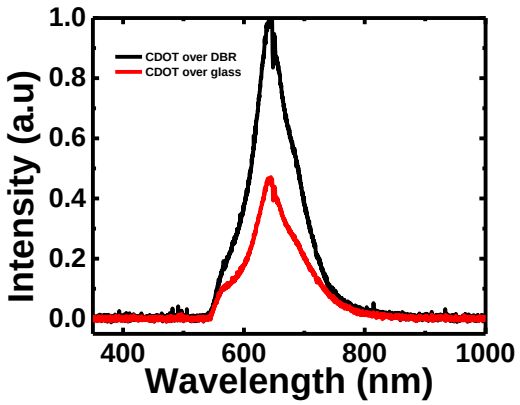

Figure 5.10 Showing the Photoluminescence of Red carbon dots over Bragg reflector and over glass substrate.

From the figure 5.10, the photoluminescence of red carbon with emission wavelength around 650 nm enhanced nearly four times as compared to the photoluminescence at the glass substrate. Following the quantum yield ratio formula above in equation (1). The ratio of quantum yields of carbon dots over DBR with quantum yield over glass is calculated as,

$$\frac{\varphi_s}{\varphi R} = \frac{I_s}{I_r} \times \frac{A_r}{A_s} \times \frac{ns^2}{nr^2}$$

‘s’ subscript representing the sample quantum yield and ‘r’ subscript reference quantum yield.

$$\frac{\varphi_{cdot+DBR}}{\varphi_{ref}} = \frac{I_{cdot+DBR}}{I_{Ref}} \times \frac{A_{ref}}{A_{cdot+DBR}} \times \frac{{n_{dmso}}^2}{{n_{ref}}^2} \quad \ldots\ldots\ldots\ldots\ldots \quad (1)$$

$$\frac{\varphi_{cdot}}{\varphi_{ref}} = \frac{I_{cdot}}{I_{ref}} \times \frac{A_{ref}}{A_{cdot+glasss}} \times \frac{{n_{dmso}}^2}{{n_{ref}}^2} \quad \ldots\ldots\ldots\ldots\ldots\ldots\ldots (2)$$

Upon comparing the ratio of the both equations,

$$\frac{\varphi_{cdot+DBR}}{\varphi_{cdot}} = \frac{I_{cdot+dbr}}{I_{cdot}} \times \frac{A_{cdot}}{A_{dbr+cdot}} \quad \ldots\ldots\ldots\ldots\ldots\ldots \quad (3)$$

Substituting values from the above data gives the value as,

$$\frac{\varphi_{cdot+DBR}}{\varphi_{cdot}} = 4.16$$

Therefore, the quantum yield of the carbon dots over DBR enhanced four times as compared to the quantum yield over the glass. Further experiments were carried to see the effect on the Full width half maxima or photoluminescence peak broadening with the function of laser intensity.

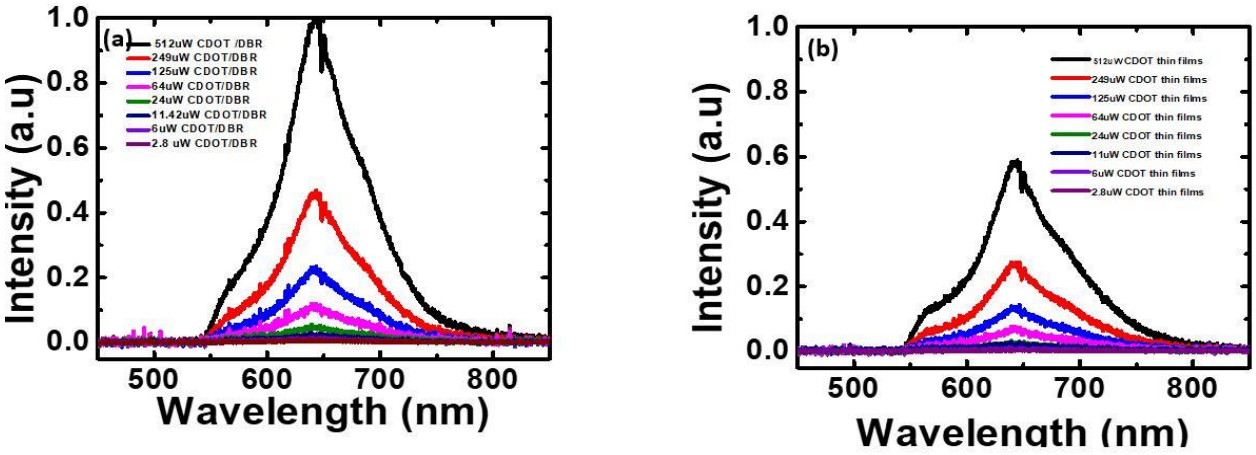

Figure 5.11 (a) Showing the change in photoluminescence with change in laser intensity over DBR and (b) representing the change in photoluminescence with change in intensity over glass.

Figure 5.11 above are representing the change in photoluminescence intensity with increase in laser intensity on carbon dots with DBR and carbon dots with glass. From the above data peak intensity with laser power and then FWHM (full width half maxima) is calculated. There is reduction in FWHM in CDOT/DBR than CDOT/glass.

5.4 Conclusion and Future perspective

In Summary, we have synthesized carbon dots of tuned emission by modified solvo - thermal method by changing the solvents during the hydrothermal reactions. To synthesize blue, green and red emitting carbon dots, hydrothermal reactions were carried out at 200 ^{o}C for 8 hours. D.I water is used as a solvent for the synthesizing blue emitting carbon dots, to synthesizing green emitting carbon dots, ethanol is used as a solvent and to synthesizing red emitting carbon dots, solutes were dissolved in DMF before hydrothermal reaction. TEM characterization suggested the size of all the carbon dots are nearly same which is around 10 – 15 nm. Raman spectral

characterization of the red emitting carbon dots gives direct indication that the intrinsic states and attachment of C=O/C=N chemical groups to the carbon core causing the emission of carbon dots in red, green and blue region due to absorption of light in various states. We have further synthesized carbon dots with broad emission by mixing them thoroughly in different ratios with PVP composite. for broad emission the optimized mixing ratio is such, green carbon dots with red carbon dots in the ratio of 4:1. Metal cavity structure fabricated as Ag (10nm) / SiO_2 (400nm) /Ag (10nm). 10 nm Ag is deposited over glass and over PET substrate with thermal vapor deposition and SiO_2 is deposited with magnetron sputtering. To prevent the damaging of Ag metal layer deposited via thermal vapor deposition, SiO_2 is deposited at a very slow rate. Optimized mixture of carbon dots is implemented over metal cavity structure and significant enhancement is observed. Moreover, we have studied the effect of red carbon emission when implemented on dielectric Bragg reflector by illuminating with 488 nm laser. Photoluminescence quantum yield of red carbon over Bragg reflector is observed to be four times as compared to the photoluminescence of red carbon dot over glass substrate. Laser intensity dependent photoluminescence measurement is done on both cdot with DBR substrate and on cdot with glass substrate. Full width half maxima plots with laser intensity were also calculated. This work provides enough results to show that carbon dots hybridized with metal cavity structure and dielectric structure holds great potential in optoelectronic devices.

5.5 References

[1] Liu J, Li R, and Yang B, Carbon Dots: A New Type of Carbon-Based Nanomaterial with Wide Applications, *ACS Cent. Sci*. **2020**, 6, 2179−2195.

[2] Wang Y, Hu A. Carbon quantum dots: synthesis, properties and applications. *J Mater Chem C*. **2014** 2 6921–3.

[3] S. Zhu, Y. Song, J. Shao, X. Zhao, B. Yang, Non-Conjugated Polymer Dots with Crosslink-Enhanced Emission in the Absence of Fluorophore Units, *Angew. Chem., Int. Ed*. **2015**, 54, 14626.

[4] Dong Y, Wang R, Li H, Shao J, Chi Y, Lin X, Chen G. Polyamine-functionalized carbon quantum dots for chemical sensing. *Anal Chem*. **2012** 84 (14) 6220–4.

[5] Baker, S. N.; Baker, G. A. Luminescent carbon nanodots: Emergent nanolights. *Angew. Chem. Int. Ed*. **2010**, 49, 6726– 6744.

[6] Li, H. T.; Kang, Z. H.; Liu, Y.; Lee, S.-T. Carbon nanodots: Synthesis, properties and applications. *J. Mater. Chem*. **2012**, 22, 24230–24253.

[7] Zhu, S. J.; Tang, S. J.; Zhang, J. H.; Yang, B. Control the size and surface chemistry of graphene for the rising fluorescent materials. *Chem. Commun***. 2012**, 48, 4527–4539.

[8] Shen, J. H.; Zhu, Y. H.; Yang, X. L.; Li, C. Z. Graphene quantum dots: emergent nanolights for bioimaging, sensors, catalysis and photovoltaic devices. *Chem. Commun*. **2012**, 48, 3686–3699.

[9] Zhang, Z. P.; Zhang, J.; Chen, N.; Qu, L. T. Graphene quantum dots: An emerging material for energy-related applications and beyond. *Energy Environ. Sci*. **2012**, 5, 8869–8890.

[10] Zhou, X. J.; Guo, S. W.; Zhang, J. Y. Solution-processable graphene quantum dots. *ChemPhysChem* **2013**, 14, 2627– 2640.

[11] Liu, S.; Tian, J. Q.; Wang, L.; Zhang, Y. W.; Qin, X. Y.; Luo, Y. L.; Asiri, A. M.; Al-Youbi, A. O.; Sun, X. P. Hydrothermal treatment of grass: A low-cost, green route to nitrogen-doped, carbon-rich, photoluminescent polymer nanodots as an effective fluorescent sensing platform for label-free detection of Cu(II) ions. *Adv. Mater*. **2012**, 24, 2037–2041.

[12] Qiao, Z.-A.; Huo, Q. S.; Chi, M. F.; Veith, G. M.; Binder, A. J.; Dai, S. A "ship-in-a-bottle" approach to synthesis of polymer dots@silica or polymer dots@carbon core-shell nanospheres. *Adv. Mater*. **2012**, 24, 6017–6021.

[13] Zhu, S. J.; Zhang, J. H; Wang, L.; Song, Y. B.; Zhang, G. Y.; Wang, H. Y.; Yang, B. A general route to make nonconjugated linear polymers luminescent. *Chem. Commun*. **2012**, 48, 10889–10891.

[14] Zhu S, Song Y, Zhao X, Shao J, Zhang J, and Yang B, The photoluminescence mechanism in carbon dots (graphene quantum dots, carbon nanodots, and polymer dots): Current state and future perspective, *Nano Research* **2015**, 8(2): 355–381.

[15] Feng, X. L.; Wu, J. S.; Ai, M.; Pisula, W.; Zhi, L. J.; Rabe, J. P.; Müllen, K. Triangle-shaped polycyclic aromatic hydrocarbons. *Angew. Chem. Int. Ed*. **2007**, 46, 3033–3036.

[16] Yan, X.; Cui, X.; Li, L.-S. Synthesis of large, stable colloidal graphene quantum dots with tunable size. *J. Am. Chem. Soc*. **2010**, 132, 5944–5945.

[17] Li, H. T.; He, X. D.; Kang, Z. H.; Huang, H.; Liu, Y.; Liu, J. L.; Lian, S. Y.; Tsang, C. H.; Yang, X. B.; Lee, S.-T. Water-soluble fluorescent carbon quantum dots and photocatalyst design. *Angew. Chem. Int. Ed.* **2010,** 49, 4430–4434.

[18] Peng, J.; Gao, W.; Gupta, B. K.; Liu, Z.; Romero-Aburto, R.; Ge, L. H.; Song, L. H.; Alemany, L. B.; Zhan, X. B.; Gao, G. H. et al. Graphene quantum dots derived from carbon fibers. *Nano Lett.* **2012**, 12, 844–849.

[19] Qiao, Z.-A.; Wang, Y. F.; Gao, Y.; Li, H. W.; Dai, T. Y.; Liu, Y. L.; Huo, Q. S. Commercially activated carbon as the source for producing multicolor photoluminescent carbon dots by chemical oxidation. *Chem. Commun*. **2010**, 46, 8812–8814.

[20] Tao, H. Q.; Yang, K.; Ma, Z.; Wan, J. M.; Zhang, Y. J.; Kang, Z. H.; Liu, Z. In vivo NIR fluorescence imaging, biodistribution, and toxicology of photoluminescent carbon dots produced from carbon nanotubes and graphite. *Small* **2012**, 8, 281–290.

[21] Yang, Z.-C.; Wang, M.; Yong, A. M.; Wong, S. Y.; Zhang, X.-H.; Tan, H.; Chang, A. Y.; Li, X.; Wang, J. Intrinsically fluorescent carbon dots with tunable emission derived from

hydrothermal treatment of glucose in the presence of monopotassium phosphate. *Chem. Commun*. **2011**, 47, 11615–11617.

[22] Zhu, H.; Wang, X. L.; Li, Y. L.; Wang, Z. J.; Yang, F.; Yang, X. R. Microwave synthesis of fluorescent carbon nanoparticles with electrochemiluminescence properties. *Chem. Commun*. **2009**, 5118–5120.

[23] Peng H, Travas-Sejdic J, Simple aqueous solution route to luminescent carbogenic dots from carbohydrates. *Chem. Mater***. 2009**, 21, 5563–5565.

[24] Liu J, Lu S, Tang Q, Zhang K, Yu W, Sun H, Yang B, One-step hydrothermal synthesis of photoluminescent carbon nanodots with selective antibacterial activity against Porphyromonas gingivalis, *Nanoscale* **2017**, 9, 7135.

[25] Feng T, Zeng Q, Lu S, Yan X, Liu J, Tao S, Yang M, Yang B, Color-Tunable Carbon Dots Possessing Solid-State Emission for Full-Color Light-Emitting Diodes Applications. *ACS Photonics* **2018**, 5, 502−510.

[26] He, J.; He, Y.; Chen, Y.; Lei, B.; Zhuang, J.; Xiao, Y.; Liang, Y.; Zheng, M.; Zhang, H.; Liu, Y. Solid-State Carbon Dots with Red Fluorescence and Efficient Construction of Dual-Fluorescence Morphologies. *Small* **2017**, 13, 1700075.

[27] Baig N, Kammakakam I and Falath W, A review of synthesis methods, properties, recent progress, and challenges, *Nanomaterials*, **2021**, 2, 1821-1871.

[28] J. Hou, H. Zhang, Q. Yang, M. Li, Y. Song, L. Jiang, Bio-inspired photonic-crystal microchip for fluorescent ultratrace detection, *Angew. Chem., Int. Ed*. **2014,** 53, 5791.

[29] Jimenez-Solano A, Galisteo-Lopez J F, Miguez H, Nanoemitters: Fine Tuning the Emission Properties of Nanoemitters in Multilayered Structures by Deterministic Control of their Local Photonic Environment *Small* **2015**, 11, 2727.

[30] Chen D, Wu W, Yuan Y, Zhou Y, Wan Z and Huang P Intense multi-state visible absorption and full-color luminescence of nitrogen-doped carbon quantum dots for blue-light-excitable solid-state-lighting *J. Mater. Chem. C* **2016** 4 9027–35.

[31] Qu S, Zhou D, Li D, Ji W, Jing P, Han D, Liu L, Zeng H and Shen D Toward efficient orange emissive carbon nanodots through conjugated sp2 -domain controlling and surface charges engineering *Adv. Mater***. 2016** 28 3516–21.

[32] Reckmeier C J, Schneider J, Susha A S and Rogach A L Luminescent colloidal carbon dots: optical properties and effects of doping *Opt. Express* **2016** 24 A312–40.

Chapter 6

Conclusions and Future Outlook

6.1 Conclusion

Regulating electromagnetic wave transmission and reflection in smart window applications attracted lot of attention in building energy saving applications. As building are the major consumer of energy, implementing smart glass designs will contribute in minimizing the energy consumption significantly. As heating, ventilation and air conditioning of buildings accounts in significant energy consumption. With Employing smart windows only regulate amount of ultraviolet and infrared light can enter into the buildings. By controlling the ultraviolet radiation will reduce the cooling expenditure and can be used vice-versa in winter days. Therefore, improving the designs of building fenestrations for energy efficiency are of extreme importance. Although there are various chromogenic materials which are used for smart window applications such as Photochromic, electrochromic and thermochroic to conserve the energy but all these materials coating require additional input of electricity or heat to function.

Photonic crystal can greatly control the electromagnetic waves due to variation periodicity. Therefore, implementing the tunable Photonic crystal with thermochromics materials can regulate the special propagation of electromagnetic waves. This smart window design due to photonic crystal can statically regulate the visible light and with thermochromic material it can dynamically regulate the infra-red light to ~ 100% efficiency. Here in this thesis we have implemented tunable 1D Photonic crystals with Vanadium Dioxide thermochromic material and studied their optical properties. ***Chapter 1*** gives the introductory details of Photonic crystal for smart windows and VO2 and its polymorphs. In ***Chapter 2*** we have described the various characterization techniques to study the structural and optical properties of 1D Photonic crystal and thermochromic materials. In ***Chapter 3*** we have presented 1D Photonic crystal based smart window design incorporated with Vanadium Dioxide. We have fabricated 1D photonic crystal tuned in infra-red region and

synthesized VO_2 nanostructures of different crystallinity. We have studied the effect of different stacks of Photonic crystal with VO_2 performance with increase in temperature. Moreover, we have employed Moderately crystalline VO_2 over ~ 100 % reflecting 1D Photonic crystal and observed the transmission reaches to ~ 0.6 % with temperature increased to 380 K. In ***chapter 4***, we have tailored the transition temperature of VO_2 nanostructure near to room temperature by doping appropriate amount of tungsten atoms. 1.1 at. % is the optimal dopant for VO_2 nanostructures. and W- doped VO_2 nanostructure are employed on flexible 1D Photonic crystal fabricated over PET substrate. 1-D Photonic crystals fabricated over PET with seven stack of SiO_2/Ta_2O_5 can achieve ~ 5 % transmission in tuned stop band and with increase in temperature, transmission almost vanish to 0.05 value. Therefore, reflection and transmission of W-doped VO_2 over flexible 1-D Photonic crystal decrease substantiality in Photonic crystal stop band with increase in temperature. Apart from this, W-VO_2/ Photonic crystal structure also subjected to compressive bending. Therefore, integration of these materials with Photonic crystal can regulate the transmission and reflection in desired manner.

Photonic crystals are great candidate for manipulating the light by the virtue of photonic band gaps. In ***Chapter 5***, we have tried to employ the carbon dots on dielectric Bragg reflectors as well as metal cavity structures. Carbon dots possess excellent fluorescence properties and is an excellent candidate for energy saving applications. Apart from being environmental friendly carbon dots shows good optical tunability. Here we have synthesized the blue, green and red carbon dots using modified facile solvo - thermal method. By optimally mixing the green and red carbon dots in the ratio of 4:1, a broad band light emitting carbon dots with PVP composite is obtained. We have further employed the red carbon dots and broad emitting light over dielectric stack and metal cavity and observed a significant Photoluminescence enhancement. These structure architectures found to have great potential in color rendering devices. However, Further experiments are necessary to gain a complete understanding.

6.2 Future Outlook

Photonic crystal based smart windows not only enhance the optical performance, due to their unique properties but will also broaden their applications in various fields. The smart window industry has the biggest challenge of durability of these designs and large area feasibility of these architectures. Incorporation of such functional materials in 2D and 3D Photonic crystal structures will allow various functionalities of smart windows with improved optical properties. Fabricating organic – inorganic Photonic crystals structures will be multi-responsive and can be further studied for advanced smart window design. Apart from improving the optical performances, the aesthetic needs for smart glasses is of equal importance. Therefore, Integrating Photonic crystal with structural color will enhance the aesthetic appeal of smart windows. Moreover, fabricating Photonic crystals which are amorphous in nature to regulate transmission and reflection by with no incident angle dependency while tuning the photonic band gap will favorable design for smart windows.

Furthermore, Improvement in thermochromic properties of functional materials for implementing with Photonic crystal structures will advance the Photonic crystal based energy efficient devices. Rather than conventional materials like VO_2 and carbon dots, Photonic crystal structure can be embedded with emerging materials like Perovskite and hydrogels for improved and better energy efficient structures for the application of high resolution bio imaging and sensors. Apart from smart windows Photonic crystal structures helps in selecting solar radiation and can be integrated with suitable absorbers for thermal Photovoltaic applications. As PCs provides robust optical confinement, therefore this structures are not only restricted to Smart windows but also highly desirable in Photonic crystal based low threshold lasers and various other applications.

APPENDIX

The research work presented in this are inspired with following publications.

1. Dipti umed singh*, omkar bohite and remya narayanana, Temperature tunable optical transmission using IR based 1D photonic crystals of VO2 nanostructures, 2020, J. Phys. D: Appl. Phys. 53 245106

2. Dipti umed singh* and Remya Narayanan, Temperature tunable flexible photo absorbers based on near-infrared 1D photonic crystal hybridized W-doped VO_2 nanostructures, 2022, Nanotechnology, 33, 6